NASA Technical Memorandum 110446

Turbulence Modeling Validation, Testing, and Development

J. E. Bardina, P. G. Huang, and T. J. Coakley

April 1997

National Aeronautics and
Space Administration

NASA Technical Memorandum 110446

Turbulence Modeling Validation, Testing, and Development

J. E. Bardina, Caelum Research Corporation, Moffett Field, California
P. G. Huang, University of Kentucky, Lexington, Kentucky
T. J. Coakley, Ames Research Center, Moffett Field, California

April 1997

National Aeronautics and
Space Administration

Ames Research Center
Moffett Field, California 94035-1000

CONTENTS

	Page
General Nomenclature	viii
Summary	1
Introduction	2
Part A. Governing Equations of Motion for a Turbulent Flow	
Section 1. Governing Equations	4
a. Conservation equations	4
b. Turbulent eddy viscosity closure model	4
c. Transformation of transport equations	5
d. Boundary conditions	6
Part B. Turbulence Models	
Section 2. Classification of Turbulence Models	8
Section 3. *k*-ε Two-Equation Model (Launder-Sharma)	9
a. Model classification: 32011	9
b. Summary	9
c. Model equations	9
d. Model constants and parameters	10
e. Boundary conditions	10
f. Numerical implementation	10
Section 4. *k*-ω Two-Equation Model (Wilcox)	12
a. Model classification: 32011	12
b. Summary	12
c. Model equations	12
d. Model constants and parameters	13

e. Boundary conditions 13
f. Numerical implementation 13

Section 5. *SST* Two-Equation Model (Menter) 14
a. Model classification: 32011 14
b. Summary 14
c. Model equations 14
d. Model constants and parameters 15
e. Boundary conditions 16
f. Numerical implementation 16

Section 6. One-Equation Model (Spalart-Allmaras) 17
a. Model classification: 31011 17
b. Summary 17
c. Model equations 17
d. Boundary conditions 19
e. Numerical implementation 19

Part C. Turbulent Free-Shear Flows

Summary 20
Mathematical Formulation 20

Section 7. Mixing Layer 22
a. Introduction 22
b. Experimental data 22
c. Results 23
1) Velocity profiles 23
2) Spreading rate 23
d. Sensitivity analyses 24
1) Freestream turbulence sensitivity study 24
2) Grid resolution sensitivity study 24

3) Initial conditions sensitivity study 25
4) Code sensitivity and Mach number sensitivity study 25

Section 8. Plane Jet 28
a. Introduction 28
b. Experimental data 28
c. Results 28
1) Velocity profiles 29
2) Spreading rate 29
d. Sensitivity analyses 30
1) Freestream turbulence sensitivity study 30
2) Grid sensitivity study 30
3) Initial conditions sensitivity study 30

Section 9. Round Jet 32
a. Introduction 32
b. Experimental data 32
c. Results 32
1) Velocity profiles 33
2) Spreading rate 33
d. Sensitivity analyses 34
1) Freestream turbulence sensitivity study 34
2) Grid sensitivity study 34
3) Initial conditions sensitivity study 34

Section 10. Plane Wake 36
a. Introduction 36
b. Experimental data 36
c. Results 36
1) Velocity profiles 37

2) Spreading rate 37
d. Sensitivity analyses 38
1) Freestream turbulence sensitivity study 38
2) Grid sensitivity study 38
3) Initial conditions sensitivity study 38

Section 11. Compressible Mixing Layer 40
a. Introduction 40
b. Experimental data 40
c. Results 41
1) Velocity profiles 41
2) Spreading rate 42
d. Sensitivity analyses 43
1) Freestream turbulence sensitivity study 43
2) Grid sensitivity study 43
3) Initial conditions sensitivity study 44

Part D. Attached and Separated Turbulent Boundary Layer Flows

Section 12. Incompressible Boundary Layer 48
a. Empirical correlations of data 48
b. Results 49
1) Grid sensitivity study 49
2) Sensitivity to the distance of the first point from the wall, y^+_1 50
3) Freestream sensitivity study 50
4) Effects of inlet conditions and code-independence study 50
5) Mach number effects 50

Section 13. Compressible Flat Plate Flow 56
a. Empirical correlations of data 56

b. Results 57

Section 14. Axisymmetric Boundary Layer with Adverse Pressure Gradient 59

a. Experimental data and description of numerical procedure 59

b. Results 59

Section 15. Transonic Separation Flow over an Axisymmetric “Bump” 67

a. Experimental data 67

b. Results 67

Section 16. Transonic Airfoil: RAE 2822 74

a. Experimental data 74

b. Results 74

Part E. General Conclusions

Section 17. Conclusions and Recommendations 79

Appendix. Self-Similar Equations for Free-Shear Flows 81

a. Compressible boundary layer equations 81

b. Incompressible two-dimensional and axisymmetric equations 82

c. Separation of variables and coordinate transformation 82

d. Self-similar equations 83

e. Boundary conditions 85

References 86

General Nomenclature

The following list shows the nomenclature of the general symbols. Special symbols are not included in this list and are explained in immediate context of the particular models. Few symbols have more than one meaning and they are described in the particular text.

- **General Symbols**

c_d	Drag coefficient
c_f	Skin friction coefficient
c_l	Lift coefficient
c_p	Specific heat at constant pressure
c_v	Specific heat at constant volume
D	Drag force
e	Specific energy, $p/(\gamma - 1) + \rho u_j u_j/2$ for a perfect gas
i	Sub-index; $i = 1,2,3$
j	Sub-index; $j = 1,2,3$
k	Turbulent kinetic energy
l	Turbulent mixing length
L_∞	Characteristic length scale
m	Mass
p	Static pressure
Pr	Prandtl number, $\rho\mu c_p/\kappa$
Pr_t	Turbulent Prandtl number, $\rho\mu_t c_p/\kappa_T$
q_j	Total heat-flux rate in the x_j coordinate direction
q_{lj}	Molecular heat-flux rate in the x_j coordinate direction
q_{tj}	Turbulent heat-flux rate in the x_j coordinate direction
R	Magnitude of mean rotation rate, $(2\Omega_{ij}\Omega_{ij})^{1/2}$
Re	Reynolds number, $\rho UL/\mu$
S	Magnitude of mean strain rate, $(2S_{ij}S_{ij})^{1/2}$
S_{ij}	Mean strain rate tensor, $(\partial u_i/\partial x_j + \partial u_j/\partial x_i)/2$
t	Time
T	Temperature
u_j	Mean flow velocity component in the x_j coordinate direction
U_∞	Characteristic velocity scale
x_j	Space coordinate component; $j = 1,2,3$
y	Space distance to nearest no-slip surface

- **General Greek Symbols**

γ	Ratio of specific heats, c_p/c_v
δ	Boundary layer thickness
δ^*	Displacement thickness
δ_{ij}	Kronecker second-order tensor
ε	Turbulent dissipation rate
ε_{ijl}	Alternating third-order tensor
θ	Momentum thickness
κ	Thermal conductivity
κ_τ	Turbulent eddy thermal conductivity
μ	Molecular viscosity
μ_t	Turbulent eddy viscosity
ν	Kinematic viscosity, m/r
ν_t	Turbulent kinematic eddy viscosity
ρ	Density
τ_{ij}	Total stress tensor
$\tau_{l\,ij}$	Molecular stress tensor
$\tau_{t\,ij}$	Turbulent Reynolds stress tensor
ψ	Stream function
ω	Specific turbulent dissipation rate, turbulent frequency
ω_i	Vorticity vector component, $\varepsilon_{ijl}(\partial\partial u_l/\partial x_j)$
Ω	Magnitude of mean vorticity
Ω_{ij}	Mean rotation tensor, $(\partial\partial u_i/\partial\partial x_j - \partial\partial u_j/\partial\partial x_i)/2$

Turbulence Modeling Validation, Testing, and Development

J. E. Bardina,* P. G. Huang,† and T. J. Coakley

Ames Research Center

Summary

The primary objective of this work is to provide accurate numerical solutions for selected flow fields and to compare and evaluate the performance of selected turbulence models with experimental results. Four popular turbulence models have been tested and validated against experimental data of ten turbulent flows. The models are: 1) the two-equation k-ω model of Wilcox, 2) the two-equation k-ε model of Launder and Sharma, 3) the two-equation k-ω/k-ε *SST* model of Menter, and 4) the one-equation model of Spalart and Allmaras. The flows investigated are five free shear flows consisting of a mixing layer, a round jet, a plane jet, a plane wake, and a compressible mixing layer; and five boundary layer flows consisting of an incompressible flat plate, a Mach 5 adiabatic flat plate, a separated boundary layer, an axisymmetric shock-wave/boundary layer interaction, and an RAE 2822 transonic airfoil. The experimental data for these flows are well established and have been extensively used in model developments. The results are shown in the following four sections: Part A describes the equations of motion and boundary conditions; Part B describes the model equations, constants, parameters, boundary conditions, and numerical implementation; and Parts C and D describe the experimental data and the performance of the models in the free-shear flows and the boundary layer flows, respectively.

*Caelum Research Corporation, Moffett Field, California. Formerly at MCAT Inc., San Jose, California.
†University of Kentucky, Lexington, Kentucky. Formerly at MCAT Inc., San Jose, California.

Introduction

Turbulence is one of the key phenomena in fluid dynamics. A major challenge in aerodynamic designs is the accuracy of turbulence models for simulations of complex turbulent flows. Development of improved turbulence models has increased in the last decade due to technological requirements of present aerodynamic systems and advances in computers and numerical simulation capabilities. The proliferation of models and the lack of information about their performance under different flow conditions create additional uncertainties and risks in the design process. The minimization of these risks can be achieved by defining standard criteria for evaluating turbulence models. Validation and testing of advanced turbulence models are necessary to understand the capabilities and limitations of present turbulence models. A unified and effective evaluation criterion for turbulence models is necessary to accurately predict complex turbulent flows. This process involves the defining and updating of metrics with specific testing and validation procedures. The methodology provides a basis for developing accurate state-of-the-art models and constitutes a framework for NASA, industry, and universities to achieve advances in this important area of engineering development and research (refs. 1–3).

The general objective of this research is to provide NASA and industry with effective turbulence models to be used with the Reynolds-averaged Navier-Stokes equations and implemented in computational fluid dynamics (CFD) codes used to solve aerodynamic flows of interest. The specific aim of this effort is the development of a methodology for the validation and testing of current state-of-the-art turbulence models which can be used and applied to the development and testing of new and advanced models.

The results and discussion presented here serve two purposes—one is to evaluate the performance of turbulence models; the other is to establish standard numerical solutions for the models. The former enables a user to select a “desirable” turbulence model for his application. For example, if one is interested in predicting an impinging jet, one may make selection based on a personal judgement of the model performance in a few relevant benchmark comparisons illustrated in this report, such as free jet or a separating boundary layer. The later enables modelers and users to determine criteria and metrics required to produce code- and grid-independent numerical solutions.

In the present study, four of the currently most popular models were selected in the benchmark comparisons—the two-equation k-ω model of Wilcox (ref. 4), the two-equation k-ε model of Launder and Sharma (refs. 5 and 6), the two-equation k-ω *SST* model of Menter (ref. 7), and the one-equation model of Spalart and Allmaras (refs. 8 and 9). Model developers and users are encouraged to validate results obtained with other models, but it is advised that they follow the guidelines illustrated in each section. It is suggested that the results posted in this report should be repeatable by other computer codes. The establishment of “well-controlled" solutions enables CFD code developers to validate their implementations of the turbulence model in their own application codes. With some careful measures to reduce the possible errors involved, it is expected that the errors be reduced to less than 2% when comparing with the standard solutions provided in this report.

This initial effort addresses ten experimental flows. The flows include free-shear flows, attached and separated boundary layers. The experimental data are well established and has been extensively used in model developments. The basic free-shear flows considered in this validation are a self-similar incompressible mixing layer, round jet, plane jet, plane wake, and compressible mixing layer. The basic boundary layer flows considered in this validation are an incompressible flat plate, a

Mach 5 adiabatic flat plate, a separated boundary layer with adverse pressure gradient, an axisymmetric shock-wave/boundary layer flow, and an RAE 2822 airfoil.

The model validation efforts concentrate on the predictions of the experimental data and the sensitivity to physical and numerical effects. These effects include sensitivity analysis to grid resolution, freestream turbulence, initial conditions, and code selection.

We introduce each test case with a general discussion of the flow and data selected for comparison, which may involve actual measured data sets or may be a well-established experimental correlation. A second section addresses issues regarding sensitivity of the solution to establish standard solutions. These issues involve the assessment of numerical and boundary condition errors and the measures to reduce them. In particular, the "standard" solutions will be reported in this section. In some cases, the computational results are reported in terms of percent errors against experimental correlations. However, this does not indicate that the experimental correlations are the "law of nature" but the purpose is to provide a convenient way to distinguish the model differences. The last section provides particular instructions of the case to establish model solutions that are not only grid independent but also code independent.

The present report is divided in four main sections. Part A describes the governing equations of turbulent flow which in this case are the Reynolds-averaged Navier-Stokes equations. In some test cases, the equations are reduced to the two-dimensional or axisymmetric boundary layer equations, or the self-similar free-shear-layer equations. Part B describes the turbulence models, the model equations, boundary conditions, and numerical treatment. Part C describes the free-shear flows and Part D describes the boundary layer flows. Each flow case describes the experimental data, model predictions, and sensitivity study.

Part A. Governing Equations of Motion for a Turbulent Flow

Section 1. Governing Equations

a. Conservation equations

The governing equations of motion for a continuous viscous fluid are the three-dimensional time-dependent compressible Navier-Stokes equations (ref. 3). These equations represent the flow conservation laws and the fluid property laws. The conservation laws of mass, momentum, and energy and the equation of state for a perfect gas expressed in terms of Reynolds density-averaged variables and compact tensor notation are

- Mass conservation equation:

$$\frac{\partial \rho}{\partial t} + \frac{\partial}{\partial x_j}(\rho u_j) = 0 \tag{1.1}$$

- Momentum conservation equation:

$$\frac{\partial \rho u_i}{\partial t} + \frac{\partial}{\partial x_j}(\rho u_j u_i + p\delta_{ij} - \tau_{ij}) = 0 \tag{1.2}$$

- Energy conservation equation:

$$\frac{\partial e}{\partial t} + \frac{\partial}{\partial x_j}[u_j(e + p) - u_i\tau_{ij} - q_j] = 0 \tag{1.3}$$

- Perfect gas equation of state:

$$p = R\rho T \tag{1.4}$$

Repeated indices in any term denote summation over the spatial index range (j = 1,2,3 for three-dimensional flows and j = 1,2 for two-dimensional flows).

For isothermal flows with incompressible fluids, these equations reduce to the set of mass and momentum equations, and the pressure field is obtained from the mass or continuity equation using the method of artificial compressibility (as in the INS2D code, for example) or other numerical methods.

b. Turbulent eddy viscosity closure model

The closure of these equations requires the definition of the turbulent Reynolds stresses and heat fluxes in terms of known quantities (ref. 4). For eddy viscosity models, the stress tensor is modeled as proportional to the mean strain-rate tensor, and the factor of proportionality is the eddy viscosity which is modeled in terms of additional turbulent scale variables. Two of the more widely used turbulent scales are the turbulent kinetic energy and its rate of energy dissipation.

This report will deal exclusively with isotropic eddy viscosity models. In these models, the total molecular and turbulent stresses and heat fluxes are expressed as functions of the molecular and turbulent viscosities as follows:

- Total molecular and Reynolds stresses:

$$\tau_{ij} = \tau_{l_{ij}} + \tau_{t_{ij}}$$

$$\tau_{l_{ij}} = 2\mu\,(S_{ij} - S_{nn}\delta_{ij}/3)$$

$$\tau_{t_{ij}} = 2\mu_t\,(S_{ij} - S_{nn}\delta_{ij}/3) - 2\rho k\delta_{ij}/3 \tag{1.5}$$

$$\text{where} \qquad S_{ij} = \frac{1}{2}\left(\frac{\partial u_i}{\partial x_j} + \frac{\partial u_j}{\partial x_i}\right)$$

The turbulent stresses are modeled using the Boussinesq approximation in terms of the eddy viscosity, μ_t, in analogy with Stoke's law for the molecular stresses.

- Heat-flux rates:

$$q_j = q_{l_j} + q_{t_j} = -(\kappa + \kappa_t)\frac{\partial T}{\partial x_j} \tag{1.6}$$

The turbulent heat-transfer rates are modeled following Fourier's law for laminar flow in terms of the eddy thermal conductivity, κ_t.

In most application CFD codes, the equations are written in nondimensional form, and the shear stresses and heat-flux rates are expressed in terms of Reynolds and Prandtl numbers. The shear-stress and heat-flux equations 1.5 and 1.6 may be written in terms of general nondimensional variables as follows:

- Total stresses:

$$\tau_{ij} = 2\,(\,(\mu + \mu_t)/Re_\infty)\,(S_{ij} - S_{nn}\delta_{ij}/3) - 2\rho k\delta_{ij}/3 \tag{1.7}$$

- Heat-flux rates:

$$q_j = -\left(\frac{\gamma}{\gamma - 1}\right)\frac{1}{Re_\infty}\left(\frac{\mu}{Pr} + \frac{\mu_t}{Pr_t}\right)\frac{\partial T}{\partial x_j} \tag{1.8}$$

with all variables representing nondimensional quantities, and reference variables denoted as L_∞, ρ_∞, and p_∞ (or u_∞) which are usually defined based on inlet or freestream conditions.

The closure using a turbulent eddy viscosity model defines μ_t in terms of known mean quantities and additional turbulent-scale quantities with their respective transport equations, such as turbulent kinetic energy and its rate of dissipation. In sections 3–6 of Part B, four eddy viscosity models are described in detail, including a one-equation and three two-equation turbulence models.

c. Transformation of transport equations

The governing equations of motion are applied to different flows. The complexity of the flow geometry varies from simple to very complex. The equations of motion are frequently transformed and simplified to represent these problems more efficiently. For example, the equations are often transformed into generalized curvilinear coordinates or unstructured systems to simulate complex geometries. The equations may be simplified to represent axisymmetric or two-dimensional flows,

and may be simplified further to represent boundary layers. The equations may be transformed into self-similar coordinates and variables to represent equilibrium boundary and free-shear layers.

The free-shear layers tested in this report have been solved using the Navier-Stokes equations and similarity equations. In particular, the similarity equations to represent the free-shear layers are given in the appendix of this report. These equations are reported for the purpose of indicating the precise assumptions and approximations used in the formulations.

d. Boundary conditions

The particular boundary conditions imposed on the flow variables are flow dependent, and they will be described in Parts C and D. In general, most boundary conditions are Dirichlet or von Neumann conditions. Dirichlet conditions with specific function values are typically specified at inflow boundaries, while von Neumann conditions with specified zero gradients are typically specified at symmetry boundaries. No slip (mixed) conditions are specified at wall boundaries. Normally, outflow conditions are extrapolated.

Part B. Turbulence models

The following sections give a general classification of turbulence models as a framework of reference and a detailed description of each one of the four turbulence eddy viscosity models validated in this study.

Section 2.	Classification of Turbulence Models
Section 3.	k-ε Two-Equation Model (Launder-Sharma)
Section 4.	k-ω Two-Equation Model (Wilcox)
Section 5.	*SST* Two-Equation Model (Menter)
Section 6.	One-Equation Model (Spalart-Allmaras)

Section 2. Classification of Turbulence Models

The general classification of the turbulence models using one-point closure is shown below as a framework of reference for the turbulence models and is defined as follows:

- **Major classification** determines the modeling of the turbulent stresses:

  1) Reynolds stress model

  2) Algebraic stress model

  3) Eddy viscosity model

- **Subclassification 1** determines the number of partial-differential model equations required to define the turbulent scales.

- **Subclassification 2** determines the number of ordinary-differential or other non-partial-differential model equations required to define the turbulent scales.

- **Subclassification 3** determines the general type of fluid of the model:

  1) Incompressible/compressible fluid model

  2) Compressible fluid model

  3) Incompressible fluid model

- **Subclassification 4** determines the treatment of the near wall-boundary flow:

  1) Integration to the wall

  2) Wall function

  3) Algebraic with matching point

  4) Switch to one-equation near the wall

- **Other models** that may not be easily classifiable in the preceding format should be clearly described by the developer and so noted.

For example, the standard two-equation k-ε and k-ω turbulence models are classified as eddy viscosity models, with two partial-differential equations for incompressible and compressible fluids, and integration capability to the wall, i.e., 32011. (The number 32011 denotes that the major classification is 3, the subclassification 1 is 2, the subclassification 2 is 0, the subclassification 3 is 1, and the subclassification 4 is 1.) The one-equation Spalart-Allmaras model is classified as an eddy viscosity model, with one partial-differential equation for incompressible and compressible fluids, and integration capability to the wall, i.e., 31011.

Section 3. *k*-ε Two-Equation Model (Launder-Sharma)

a. Model classification: 32011

Two-equation eddy viscosity model for incompressible/compressible turbulent flows with integration to the wall.

b. Summary

The *k*-ε model (refs. 4–6) is the most widely known and extensively used two-equation eddy viscosity model. Different versions of this model are found in the literature. The main references on this model are described by Jones and Launder (ref. 5) and Launder and Sharma (ref. 6). The formulation used here is the one of Launder and Sharma. This model is sometimes referred in this report as the standard *k*-ε model. Other formulations of the *k*-ε model are reported in the literature or are commercially available, and should be included in future work (refs. 4 and 10).

The *k*-ε model was originally developed to improve the mixing-length model and to avoid the algebraic prescription of the turbulent length scale in complex flows. Transport equations are solved for two scalar properties of turbulence. The *k*-equation is a model of the transport equation for the turbulent kinetic energy, and the ε-equation is a model for the dissipation rate of turbulent kinetic energy.

This model has given reasonably good results for free-shear-layer flows with relatively small pressure gradients. For wall bounded flows, the model gives good agreement with experimental results for zero and small mean pressure gradients, but is less accurate for large adverse pressure gradients (ref. 4). The predictions of the model are insensitive to freestream values of the turbulence. The model requires explicit wall-damping functions and the use of fine grid spacing near solid walls.

c. Model equations

The Reynolds stresses are modeled in terms of the eddy viscosity as follows:

$$\tau_{t_{ij}} = 2\mu_t (S_{ij} - S_{nn}\delta_{ij}/3) - 2\rho k \delta_{ij}/3 \tag{3.1}$$

where μ_t is the eddy viscosity, S_{ij} is the mean-velocity strain-rate tensor, ρ is the fluid density, *k* is the turbulent kinetic energy, and δ_{ij} is the Kronecker delta.

The eddy viscosity is defined as a function of the turbulent kinetic energy, *k*, and the turbulent dissipation rate, ε, as

$$\mu_t = c_\mu f_\mu \rho k^2/\varepsilon \tag{3.2}$$

The eddy viscosity is scaled with the fluid density, ρ, the turbulent velocity scale, $k^{1/2}$, and the length-scale, $k^{3/2}/\varepsilon$, based on local dimensional analysis. The model coefficient, c_μ, is determined by equilibrium analysis at high Reynolds numbers, and the damping function, f_μ, is modeled in terms of a turbulence Reynolds number, $Re_t = \rho k^2/\varepsilon\mu$.

The turbulence transport equations for the *k*-ε Launder-Sharma model are defined below.

- Turbulence energy transport equation:

$$\frac{\partial \rho k}{\partial t} + \frac{\partial}{\partial x_j}\left(\rho u_j \frac{\partial k}{\partial x_j} - \left(\mu + \frac{\mu_\tau}{\sigma_k}\right)\frac{\partial k}{\partial x_j}\right) = \tau_{tij} S_{ij} - \rho\varepsilon + \phi_k \tag{3.3}$$

- Energy dissipation transport equation:

$$\frac{\partial \rho \varepsilon}{\partial t} + \frac{\partial}{\partial x_j}\left(\rho u_j \varepsilon - \left(\mu + \frac{\mu_\tau}{\sigma_\varepsilon} \right) \frac{\partial \varepsilon}{\partial x_j} \right) = c_{\varepsilon 1} \frac{\varepsilon}{k} \tau_{t_{ij}} S_{ij} - c_{\varepsilon 2} f_2 \rho \frac{\varepsilon^2}{k} + \phi_\varepsilon \tag{3.4}$$

where the right-hand-side terms represent production, dissipation, and wall terms, respectively.

d. Model constants and parameters

The model constants are defined below as

$$\begin{aligned} c_\mu &= 0.09 \qquad c_{\varepsilon 1} = 1.45 \qquad c_{\varepsilon 2} = 1.92 \\ \sigma_k &= 1.0 \qquad \sigma_\varepsilon = 1.3 \qquad Pr_t = 0.9 \end{aligned} \tag{3.5}$$

The near wall damping functions are

$$\begin{aligned} f_\mu &= \exp\left(-3.4 / (1 + 0.02 Re_t)^2 \right) \\ f_2 &= 1 - 0.3 \exp\left(-Re_t^2 \right) \end{aligned} \quad \text{and} \quad Re_t = \frac{\rho k^2}{\mu \varepsilon} \tag{3.6}$$

and the explicit wall terms are

$$\phi_k = 2\mu \left(\frac{\partial \sqrt{k}}{\partial y} \right)^2 \quad \text{and} \quad \phi_\varepsilon = 2\mu \frac{\mu_t}{\rho} \left(\frac{\partial^2 u_s}{\partial y^2} \right)^2 \tag{3.7}$$

where u_s is the flow velocity parallel to the wall.

e. Boundary conditions

Boundary conditions at no-slip surfaces with integration to the wall are given by the following simpler relationships:

$$k = 0 \quad \text{and} \quad \varepsilon = 0 \tag{3.8}$$

when the above wall terms are included (see eq. 3.7) and the effective dissipation rate is expressed as $\varepsilon - \phi_k/\rho$. Zero-gradient conditions are applied at symmetry boundaries, and additional boundary conditions are discussed further for each flow case.

f. Numerical implementation

The turbulence transport equations are similar to the transport equations of the mean flow. The recommended numerical treatment of each term of the turbulence transport equations is the numerical treatment used in this work for the mean flow equations of each particular numerical code. Although not including any specific reference, these statements reflect the general treatment used in different numerical methods and codes developed and applied at NASA Ames Research Center.

Second-order numerical differences are recommended and used for the convective and diffusive terms of the flow and turbulence model equations. For the convective terms using Navier-Stokes solvers, second-order upwind flux-difference splitting methods with flux-limiters have been used and are recommended, although in some cases first-order methods have been used successfully with the turbulence equations. Implicit second-order central-difference methods for the diffusion terms of the

momentum, energy, and turbulence model equations have been used and are recommended. These methods provide efficient numerical procedures and good agreement with theory and experiment.

The numerical treatment of source terms of the turbulence model equations is of major importance for the stability of this scheme. It is recommended to treat implicitly all negative (destruction) terms and explicitly all positive (production) right-hand-side terms. This procedure leads to an increase in the diagonal dominance of the implicit portion of the scheme and thereby enhances its stability. The following representation of the approximate linearization for the source terms of the turbulent kinetic energy equation is indicative of the method employed here.

$$[P_k - D_k]_{n+1} \approx [P_k - D_k]_n - \left[\frac{D_k}{k}\right]_n (k_{n+1} - k_n) \tag{3.9}$$

where P_k and D_k represent the sum of the positive and negative source terms, respectively, and the subscript n and n+1 represent the current and the next time steps, respectively. See reference 32 for additional details in the procedure.

Section 4. k-ω Two-Equation Model (Wilcox)

a. Model classification: 32011

Two-equation eddy viscosity model for incompressible/compressible turbulent flows with integration to the wall.

b. Summary

The k-ω model (refs. 4 and 11) is a well known and widely tested two-equation eddy viscosity model. The main reference to this model is given by Wilcox (ref. 4), and his formulation is used here. This model is referred to here as the standard k-ω model. The roots of this model can be traced to Kolmogorov, Prandtl, Saffman, and Wilcox in collaboration with other scientists.

This model was originated at about the same time and was developed in parallel with the k-ε model as an alternative to define the eddy viscosity function. Convective transport equations are solved for the turbulent kinetic energy and its specific dissipation rate, k and ω, respectively.

The k-ω model of Wilcox has proven to be superior in numerical stability to the k-ε model primarily in the viscous sublayer near the wall. This model does not require explicit wall-damping functions as do the k-ε and other two-equation models due to the large values of ω in the wall region. The numerical wall boundary conditions require the specification of the distance from the wall to the first point off the wall. In the logarithmic region, the model gives good agreement with experimental results for mild adverse pressure gradient flows.

In free-shear layer and adverse-pressure-gradient boundary layer flows, the results of the k-ω model are sensitive to small freestream values of ω (refs. 11 and 12). In complex Navier-Stokes computations it is difficult to exercise enough control over the local freestream turbulence to avoid small freestream ω and ambiguities in the predicted results.

c. Model equations

The Reynolds stresses are modeled in terms of the eddy viscosity as follows:

$$\tau_{t_{ij}} = 2\mu_t (S_{ij} - S_{nn}\delta_{ij}/3) - 2\rho k \delta_{ij}/3 \tag{4.1}$$

The eddy viscosity is defined as a function of the turbulent kinetic energy, k, and the specific rate of dissipation, ω, as follows:

$$\mu_t = \rho k/\omega \tag{4.2}$$

The two transport model equations for the k and ω scalar turbulence scales are defined below.

$$\frac{\partial \rho k}{\partial t} + \frac{\partial}{\partial x_j}\left(\rho u_j k - (\mu + \sigma^* \mu_t)\frac{\partial k}{\partial x_j}\right) = \tau_{t_{ij}} S_{ij} - \beta^* \rho \omega k \tag{4.3}$$

$$\frac{\partial \rho \omega}{\partial t} + \frac{\partial}{\partial x_j}\left(\rho u_j \omega - (\mu + \sigma \mu_t)\frac{\partial \omega}{\partial x_j}\right) = \alpha \frac{\omega}{k} \tau_{t_{ij}} S_{ij} - \beta \rho \omega^2 \tag{4.4}$$

d. Model constants and parameters

Following Wilcox (ref. 4), the model constants are defined as

$$\alpha = \frac{5}{9} \qquad \beta = \frac{3}{40} \qquad \beta^* = \frac{9}{100}$$
$$\sigma = 0.5 \qquad \sigma^* = 0.5 \qquad Pr_t = 0.9 \tag{4.5}$$

e. Boundary conditions

The choice of freestream values recommended for boundary layer flows (ref. 3) are

$$\omega_\infty > \lambda \frac{U_\infty}{L} \qquad \mu_{t\infty} < 10^{-2}\mu_{tmax} \qquad k_\infty = \frac{\mu_{t\infty}}{\rho_\infty}\omega_\infty \tag{4.6}$$

where L is the approximate length of the computational domain and U_∞ is the characteristic velocity. The factor of proportionality $\lambda = 10$ has been recommended (ref. 3).

Free-shear layers are more sensitive to small freestream values of ω_∞ and larger values of ω are needed in the freestream. Following a similar analysis to the one referenced above, and based on the analysis of self-similarity, a value of λ may be determined. This analysis is not included here; however, it shows a value of at least $\lambda = 40$ for mixing layers, increasing up to $\lambda = 80$ for round jets.

Boundary conditions at no-slip surfaces are given by the following relationships:

$$k = 0 \qquad \text{and} \qquad \omega = 10\frac{6\mu}{\beta\rho\,(y_1)^2} \tag{4.7}$$

where y_1 is the distance of the first point away from the wall and $y_1^+ < 1$.

Zero-gradient conditions are applied at symmetry boundaries, and additional boundary conditions are discussed further for each flow case.

f. Numerical implementation

The numerical implementation of the k-ω model equations is similar to that described on pages 10 and 11 for two-equation models. The implicit treatment of the source terms shows one difference—a factor of 2 is introduced in the implicit treatment of the dissipation term $\beta\rho\omega^2$ of the ω-equation due to the proportionality of this term to ω^2.

Section 5. *SST* Two-Equation Model (Menter)

a. Model classification: 32011

Two-equation eddy viscosity model for incompressible/compressible turbulent flows with integration to the wall. Following Menter, this model is expressed in terms of a k-ω model formulation.

b. Summary

The k-ω *SST* shear-stress-transport model (refs. 7 and 12–14) combines several desirable elements of existing two-equation models. The two major features of this model are a zonal weighting of model coefficients and a limitation on the growth of the eddy viscosity in rapidly strained flows. The zonal modeling uses Wilcox's k-ω model near solid walls and the standard k-ε model (in a k-ω formulation) near boundary layer edges and in free-shear layers. This switching is achieved with a blending function of the model coefficients. The shear stress transport modeling also modifies the eddy viscosity by forcing the turbulent shear stress to be bounded by a constant times the turbulent kinetic energy inside boundary layers (a realizability constraint). This modification improves the prediction of flows with strong adverse pressure gradients and separation.

In order to blend the k-ω and the k-ε model, the latter is transformed into a k-ω formulation. The differences between this formulation and the original k-ω model are that an additional cross-diffusion term appears in the ω-equation and that the modeling constants are different. The original k-ω model is then multiplied by a function F_1 and the transformed k-ε model by a function $(1 - F_1)$ and the corresponding equations of each model are added together. The function F_1 is designed to be a value of one in the near wall region (activating the original model) and zero far from the wall. The blending takes place in the wake region of the boundary layer.

The *SST* model also modifies the turbulent eddy viscosity function to improve the prediction of separated flows. Two-equation models generally underpredict the retardation and separation of the boundary layer due to adverse pressure gradients. This is a serious deficiency, leading to an underestimation of the effects of viscous-inviscid interaction which generally results in too optimistic performance estimates for aerodynamic bodies. The reason for this deficiency is that two-equation models do not account for the important effects of transport of the turbulent stresses. The Johnson-King model (ref. 15) has demonstrated that significantly improved results can be obtained with algebraic models by modeling the transport of the shear stress as being proportional to that of the turbulent kinetic energy. A similar effect is achieved in the present model by a modification in the formulation of the eddy viscosity using a blending function F_2 in boundary layer flows.

c. Model equations

The eddy viscosity is defined as the following function of the turbulent kinetic energy, k, and specific dissipation rate or turbulent frequency, ω:

$$\mu_t = \frac{\rho k / \omega}{max\,[1; \Omega F_2 / (a_1 \omega)]} \qquad a_1 = 0.31 \tag{5.1}$$

In turbulent boundary layers, the maximum value of the eddy viscosity is limited by forcing the turbulent shear stress to be bounded by the turbulent kinetic energy times a_1. This effect is achieved with an auxiliary function F_2 and the absolute value of the vorticity, Ω. The auxiliary function, F_2, is defined as a function of wall distance y as

$$F_2 = \tanh\left\{\left(max\left[2\frac{\sqrt{k}}{0.09\omega y};\frac{500\mu}{\rho y^2\omega}\right]\right)^2\right\} \tag{5.2}$$

The two transport equations of the model are defined below with a blending function F_1 for the model coefficients of the original ω and ε model equations. The transport equation for the turbulent kinetic energy is

$$\frac{\partial\rho k}{\partial t} + \frac{\partial}{\partial x_j}\left(\rho u_j k - (\mu + \sigma_k\mu_t)\frac{\partial k}{\partial x_j}\right) = \tau_{t_{ij}}S_{ij} - \beta^*\rho\omega k \tag{5.3}$$

and the transport equation for the specific dissipation of turbulence is

$$\frac{\partial\rho\omega}{\partial t} + \frac{\partial}{\partial x_j}\left(\rho u_j\omega - (\mu + \sigma_\omega\mu_t)\frac{\partial\omega}{\partial x_j}\right) = P_\omega - \beta\rho\omega^2 + 2(1 - F_1)\frac{\rho\sigma_{\omega 2}}{\omega}\frac{\partial k}{\partial x_j}\frac{\partial\omega}{\partial x_j} \tag{5.4}$$

where the last term of equation 5.4 represents the cross-diffusion term that appears in the transformed ω-equation from the original ε-equation. The production term of ω is sometimes approximated as proportional to the absolute value of vorticity (ref. 14):

$$P_\omega \equiv 2\gamma\rho\,(S_{ij} - \omega S_{nn}\delta_{ij}/3)\,S_{ij} \approx \gamma\rho\Omega^2 \tag{5.5}$$

d. Model constants and parameters

The function F_1 is designed to blend the model coefficients of the original *k*-ω model in boundary layer zones with the transformed *k*-ε model in free-shear layer and freestream zones. This function takes the value of one on no-slip surfaces and near one over a large portion of the boundary layer, and goes to zero at the boundary layer edge. This auxiliary blending function, F_1, is defined as

$$F_1 = \tanh\left\{\left(min\left[max\left[\frac{\sqrt{k}}{0.09\omega y};\frac{500\mu}{\rho y^2\omega}\right];\frac{4\rho\sigma_{\omega 2}k}{CD_{k\omega}y^2}\right]\right)^4\right\}$$
$$\text{where} \qquad CD_{k\omega} = max\left[\frac{2\rho\sigma_{\omega 2}}{\omega}\frac{\partial k}{\partial x_j}\frac{\partial\omega}{\partial x_j};10^{-20}\right] \tag{5.6}$$

where $CD_{k\omega}$ stands for cross-diffusion in the *k*-ω model.

The constants of the *SST* model are

$$a_1 = 0.31 \qquad \beta^* = 0.09 \qquad \kappa = 0.41 \tag{5.7}$$

The model coefficients β, γ, σ_k, and σ_ω denoted with the symbol ϕ are defined by blending the coefficients of the original *k*-ω model, denoted as ϕ_1, with those of the transformed *k*-ε model, denoted as ϕ_2.

$$\phi = F_1\phi_1 + (1 - F_1)\phi_2 \qquad \text{where} \qquad \phi = \{\sigma_k, \sigma_\omega, \beta, \gamma\} \tag{5.8}$$

with the coefficients of the original models defined as

- Inner model coefficients:

$$\sigma_{k1} = 0.85 \qquad \sigma_{\omega 1} = 0.5 \qquad \beta_1 = 0.075$$
$$\gamma_1 = \beta_1 / \beta^* - \sigma_{\omega 1}\kappa^2 / \sqrt{\beta^*} = 0.553 \tag{5.9}$$

- Outer model coefficients:

$$\sigma_{k2} = 1.0 \qquad \sigma_{\omega 2} = 0.856 \qquad \beta_2 = 0.0828$$
$$\gamma_2 = \beta_2 / \beta^* - \sigma_{\omega 2}\kappa^2 / \sqrt{\beta^*} = 0.440 \tag{5.10}$$

e. Boundary conditions

The boundary conditions of the *k*-ω *SST* model equations are the same as those described in section 4 for the *k*-ω model.

f. Numerical implementation

The numerical implementation of the *SST* model equations is similar to the one described on pages 10 and 11 for two-equation models. The implicit treatment of the source terms of the ω equation includes a factor of 2 for the dissipation term $\beta\rho\omega^2$ due to the proportionality of this term to ω^2.

The production term of ω written as a function of the absolute vorticity (see eq. 5.5) together with a limiter on the production of turbulent kinetic energy, P_k, have been found to be beneficial numerically in some cases (ref. 14). This procedure can help to prevent the unrealistic buildup of eddy viscosity in the stagnation region of airfoils and can help to suppress numerical oscillations near turbulent and nonturbulent interfaces. These effects have also been observed with other two-equation models. The limiter recommended on the production of turbulent kinetic energy bounds the production of turbulent kinetic energy to a value not larger than 20 times the dissipation of turbulent kinetic energy.

Section 6. One-Equation Model (Spalart-Allmaras)

a. Model classification: 31011

One-equation eddy viscosity model for incompressible/compressible turbulent flows with integration to the wall.

b. Summary

The Spalart-Allmaras model (refs. 4, 8, and 9) is a relatively recent eddy viscosity model based on a transport equation for the turbulent viscosity. This model was inspired from an earlier model developed by Baldwin and Barth (ref. 16). Its formulation and coefficients were defined using dimensional analysis, Galilean invariance, and selected empirical results. The empirical results used in its development were two-dimensional (2-D) mixing layers, wakes, and flat-plate boundary layer flows.

The aim of this model is to improve the predictions obtained with algebraic mixing-length models to develop a local model for complex flows, and to provide a simpler alternative to two-equation turbulence models.

The model uses distance to the nearest wall in its formulation, and provides smooth laminar-turbulent transition capabilities, provided that the location of the start of transition is given. It does not require as fine a grid resolution in wall-bounded flows as two-equation turbulence models, and it shows good convergence in simpler flows.

The model does not give good predictions in jet flows, but gives reasonably good predictions of 2-D mixing layers, wake flows, and flat-plate boundary layers and shows improvements in the prediction of flows with adverse pressure gradients compared with the k-ε and k-ω models, although not as much as the *SST* model.

c. Model equations

The eddy viscosity function is defined in terms of an eddy viscosity variable, $\tilde{\nu}$, and a wall function, f_{v1}, as follows:

$$\nu_t = \tilde{\nu} f_{v1} \tag{6.1}$$

In zones far from wall boundaries, the function f_{v1} is equal to one and $\nu_t = \tilde{\nu}$.

The convective transport equation of the eddy viscosity is modeled as

$$\frac{\partial \rho \tilde{\nu}}{\partial t} + \frac{\partial}{\partial x_j}\left(\rho \tilde{\nu} u_j\right) = c_{b1}\,(1 - f_{t2})\,\rho \tilde{S} \tilde{\nu} + \frac{1}{\sigma}\left[\frac{\partial}{\partial x_j}\left(\rho\,(\nu + \tilde{\nu})\,\frac{\partial \tilde{\nu}}{\partial x_j}\right) + c_{b2}\rho \frac{\partial \tilde{\nu}}{\partial x_j}\frac{\partial \tilde{\nu}}{\partial x_j}\right] \tag{6.2}$$

$$-\left[c_{w1} f_w - \frac{c_{b1}}{\kappa^2} f_{t2}\right]\rho\left[\frac{\tilde{\nu}}{d}\right]^2 + f_{t1}\rho \Delta U^2 \tag{6.3}$$

where the right-hand-side terms represent turbulence eddy viscosity production, conservative diffusion, nonconservative diffusion, near-wall turbulence destruction, transition damping of production, and transition source of turbulence. The subscript b stands for “basic,” w stands for “wall,” v stands for “viscous,” and t stands for “trip” (start of transition).

The model constants and auxiliary functions are defined in terms of the basic model for free-shear flows, the wall model for boundary layers, the viscous model for integration to the wall, and the transition model for laminar-turbulent transition.

The basic model constants for free-shear flows to control the production and diffusion of turbulent eddy viscosity are

$$c_{b1} = 0.1355 \qquad c_{b2} = 0.622 \qquad \sigma = 2/3 \tag{6.4}$$

The additional model constants and auxiliary functions for the destruction of turbulent eddy viscosity in the boundary layer zone are

$$\begin{aligned} c_{w1} &= c_{b1}/\kappa^2 + (1 + c_{b2})/\sigma \qquad r \equiv \frac{\tilde{\nu}}{\tilde{S}\kappa^2 d^2} \\ c_{w2} &= 0.3 \qquad g = r + c_{w2}\left(r^6 - r\right) \\ c_{w3} &= 2 \qquad f_w = g\left(\frac{1 + c_{w3}^6}{g^6 + c_{w3}^6}\right)^{1/6} \end{aligned} \tag{6.5}$$

These auxiliary functions allow the model to predict the log layer, although the particular budget of the Reynolds shear stress is not in quantitative agreement with experimental data.

Modeling functions and constants for the near wall flow regions are given by

$$\begin{aligned} \tilde{S} &\equiv S + \frac{\tilde{\nu}}{(\kappa d)^2} f_{v2} \qquad S = \sqrt{2S_{ij}S_{ij}} \qquad \chi \equiv \frac{\tilde{\nu}}{\nu} \\ f_{v1} &= \frac{\chi^3}{\chi^3 + c_{v1}^3} \qquad f_{v2} = 1 - \frac{\chi}{1 + \chi f_{v1}} \qquad c_{v1} = 7.1 \end{aligned} \tag{6.6}$$

The auxiliary functions and model constants to control the laminar region of the shear layers and transition to turbulence are defined with a source term controlled with the function f_{t1} and a reduction of production controlled with the function f_{t2}.

$$\begin{aligned} f_{t1} &= c_{t1} g_t \cdot exp\left(-c_{t2}\frac{\omega_t^2}{\Delta U^2}\left[d^2 + (g_t d_t)^2\right]\right) \\ f_{t2} &= c_{t3} \cdot exp\left(-c_{t4}\chi^2\right) \\ g_t &= min\left[0.1, \Delta U/(\omega_t \Delta x_t)\right] \\ c_{t1} &= 1 \qquad c_{t2} = 2 \qquad c_{t3} = 1.2 \qquad c_{t4} = 0.5 \end{aligned} \tag{6.7}$$

where ω_t is the vorticity at the boundary layer trip point, ΔU is the norm of the difference between the velocity at the field point and the velocity at the trip point, Δx_t is the grid spacing along the wall at the trip, and d is the distance from the wall.

d. Boundary conditions

The ideal value of the freestream eddy viscosity variable is zero. Some solvers have trouble with zero freestream values, and values smaller than $\nu/2$ have been recommended. Small freestream values are recommended for free-shear flows; otherwise, the solutions show freestream dependence in velocity profiles and spreading rates. At wall boundaries the eddy viscosity is zero.

e. Numerical implementation

The numerical implementation of the Spalart-Allmaras model equations that we used here is similar to the one described on pages 10 and 11 for two-equation models.

Part C. Turbulent Free-Shear Flows

Summary

Turbulent free-shear flows are defined as turbulent flows not interacting with solid boundaries. These flows provide a good balance for testing the predictive capability of models on diffusion effects and calibration of model coefficients. Five turbulent free-shear flows are included in this study, and the results of each flow are shown in the following sections:

Section 7.	Mixing Layer
Section 8.	Plane Jet
Section 9.	Round Jet
Section 10.	Plane Wake
Section 11.	Compressible Mixing Layer

Four turbulence eddy viscosity models are validated for the prediction of these turbulent free-shear flows. The four models included in the present study are the two-equation k-ω model of Wilcox (ref. 4), the two-equation k-ε model of Launder and Sharma (refs. 5 and 6), the two-equation k-ω *SST* model of Menter (ref. 7), and the one-equation model of Spalart and Allmaras (*S-A*) (refs. 8 and 9). These models and their equations are described in Part B of this report.

The validation of each model is mainly based on the ability of the models to predict the mean velocity profile and spreading rate of each one of these fully developed free-shear flows. Differences observed in the predictions of these flows may be explained in part because some of the model constants have been defined or selected during the model development based on one of these flows.

Sensitivity analyses of the validation results to freestream turbulence, grid resolution, and initial profiles are included in each section. In general, the results showed great sensitivity to grid resolution with all the turbulence models, and to freestream turbulence with some of the models. In particular, the k-ω model showed large sensitivity to low freestream ω values, and the k-ε model showed no sensitivity to low freestream ε values. The predictions of the shapes of nondimensional mean velocity profiles and their spreading rates were insensitive to different initial profiles in each flow beyond the initial development zone. The sensitivity of the results to numerical codes and freestream Mach numbers used with compressible codes is also shown in section 7 for the incompressible mixing layer. These results showed good consistency from flow to flow.

Mathematical Formulation

The governing equations are the Navier-Stokes equations at high Reynolds numbers and are described in Part A of this report. For self-similar free-shear flows, these equations can be reduced to a simpler form through similarity transformations and the boundary layer approximation. The appendix gives the self-similar free-shear flow equations and boundary conditions expressed in terms of similarity coordinates. These equations were used to obtain most of the free-shear flow results shown here. The agreement between Navier-Stokes and self-similar predictions is given in section 7 for the incompressible mixing layer.

The boundary conditions imposed on the equations of motion are defined by the respective states of the freestreams, and reflection conditions in symmetry planes of plane jets and axes of symmetry in round jets. Integral constraints based on the conservation of total momentum and the displacement thickness of the layer were used for the jet and wake calculations, as described in reference 4.

For the self-similar equations, the equations were solved in delta form using an implicit relaxation procedure until the residuals of the dependent variables converged to zero within computer machine accuracy. The numerical method used to solve these equations was an implicit upwind algorithm for the convective terms, second-order-implicit central differences for the diffusion terms, and implicit treatment of the destruction source terms of the turbulence model equations. This method is described further in the appendix. The solutions of these equations showed fast rate of convergence. Very small and large values of freestream variables required upper and lower limiters in the eddy viscosity during the transient relaxation time to achieve fast convergence.

No significant differences were observed between results obtained with self-similar and Navier-Stokes simulations with similar corresponding boundary conditions. However, different freestream conditions are normally used with different methods. For example, self-similar calculations are usually done with fixed boundary conditions. Navier-Stokes simulations with the one-equation model of Spalart and Allmaras are also normally done with fixed freestream states. On the other hand, Navier-Stokes simulations with two-equation turbulence models normally produce a decay of freestream turbulence, and this decay is inversely proportional to the freestream speed. This difference is not an issue in models whose results are insensitive to freestream turbulence; for example, the k-ε and the k-ω *SST* models. However, the results of mean velocity profiles obtained with the k-ω model are very sensitive to low values of freestream ω, and ω decays rapidly in streams at rest. Thus under these conditions the k-ω model can give different results for low freestream values of ω using the self-similar equations and the Navier-Stokes equations. The results obtained with the Spalart-Allmaras model are not sensitive to freestream turbulence, except for very large values of freestream eddy viscosity, which may become an issue in complex flows.

Section 7. Mixing Layer

a. Introduction

Turbulent mixing layers are of considerable interest in engineering design and represent a class of flows encountered in many aerodynamic applications (refs. 1–4 and 17). Mixing layer flows are defined as the region between two parallel streams moving at different speeds. The self-preserving properties of fully developed free-shear flows have been extensively used to validate model coefficients in almost all well-known turbulence models (ref. 4). Single phase, incompressible, fully developed turbulent mixing layer flows are considered fundamental flows in turbulence modeling.

At high Reynolds numbers and far downstream of transition and initial effects, the mixing layer develops an asymptotic equilibrium state. The analysis of the experimental data in the 1980–81 AFOSR-HTTM-Stanford Conference on Complex Turbulent Flows (ref. 17) reported a spreading rate of 0.115 for a fully developed mixing layer between stagnant and moving streams. The mean velocity profile and its spreading rate are considered the most significant parameters in this flow.

b. Experimental data

Model validation requires a carefully selected set of experimental data, along with the proper mathematical and numerical formulation of the governing equations of motion. Experimental data reveal that even simple measurements have varied between different experiments in the initial zone of development of the mixing layer. This zone is sensitive to initial conditions of flow structures of the layer, boundary conditions imposed by the flow geometry, and Reynolds number effects. After the mixing layer is fully developed, the available experimental data show a unique self-similar mean-velocity profile with an asymptotic spreading rate value (refs. 17 and 18).

In the present study, the predictions are compared against the experimental data of Liepmann and Laufer (ref. 19) where one freestream is at rest and the other freestream is moving at speed U_1. The experimental data are defined as $\eta = y/x + 0.007$ and U/U_1, where the data arrays are

$$
\begin{aligned}
y/x = [&-0.180, -0.176, -0.160, -0.150, -0.147, -0.145, -0.135, -0.132, -0.129, -0.126, -0.120,\\
&-0.116, -0.115, -0.113, -0.113, -0.106, -0.102, -0.100, -0.097, -0.095, -0.092, -0.089,\\
&-0.084, -0.081, -0.080, -0.077, -0.077, -0.069, -0.065, -0.065, -0.063, -0.062, -0.053,\\
&-0.050, -0.048, -0.044, -0.040, -0.036, -0.034, -0.033, -0.028, -0.026, -0.021, -0.019,\\
&-0.017, -0.016, -0.010, -0.009, -0.005, -0.004, -0.002, 0.008, 0.011, 0.011, 0.015,\\
&0.021, 0.025, 0.027, 0.030, 0.033, 0.039, 0.042, 0.044, 0.045, 0.046, 0.054,\\
&0.057, 0.058, 0.062, 0.062, 0.069, 0.074, 0.078, 0.079, 0.081, 0.083, 0.090,\\
&0.094, 0.094, 0.096, 0.098, 0.106, 0.110, 0.113, 0.115, 0.118, 0.121, 0.126]
\end{aligned}
$$

$$
\begin{aligned}
U/U_1 = [&0.015, 0.050, 0.055, 0.040, 0.040, 0.075, 0.055, 0.050, 0.075, 0.045, 0.060,\\
&0.060, 0.065, 0.055, 0.100, 0.075, 0.085, 0.088, 0.090, 0.125, 0.107, 0.105,\\
&0.114, 0.170, 0.145, 0.145, 0.137, 0.177, 0.195, 0.255, 0.220, 0.210, 0.245,\\
&0.300, 0.285, 0.295, 0.310, 0.335, 0.380, 0.350, 0.375, 0.390, 0.435, 0.437,\\
&0.450, 0.445, 0.475, 0.485, 0.515, 0.525, 0.530, 0.595, 0.622, 0.633, 0.635,\\
&0.670, 0.695, 0.715, 0.708, 0.748, 0.790, 0.815, 0.815, 0.825, 0.800, 0.865,\\
&0.885, 0.890, 0.865, 0.905, 0.923, 0.950, 0.920, 0.958, 0.970, 0.967, 0.980,\\
&0.960, 0.980, 0.980, 0.985, 0.990, 0.985, 0.990, 0.998, 1.000, 1.000, 0.995]
\end{aligned}
$$

The displacement of 0.007 is used to set the coordinate origin, $\eta = 0$, at the midpoint of the mean velocity ratio profile, $U/U_{1\infty} = 1/2$.

c. Results

The validation of the turbulence models for the prediction of the mean velocity profile and spreading rate of the mixing layer is shown below. In order to ensure accuracy of the model predictions, these calculations were performed by solving the nondimensional similarity equations described in the appendix. A uniform distribution of 501 points was defined within the grid domain $-0.3 \le \eta \equiv y/x \le 0.2$, the freestream value of the nondimensional turbulent kinetic energy was defined as $K_1 \equiv k_1/U_1^2 = 10^{-6}$ (nearly zero) for the two-equation turbulence models, and the freestream value of the nondimensional turbulent viscosity was varied from $10^{-30} \le N \le 1$. This was also the method used to vary the freestream value of ω or ε for the two-equation turbulence models. The initial mean velocity profile was defined as $U/U_1 = 0.5 + 0.5 \tanh(10\eta)$. The coordinate x was defined as the streamwise coordinate direction with its origin at the virtual origin of the self-similar flow, the coordinate y was defined as the transverse coordinate direction, and U_1 was defined as the freestream speed of one boundary stream while the other freestream was set at rest.

1) Velocity profiles

Figure 7.1 shows the comparison of the predictions of mean velocity profile U/U_1 against $\eta = y/x$ and the experimental data of Liepmann and Laufer (ref. 5). The nondimensional coordinate η was defined with its origin located where the mean velocity ratio was 1/2.

The results of the k-ε and k-ω *SST* models are insensitive to freestream turbulence and show good agreement in the middle of the mixing zone and sharp edge profiles at the boundaries. The small difference between the predictions of these two models near the edge of the freestream at rest is due to the different value of their diffusion model constant, σ_ε. The results of the Spalart-Allmaras model show very good agreement with the experimental data, but show a wider mean velocity profile with very large values of freestream eddy viscosity ($10^{-3} \le N_1 \equiv \nu_t/U_1 x$; see fig. 7.2). In practice, these large values of dimensionless eddy viscosity are much larger than the molecular viscosity, and the errors can be controlled by limiting the eddy viscosity in the freestream, ($\mu_t/\mu_l \le 10^{-3} Re_\infty$). The k-ω model shows two different results of mean velocity profiles, one for low values and another for high values of freestream ω, and a range of profiles in between these two values, ($10^{-2} \le W \equiv \omega x/U_1 \le 10$). The profiles show significant underprediction in the low-speed side and overprediction in the high-speed side of the mixing layer with low freestream ω, ($W \le 10^{-2}$), and underprediction in the higher speed side with high freestream ω, ($W \ge 10$).

2) Spreading rates

The spreading rate provides an estimate of the width of the mixing region and is considered one of the most significant parameters that turbulence models attempt to predict with accuracy. The spreading rate was defined as the distance between the points of the nondimensional variable η in the mean velocity profile where the square of the nondimensional mean velocity ratio is 0.9 and 0.1, respectively. This definition of spreading rate is one of several formulations that have been proposed in the literature to measure the spreading rate. The main shortcoming of this definition is reported to

be the large differences that the models predict near the edge zones of the mixing layer (refs. 17 and 18). The main advantage of this definition is its widespread use in turbulence modeling (refs. 17 and 18).

The following table reports the spreading rate values obtained with the turbulence models and the recommended experimental value. It is to be noted that the experimental value of 0.115 shows an uncertainty of about ±10%.

Mixing layer	Spreading rate
Experiment	0.115
Launder-Sharma k-ε model	0.099
Wilcox k-ω model	0.068–0.143
Menter *SST* model	0.100
Spalart-Allmaras model	0.109

The range of values reported for the k-ω model is due to the effects of low and high freestream ω values. These effects are shown in detail in the following paragraphs and in figure 7.2.

d. Sensitivity analyses

1) Freestream turbulence sensitivity study

Figure 7.2 shows the spreading rates predicted with different freestream values of eddy viscosity, $N \equiv \nu_t/U_1 x = 10^{-n}$. For each turbulence model, a set of simulations was done with different values of the exponent n within the range of $-13 \le n \le 0$. A uniform distribution of 501 points was defined within the grid domain $-0.3 \le \eta = y/x \le 0.2$ in all these simulations, except for the Spalart-Allmaras model for very large values of freestream eddy viscosity where the grid range was increased up to $-5 \le \eta = y/x \le 4$ for $N = 1$.

The predictions of the spreading rate, velocity profile, and eddy viscosity profile with the k-ε and k-ω *SST* models are quite insensitive to freestream turbulence. The k-ω model predictions show a strong sensitivity to freestream turbulence. Large values of freestream ω give a spreading rate of 0.068 and small values of freestream ω give a spreading rate of 0.143. These results are consistent with the far wake predictions presented by Menter (ref. 12) in his discussion over the sensitivity of the k-ω model to freestream conditions. The one-equation model of Spalart-Allmaras shows no sensitivity to freestream turbulence and gives a spreading rate of 0.109 with $N \le 10^{-5}$. For very large freestream eddy viscosity, it predicts larger values up to 1.61 with a nondimensional eddy viscosity of $N = 1$.

2) Grid resolution sensitivity study

A grid sensitivity study for each model was made to provide an estimate of the resolution needed to capture an accurate solution and is shown in figure 7.3. The computations were performed with 50, 100, 150, 300, 500, and 1000 points with a uniform distribution inside the grid domain

$-0.3 \le \eta \le 0.2$. The freestream values of the turbulent kinetic energy and eddy viscosity were set equal to $K_1 = 10^{-6}$ and $N_1 = 10^{-8}$, respectively. The results are presented based on the percent error of spreading rate with respect to the solution obtained using 1000 grid points. In general, the results show that errors can be controlled within less than 3% if 100 grid points are used in the calculations of the mixing layer with the k-ε and the k-ω *SST* models. The *S-A* model shows a smaller sensitivity to grid resolution, while the k-ω model shows a much larger sensitivity to grid resolution.

3) Initial conditions sensitivity study

The models all appeared to show zero sensitivity to different initial profiles, as expected from the usual concept of self-similar profiles. For example, the following table shows the spreading rates with the same six significant figures computed with two different initial velocity profiles, a step function and a hyperbolic tangent profile defined as $U/U_1 = 0.5 + 0.5 \tanh(10\eta)$.

Initial\model	k-ε	k-ω	*SST*	*S-A*
tanh/step function	0.098594	0.067572	0.100237	0.108637

4) Code sensitivity and Mach number sensitivity study

A study of code independence is needed to demonstrate that an accurate solution can be obtained independent of the numerical code—even among codes involving different physical simplifications, such as full Navier-Stokes methods, boundary layer approximations, self-similar approaches, and incompressible versus compressible codes. Five codes with three different numerical methods were used in this study: three self-similar equilibrium method (SSE), one incompressible Navier-Stokes method (INS) (ref. 20), and one compressible Navier-Stokes methods (CNS) (ref. 21). The “standard” solutions for each code were established following the guidelines illustrated in the current section. Figure 7.4 shows the comparison of the results using the one-equation Spalart-Allmaras turbulence model (*S-A*). The mean velocity profiles are similar and code-independent. No significant differences were found in the predictions obtained with the five different numerical codes; they all show similar predictions. The self-similar solutions show similar results with 102, 200, and 500 grid points. The incompressible Navier-Stokes solution obtained with the INS2D code used 101 grid points.

The effect of the freestream Mach number is presented for the benefit of users of compressible Navier-Stokes codes. The comparison in figure 7.4 of the velocity profiles using $M_1 = 0.5$ with the compressible Navier-Stokes code, the incompressible Navier-Stokes code, and the three self-similar equilibrium approximations for the incompressible mixing layer using $M_1 = 0$ showed no significant differences. One SSE predicted a spreading rate about 2% less than the consensus of the other incompressible methods, and the CNS prediction was only 3.7% low even at $M_1 = 0.5$. These differences are much smaller than the 10% observed in the experimental data. Simulations based on Navier-Stokes codes should make sure to determine the self-similar state independent of initial conditions, and should define the virtual origin of the mixing layer based on the flow region where the spreading rate becomes a linear function of the streamwise distance.

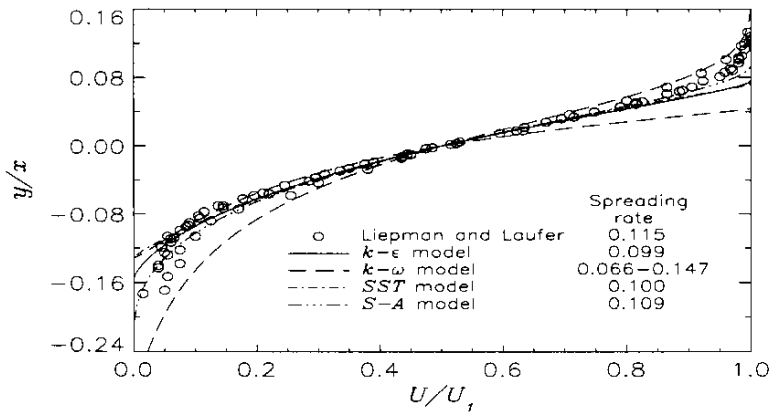

Figure 7.1. Comparison of velocity profiles for mixing layer flow.

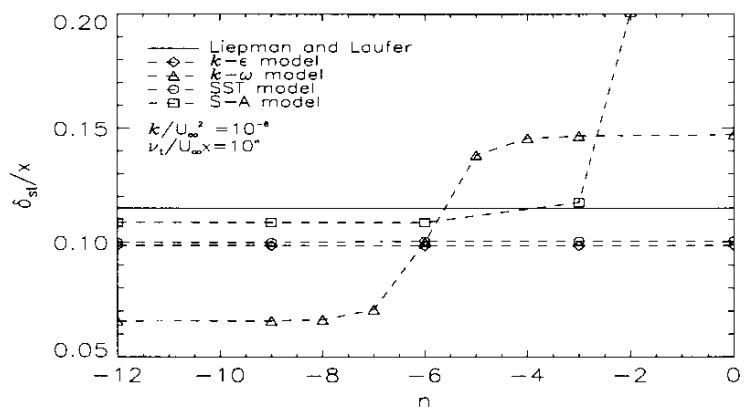

Figure 7.2. Comparison of spreading rate sensitivity to freestream turbulence for mixing layer flow.

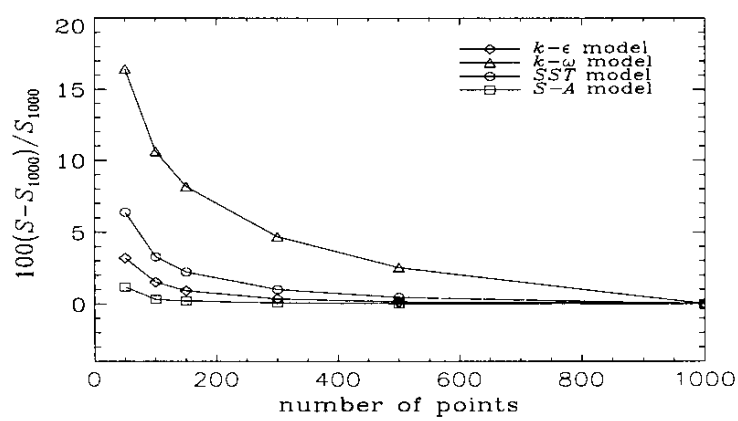

Figure 7.3. Comparison of spreading rate sensitivity to grid resolution for mixing layer flow.

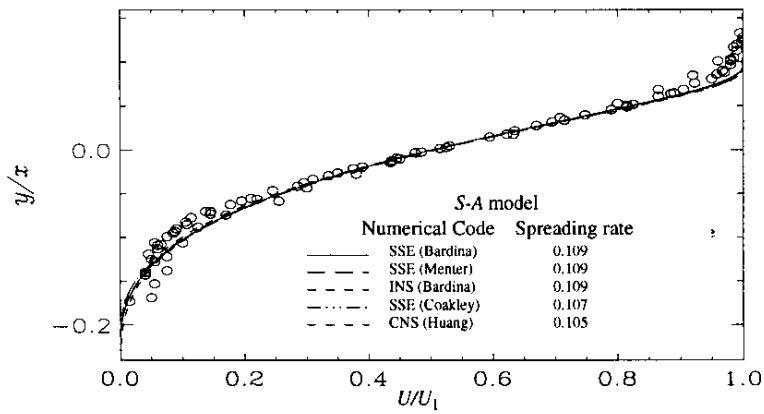

Figure 7.4. Comparison of code sensitivity in the prediction of the velocity profile for mixing layer flow.

Section 8. Plane Jet

a. Introduction

Turbulent plane jets or nearly plane jets are of great interest in engineering design (refs. 3, 4, 22, and 23). Experimental results show that the jet develops an asymptotic nondimensional profile at high Reynolds numbers and far downstream of transition and initial development effects. The experimental data of Bradbury (ref. 23) shows a spreading rate value between 0.10 and 0.11 for a fully developed plane jet. Similar to the other free-shear flows, the mean velocity profile and its spreading rate are considered the most significant parameters for turbulence model predictions.

b. Experimental data

In the present study, the predictions of the turbulence models are compared against the experimental data of Bradbury (ref. 23), whose nondimensional mean velocity profile is

$$y/x = [0.000,\ 0.009,\ 0.018,\ 0.026,\ 0.034,\ 0.035,\ 0.044,\ 0.053,\ 0.061,\ 0.062,\ 0.070,\ 0.079,\ 0.088,\ 0.096,\ 0.097,\ 0.106,\ 0.110,\ 0.110,\ 0.114,\ 0.123,\ 0.123,\ 0.132,\ 0.141,\ 0.142,\ 0.150,\ 0.158,\ 0.167,\ 0.169,\ 0.176,\ 0.185,\ 0.188,\ 0.194,\ 0.202,\ 0.211,\ 0.220]$$

$$U/U_1 = [1.000,\ 0.996,\ 0.983,\ 0.962,\ 0.916,\ 0.933,\ 0.898,\ 0.856,\ 0.784,\ 0.809,\ 0.758,\ 0.703,\ 0.646,\ 0.553,\ 0.588,\ 0.529,\ 0.500,\ 0.468,\ 0.471,\ 0.400,\ 0.414,\ 0.358,\ 0.305,\ 0.284,\ 0.256,\ 0.210,\ 0.168,\ 0.174,\ 0.131,\ 0.099,\ 0.084,\ 0.072,\ 0.050,\ 0.033,\ 0.020]$$

where the mean speed of one freestream is U_1 and the other freestream is at rest, x is the streamwise coordinate direction and y is the transversal coordinate direction, and the center of coordinates is located at the virtual origin of the self-similar flow.

c. Results

The validation metrics of the turbulence models for the prediction of the mean velocity profile and spreading rate of the plane jet are shown below. Consistent with the mixing layer simulations, these calculations were performed by solving the nondimensional similarity equations described in the appendix, achieving fast convergence to machine accuracy. The freestream value of the nondimensional turbulent kinetic energy was also defined as $K_1 \equiv k_1/U_1^2 = 10^{-6}$ (nearly zero) for the two-equation turbulence models, and the nondimensional freestream turbulent viscosity was varied within the range $10^{-15} \le N \le 1$. A uniform distribution of 150 points was defined inside the grid domain within $0 \le \eta \equiv y/x \le 0.35$ for the k-ε, the k-ω *SST*, and the k-ω models. The number of grid points and the domain were increased to 300 and $\eta \le 0.7$ for the k-ω model with low freestream $W \equiv \omega x/U_1 \le 1$. The predictions with the Spalart-Allmaras model also used 300 grid points uniformly distributed within $\eta \le 0.7$ for freestream eddy viscosities $N \le 10^{-2}$, and used 600 grid points and $\eta_{max} = 1.4$ for $N = 0.1$, and 1000 grid points and $\eta_{max} = 6$ for $N = 1$, respectively. The initial mean velocity profile was defined as $U/U_1 = exp(-81\eta^2)$. The coordinate x was defined as the streamwise coordinate direction with its origin at the virtual origin of the self-similar flow, the coordinate y was defined as the transverse coordinate direction, U_1 was defined as the mean speed of one freestream, and the other freestream was set at rest.

1) Velocity profiles

Figure 8.1 shows the comparison of the mean velocity profiles U/U_1 against $\eta \equiv y/x$ and the experimental data of Bradbury (ref. 23). The k-ω *SST* model profile gives excellent agreement with the experimental data and is also insensitive to low freestream values of ω. The profile of the k-ε model is very similar, except near the freestream at rest, and is insensitive to low freestream values of ε. The small difference between the predictions of these two models is due to the different value of their diffusion model constant, σ_ε. The Spalart-Allmaras model overpredicts the mean velocity profile thickness; the results are insensitive to freestream eddy viscosity for $N \equiv \nu_t/U_1 x \leq 10^{-3}$. Results with larger freestream eddy viscosities give much larger overpredictions and are not shown in figure 8.1. In practice, these errors can be controlled by limiting the values of the eddy viscosity in the freestream, ($\mu_t/\mu_l \leq 10^{-3}\, Re_\infty$). The results of the k-ω model show two predictions; one largely overpredicts and the other underpredicts the thickness of the mean velocity profile, corresponding to low and high freestream $W \equiv \omega x/U_1$ values, ($W \leq 10^{-4}$ and $W \geq 10^3$), respectively. This model gives a set of intermediate solutions (not shown in fig. 8.1) depending on the values of freestream ω, ($10^{-4} \leq W \leq 10^3$).

2) Spreading rates

The spreading rate S is defined as the distance of the nondimensional coordinate $\eta \equiv y/x$ between the centerline and the freestream, where the nondimensional velocity is $U/U_1 = 1$ and $U/U_1 = 1/2$, respectively. This definition of spreading rate is one of several formulations that have been proposed.

The following table gives the spreading rate values obtained with the turbulence models and the recommended experimental value. The range of experimental values is reported between 0.10 and 0.11 and is given only as reference values.

Plane jet	Spreading rate
Experiment	0.100–0.110
Launder-Sharma k-ε model	0.108
Wilcox k-ω model	0.092–0.132
Menter *SST* model	0.112
Spalart-Allmaras model	0.143

The k-ε and the k-ω *SST* models give close prediction of the experimental spreading rate, while the Spalart-Allmaras model overpredicts the spreading rate. The k-ω model predicts a range of values due to the effects of low and high freestream ω. These effects are further discussed in the following paragraphs.

d. Sensitivity analyses

1) Freestream turbulence sensitivity study

Figure 8.2 shows the sensitivity of the spreading rates predicted with different freestream values of eddy viscosity, $N \equiv \nu_t/U_1 x = 10^{-n}$, and the values of the exponent n was varied within $-15 \le n \le 0$. The sensitivity of the spreading rate to freestream turbulence is similar in all free-shear flows. The results with the k-ε and k-ω *SST* models are insensitive to low freestream values of ε or ω, respectively. The k-ω model shows a strong sensitivity to freestream ω. Large values of freestream ω give a spreading rate of 0.092, small values of freestream ω give a spreading rate of 0.132, and intermediate values are predicted in between these two limits. The one-equation model of Spalart-Allmaras shows no sensitivity to freestream turbulence with $N \le 10^{-5}$ and gives a larger spreading rate of 0.143; even larger values are predicted with greater nondimensional freestream eddy viscosity of values.

2) Grid sensitivity study

A grid sensitivity study for each model was done to provide an estimation of the resolution needed to capture an accurate solution. The computations were performed with 50, 100, 150, 300, 500, and 1000 points with a uniform distribution inside the grid domain $0 \le \eta \le \eta_{max}$. The value of $\eta_{max} = 0.35$ was defined for the k-ε, *SST*, and k-ω models, and the value of $\eta_{max} = 0.7$ was defined for the *S-A* model. The freestream values of the turbulent kinetic energy and eddy viscosity were set equal to $K_1 = 10^{-6}$ and $N_1 = 10^{-8}$, respectively. The results are presented based on the percent error with respect to the solution obtained using 1000 grid points. Figure 8.3 shows the sensitivity of the model solutions to the number of grid points used in these calculations. In general, errors can be controlled within less than 2% with 50 through 1000 grid points used in the calculations, except for the k-ω model when the number of grid points inside the boundary layer is less than 200.

3) Initial conditions sensitivity study

The predictions of the different models showed zero sensitivity to the initial profiles.

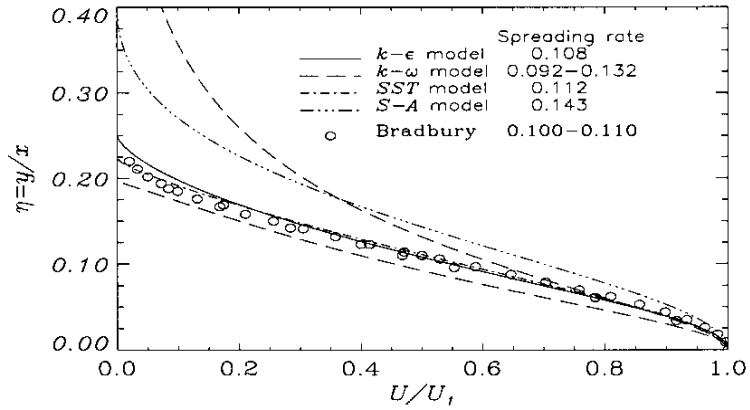

Figure 8.1. Comparison of velocity profiles for plane jet flow.

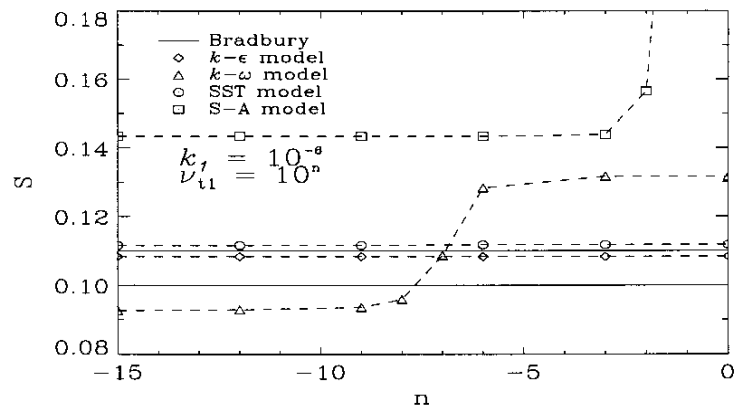

Figure 8.2. Comparison of spreading rate sensitivity to freestream turbulence for plane jet flow.

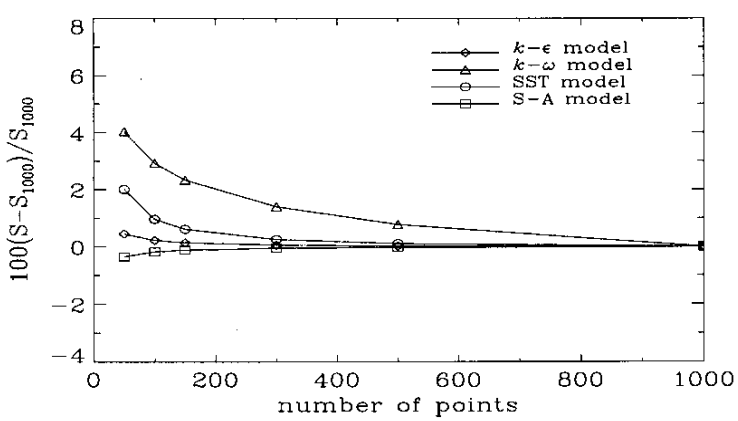

Figure 8.3. Comparison of spreading rate sensitivity to grid resolution for plane jet flow.

Section 9. Round Jet

a. Introduction

Turbulent round or axisymmetric jets are encountered in many aerospace flows (refs. 3, 4, 22, and 24). At high Reynolds numbers and far downstream of transition and initial development effects, the round jet develops an asymptotic equilibrium state. The analysis of the experimental data of Wygnanski and Fiedler (ref. 24) shows a spreading rate value between 0.086 and 0.095 for a fully developed round jet. Similar to other free-shear flows, the mean velocity profile and its spreading rate are considered to be the most significant parameters in turbulence model predictions.

b. Experimental data

In the present study, the predictions of the turbulence models are compared with the experimental data of Wygnanski and Fiedler (ref. 24) whose nondimensional mean velocity profile is

$$y/x = [0.000,\ 0.004,\ 0.005,\ 0.007,\ 0.009,\ 0.015,\ 0.017,\ 0.017,\ 0.019,\ 0.029,\ 0.029,\ 0.030,\ 0.032,\ 0.036,\ 0.038,\ 0.042,\ 0.042,\ 0.049,\ 0.049,\ 0.054,\ 0.058,\ 0.060,\ 0.064,\ 0.066,\ 0.068,\ 0.068,\ 0.076,\ 0.078,\ 0.080,\ 0.081,\ 0.087,\ 0.088,\ 0.096,\ 0.097,\ 0.099,\ 0.102,\ 0.107,\ 0.114,\ 0.115,\ 0.118,\ 0.125,\ 0.128,\ 0.131,\ 0.134,\ 0.137,\ 0.137,\ 0.144,\ 0.145,\ 0.149,\ 0.154,\ 0.160,\ 0.161,\ 0.163,\ 0.173,\ 0.176,\ 0.182,\ 0.185,\ 0.192,\ 0.192,\ 0.197,\ 0.210]$$

$$U/U_1 = [1.000,\ 0.995,\ 0.991,\ 0.989,\ 0.984,\ 0.977,\ 0.973,\ 0.961,\ 0.973,\ 0.918,\ 0.909,\ 0.893,\ 0.900,\ 0.850,\ 0.855,\ 0.832,\ 0.809,\ 0.791,\ 0.775,\ 0.739,\ 0.727,\ 0.700,\ 0.700,\ 0.636,\ 0.641,\ 0.623,\ 0.559,\ 0.555,\ 0.550,\ 0.532,\ 0.500,\ 0.486,\ 0.432,\ 0.439,\ 0.432,\ 0.405,\ 0.375,\ 0.332,\ 0.314,\ 0.300,\ 0.268,\ 0.255,\ 0.241,\ 0.214,\ 0.218,\ 0.205,\ 0.182,\ 0.182,\ 0.145,\ 0.136,\ 0.109,\ 0.114,\ 0.109,\ 0.082,\ 0.073,\ 0.073,\ 0.055,\ 0.050,\ 0.041,\ 0.045,\ 0.027]$$

where the centerline speed of the jet is U_1 and the freestream is at rest, x is the streamwise coordinate direction and y is the transversal coordinate direction, and the center of coordinates is located at the virtual origin of the self-similar flow.

c. Results

The validation of the turbulence models for the prediction of the mean velocity profile and spreading rate of the round jet is shown below. Consistent with the mixing layer simulations, these calculations were performed by solving the nondimensional similarity equations described in the appendix, achieving fast convergence to machine accuracy. A uniform distribution of 300 grid points was defined in the domain $0 \le \eta \equiv y/x \le 7/10$. The freestream value of the nondimensional turbulent kinetic energy was also defined as $K_1 \equiv k_1/U_1^2 = 10^{-6}$ (nearly zero) for the two-equation turbulence models, and the nondimensional freestream turbulent viscosity was varied from $10^{-15} \le N \le 1$ for all the models. The number of grid points and the radial jet distance were increased with the k-ω and the Spalart-Allmaras models for large values of freestream eddy viscosity due to freestream sensitivity, 600 grid points and $\eta_{max} = 1.4$ for $N = 0.1$ and 1000 grid points and $\eta_{max} = 6$ for $N = 1$. The initial mean velocity profile was defined as $U/U_1 = 1.0 - \tanh(10\eta)$. The coordinate x was defined as the streamwise coordinate direction with its origin at the virtual origin of the self-similar flow, the

coordinate y was defined as the transverse coordinate direction with its origin at the center of the jet, U_1 was defined as the centerline mean speed of the jet, and the freestream was set at rest.

1) Velocity profiles

Figure 9.1 shows the comparison of the predictions of mean velocity profile U/U_1 against $\eta = y/x$ and the experimental data of Wygnanski and Fiedler (ref. 4). All the models overpredict the thickness of the experimental mean velocity profile. This classical anomaly is well known in these models that have been fine-tuned with empirical data of mixing layer, plane jet, and/or far wake experiments.

The results of the k-ε and k-ω *SST* models are closer to the experimental data and are also insensitive to low freestream values of ε or ω, respectively. The small difference between the predictions of these two models near the edge of the freestream is also due to the different value of their diffusion model constant, σ_ε. The Spalart-Allmaras model gives a considerably larger overprediction of the mean velocity profile thickness, and the results are insensitive to freestream eddy viscosity for $N \equiv \nu_t/U_1 x \leq 10^{-3}$. Results with larger freestream eddy viscosities give much larger overpredictions and are not shown in figure 9.1. In practice, these large values of dimensionless eddy viscosity are much larger than the molecular viscosity, and the errors can be controlled by limiting the eddy viscosity in the freestream, ($\mu_t/\mu_l \leq 10^{-3}\, Re_\infty$). The results of the k-ω model show two overpredictions of the thickness of the mean velocity profile, corresponding to low and high freestream $W \equiv \omega x/U_1 x$ values, ($W \leq 10^{-4}$ and $W \geq 10^4$), and a set of intermediate solutions (not shown in fig. 9.1) depending on the values of freestream ω, ($10^{-4} \leq W \leq 10^4$).

2) Spreading rate

The spreading rate is defined as the value of the nondimensional jet radius, $S = y/(x - x_o)$, where the mean speed is half its centerline value. This definition of spreading rate is one of several formulations that have been proposed. The spreading rate provides an estimate of the thickness of the round jet and is widely used in turbulence modeling. However, it is only one parameter and it does not provide information about the shape of the velocity profile.

The following table reports the spreading rate obtained with the turbulence models and the recommended experimental value. The range of experimental values is between 0.086 and 0.095.

Round jet	Spreading rate
Experiment	0.086–0.095
Launder-Sharma k-ε model	0.120
Wilcox k-ω model	0.169–0.356
Menter *SST* model	0.127
Spalart-Allmaras model	0.253

All models overpredict the spreading rate. The range of values reported for the k-ω model is due to the effects of low and high freestream ω values.

d. Sensitivity analyses

1) Freestream turbulence sensitivity study

Figure 9.2 shows the sensitivity of the spreading rates predicted with different freestream values of eddy viscosity, $N \equiv \nu_t/U_1 x = 10^{-n}$, and the values of the exponent n was varied within $-15 \le n \le 0$. A uniform distribution of 300 grid points inside the domain $0 \le \eta = y/x \le 0.7$ was set in all these simulations, except for the models with large freestream sensitivity (see fig. 9.1).

For a given model, the sensitivity of the spreading rate to freestream turbulence is similar in all freeshear flows. The results with the k-ε and k-ω *SST* models are insensitive to low freestream values of ε or ω, respectively. The k-ω model shows a strong sensitivity to freestream ω, large values of freestream ω give a spreading rate of 0.068, small values of freestream ω give a spreading rate of 0.143, and intermediate values are predicted in between these two limits. The one-equation model of Spalart-Allmaras shows no sensitivity to freestream turbulence with $N \le 10^{-5}$ and gives a spreading rate of 0.109, but larger values are predicted with very large freestream eddy viscosity values, $N > 10^{-3}$; in other words, when $\mu_t/\mu_l > 10^{-3}\, Rex_\infty$.

2) Grid sensitivity study

Figure 9.3 shows a grid sensitivity study for each model, which provides an estimate of the resolution needed to capture an accurate solution. The computations were performed with 50, 100, 150, 300, 500, and 1000 grid points with a uniform distribution inside the domain $0 \le \eta \le \eta_{max}$, where $\eta_{max} = 0.35$ except for the Spalart-Allmaras model where $\eta_{max} = 0.70$. The freestream values of the turbulent kinetic energy and eddy viscosity were set equal to $K_1 = 10^{-6}$ and $N_1 = 10^{-8}$, respectively. The results are presented based on the percent error with respect to the spreading rate obtained with 1000 grid points. In general, errors can be controlled within less than 2% with 50 through 1000 grid points used in the calculations.

3) Initial conditions sensitivity study

Similar to the results of other free-shear flows, all the models showed zero sensitivity to different initial profiles.

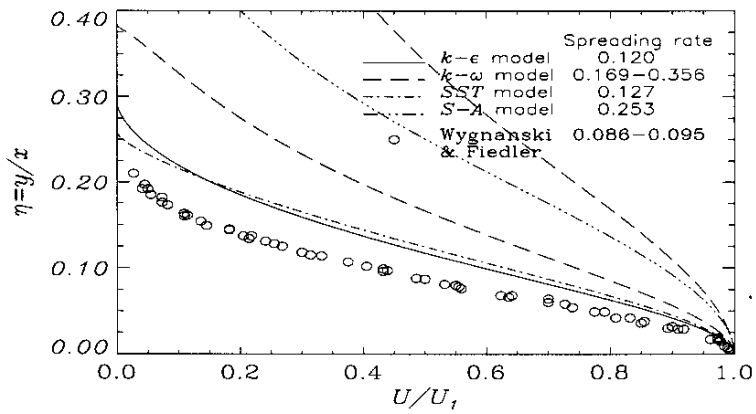

Figure 9.1. Comparison of velocity profiles for round jet flow.

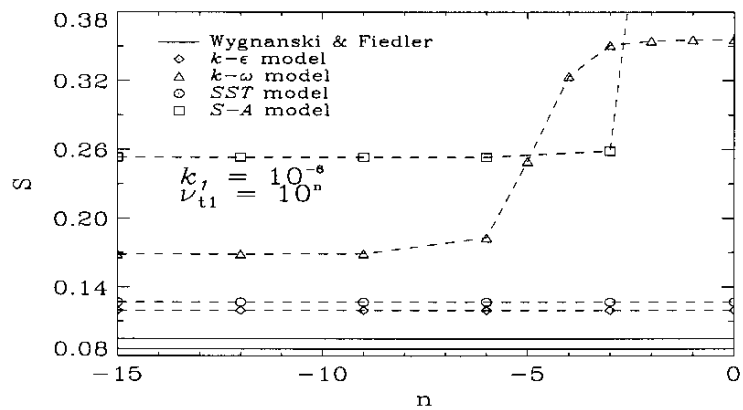

Figure 9.2. Comparison of spreading rate sensitivity to freestream turbulence for round jet flow.

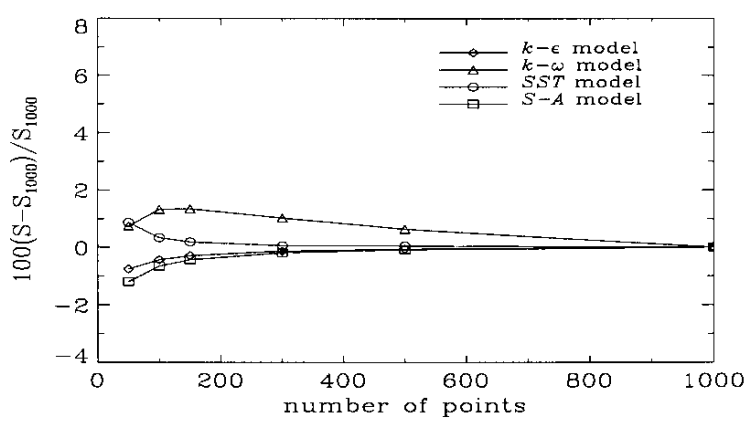

Figure 9.3. Comparison of spreading rate sensitivity to grid resolution for round jet flow.

Section 10. Plane Wake

a. Introduction

Turbulent plane wakes are encountered in many aerodynamic flows (figs. 3, 4, 22, 25, and 26). Similar to other free-shear flows, experimental results show that the wake develops an asymptotic nondimensional profile far downstream of transition and initial development effects. For turbulence modeling, the mean velocity profile and its spreading rate are also considered the most significant parameters. The analysis of the experimental data of Fage and Falkner (ref. 25) shows an spreading rate of 0.365 for a fully developed plane wake.

b. Experimental data

In the present study, the predictions are compared against the experimental data of Fage and Falkner (ref. 25) whose mean velocity profile is defined as

$$\eta = [0.101,\ 0.109,\ 0.118,\ 0.139,\ 0.214,\ 0.221,\ 0.231,\ 0.252,\ 0.331,\ 0.335,\ 0.344,\ 0.373,\ 0.444,\ 0.452,\ 0.456,\ 0.489,\ 0.556,\ 0.568,\ 0.609,\ 0.669,\ 0.669,\ 0.688,\ 0.730,\ 0.737,\ 0.778]$$

$$(U - U_{min})/(U_\infty - U_{min}) = [0.923,\ 0.928,\ 0.916,\ 0.899,\ 0.725,\ 0.715,\ 0.686,\ 0.719,\ 0.479,\ 0.467,\ 0.481,\ 0.444,\ 0.323,\ 0.290,\ 0.300,\ 0.243,\ 0.150,\ 0.145,\ 0.107,\ 0.075,\ 0.052,\ 0.044,\ 0.030,\ 0.020,\ 0.014]$$

where $\eta = y(\rho U_\infty/Dx)^{1/2}$ and $(U - U_{min})/(U_\infty - U_{min})$, the centerline speed of the wake is U_{min}, the mean speed of both freestreams is U_∞, x is the streamwise coordinate direction with its origin at the virtual origin of the self-similar flow and y is the transversal coordinate direction, ρ is the fluid density, and D is the total wake drag or momentum deficit (integrated over the full wake width).

c. Results

The validation metrics of the turbulence models for the prediction of the mean velocity profile and spreading rate of the far wake are shown below. Consistent with the mixing layer simulations, these calculations were performed by solving the nondimensional similarity equations described in the appendix, achieving fast convergence to machine accuracy. The freestream value of the nondimensional turbulent kinetic energy was also defined as $K_1 \equiv k_1/U_1^2 = 10^{-6}$ (nearly zero) for the two-equation turbulence models, and the nondimensional freestream turbulent viscosity was varied within the domain $10^{-15} \le N \le 1$. Based on the predicted spreading rate of the mean velocity profile, a uniform distribution of 300 grid points was defined in the domain $0 \le \eta \le 2$ to simulate flows with high freestream eddy viscosity, $N \ge 0.01$, and 150 grid points within the domain $0 \le \eta \le 1$ to simulate flows with lower freestream eddy viscosity. The initial mean velocity profile was defined as the following exponential function $(U - U_{min})/(U_\infty - U_{min}) = exp(-2\eta^2)$. See reference 4 for details on using the displacement thickness as an integral constraint in computing the mean velocity profile.

1) Velocity profiles

Figure 10.1 shows the mean velocity profiles $(U - U_{min})/(U_\infty - U_{min})$ versus the nondimensional coordinate $\eta = y(\rho U_\infty/Dx)^{1/2}$ compared with the experimental data of Fage and Falkner (ref. 25). The k-ε and k-ω *SST* models give thinner profiles than experiment and are insensitive to low freestream values of ε or ω, respectively. The small difference between the predictions of these two models near the freestream is due to the different value of their diffusion model constant, σ_ε. The Spalart-Allmaras model gives best agreement with the experimental profile, and the results are insensitive to freestream eddy viscosity for $N \equiv \nu_t/U_\infty x \leq 10^{-4}$. Results with much larger freestream eddy viscosities give overpredictions and are not shown in figure 10.1; in practice, these errors can be controlled by limiting the eddy viscosity in the freestream, $(\mu_t/\mu_l \leq 10^{-3}\, Re_\infty)$. The results of the k-ω model show two predictions; one largely overpredicts and the other underpredicts the thickness of the mean velocity profile, corresponding to low and high freestream $W \equiv \omega x/U_\infty$ values, ($W \leq 10^{-4}$ and $W \geq 10^3$), respectively. This model gives a set of intermediate solutions (not shown in fig. 10.1) depending on the intermediate values of freestream ω, ($10^{-4} \leq W \leq 10^3$).

2) Spreading rate

The spreading rate S is defined as the difference $S = \eta_{0.5} - \eta_0$ of the nondimensional coordinate η between the points where the nondimensional mean speed is one half and zero, respectively. This definition of spreading rate is one of several formulations that have been proposed and it is widely used in turbulence modeling.

The following table reports the spreading rate obtained with the turbulence models and the recommended experimental value 0.365 of Fage and Falkner (ref. 25).

Far wake	Spreading rate
Experiment	0.365
Launder-Sharma k-ε model	0.255
Wilcox k-ω model	0.209–0.494
Menter *SST* model	0.257–0.260
Spalart-Allmaras model	0.339

The k-ε and the k-ω *SST* models underpredict the experimental spreading rate by 30%, while the Spalart-Allmaras model gives a value much closer to the experimental spreading rate (7%). The k-ω model predicts a range of values due to the effects of low and high freestream ω, within an underprediction of 43% and an overprediction of 35%.

d. Sensitivity analyses

1) Freestream turbulence sensitivity study

Figure 10.2 shows the sensitivity of the spreading rates predicted with different freestream values of eddy viscosity, $N \equiv \nu_t/U_1 x = 10^{-n}$, and the values of the exponent n was varied within $-10 \le n \le 0$. The results with the k-ε and k-ω *SST* models are insensitive to low freestream values of ε or ω, respectively. The k-ω model shows a strong sensitivity to freestream ω, large values of freestream ω give a spreading rate of 0.209, small values of freestream ω give a spreading rate of 0.494, and intermediate values are predicted in between these two limits. The one-equation model of Spalart-Allmaras shows no sensitivity to freestream turbulence with $N \le 10^{-4}$ and predicts a spreading rate of 0.339, which gives best agreement with experiment.

2) Grid sensitivity study

A grid sensitivity study for each model is recommended to provide an estimation of the resolution needed to capture an accurate solution. The computations were performed with 50, 100, 150, 300, 500, and 1000 grid points with a uniform distribution inside the domain $0 \le \eta \le \eta_{max}$. The value of $\eta_{max} = 1$, freestream turbulent kinetic energy $K_\infty = 10^{-6}$, and freestream eddy viscosity $N_\infty = 10^{-8}$ were defined for all the models. Figure 10.3 shows the sensitivity of the model solutions to the number of grid points used in the calculations. The results are reported based on the percent error with respect to the solution obtained using 1000 grid points. Figure 10.3 shows the sensitivity of the model solutions to the number of grid points used in the calculations. In general, errors can be controlled within less than 2% with 50 through 1000 grid points used in the calculations, except for the k-ω model when the minimum number of grid points is about 400.

3) Initial conditions sensitivity study

The predictions of the different models showed zero sensitivity to the initial profiles.

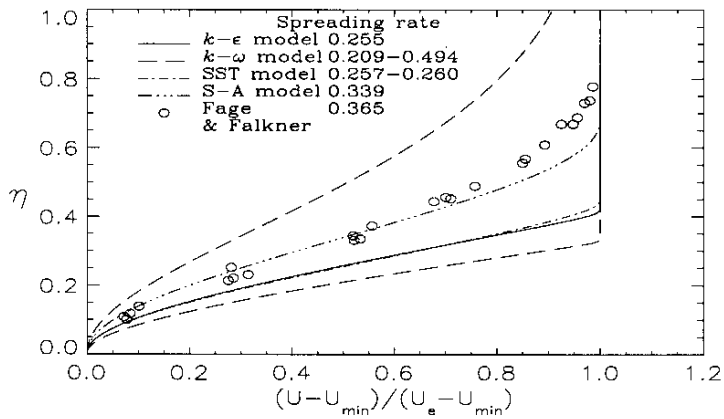

Figure 10.1. Comparison of velocity profiles for plane wake flow.

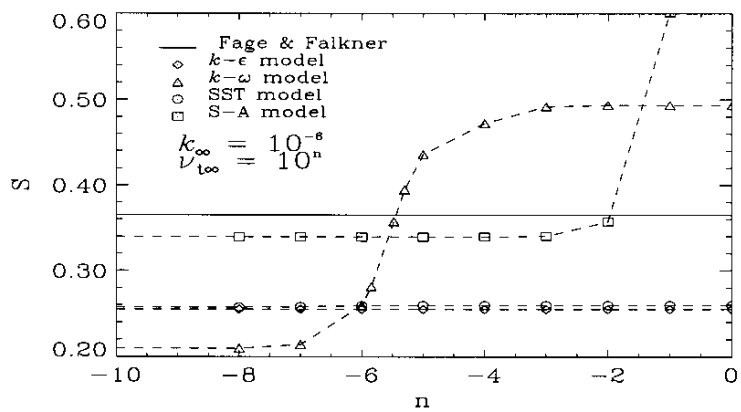

Figure 10.2. Comparison of spreading rate sensitivity to freestream turbulence for plane wake flow.

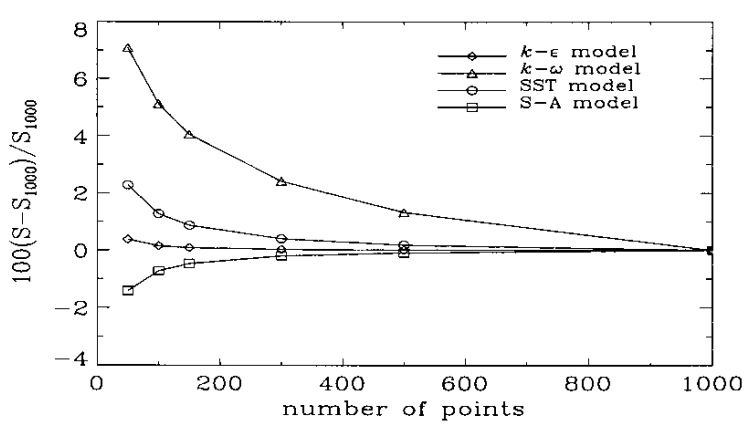

Figure 10.3. Comparison of spreading rate sensitivity to grid resolution for plane wake flow.

Section 11. Compressible Mixing Layer

a. Introduction

The compressible turbulent mixing layer is present in many aerodynamic flows and is of considerable interest in engineering design. It is a fundamental flow for studying compressibility effects in the modeling of turbulence (refs. 18 and 27–29). At high Reynolds numbers and far downstream of transition and initial condition effects, the mixing layer develops an asymptotic equilibrium state. The analysis of the experimental data in the Free Turbulent Shear Flow conference held at NASA Langley Research Center was reported by Birch and Eggers (refs. 18 and 28) and shows a decrease of the spreading rate with increasing convective Mach number; these data are known as the "Langley curve." The spreading rate and the shape of the mean velocity profile are considered significant parameters for prediction.

b. Experimental data

Model validation requires a careful comparison of predictions and experimental data and a proper mathematical and numerical formulation of the governing equations. Experimental data reveal that the initial development of the mixing layer is sensitive to initial conditions of flow structures, boundary conditions imposed by flow geometry, and Reynolds number effects. In the later development or far field, the available experimental data for fully developed mixing layer flows at high Reynolds numbers show a unique self-similar profile with an asymptotic spreading rate (refs. 28 and 29).

The experimental results of Samimy and Elliot on mean velocity profiles show the self-similar profiles of the mixing layer. These experimental results are compiled and tabulated in the database of Settles and Dodson (ref. 29) in a study of 45 experiments on free-shear flows.

The experimental results of spreading rate show a decrease of the thickness of the mixing layer with increasing convective Mach number, M_c. $M_c = (U_1 - U_2)/(a_1 + a_2)$ is defined in terms of the mean velocity, U, and the sound speed, a, in each freestream. Experimental data are available with different freestream velocities in the low- and high-speed sides of the mixing layer, and with constant total or static temperature. The compilation of different experimental results with the low-speed freestream at rest and constant total temperature are represented by the "Langley data" with high speed freestream Mach number M_1 and spreading rate S as

$$M_1 = [0.0,\ 0.5,\ 1.0,\ 1.5,\ 2.0,\ 2.5,\ 3.0,\ 3.5,\ 4.0,\ 4.5,\ 5.0]$$

$$S = [0.115,\ 0.115,\ 0.1106,\ 0.08275,\ 0.0632,\ 0.05182,\ 0.0446,\ 0.04052,\ 0.03798,\ 0.03563,\ 0.03395]$$

For perfect gases with constant pressure and total temperature, the corresponding convective Mach numbers are

$$M_c = [0,\ 0.247,\ 0.477,\ 0.681,\ 0.854,\ 1.000,\ 1.122,\ 1.225,\ 1.312,\ 1.386,\ 1.450]$$

and the convective Mach number reduces to $M_c = (U_1 - U_2)/(a_1 + a_2) = (M_1R - M_2)/(R + 1)$ where $R^2 = \rho_2/\rho_1$ and $R^2 = [1 + 0.5(\gamma - 1)M_2^2]/[1 + 0.5(\gamma - 1)M_1^2]$. The spreading rate S is defined based on the energy thickness definition of Birch and Eggers (ref. 28) as the difference between the values of y/x where $(U - U_2)^2/(U_1 - U_2)^2$ is 9/10 and 1/10.

The experimental results of Liepmann and Laufer (ref. 19) for the mixing layer of an incompressible fluid are reported in section 8 and are also used here as reference data.

c. Results

The validation results of the turbulence models for the prediction of the mean velocity profile and spreading rate of the compressible mixing layer are shown below. In the present simulations, a uniform distribution of 501 grid points was defined within the domain $-0.3 \le \eta = y/x \le 0.2$, where x is the streamwise coordinate direction with its origin at the virtual origin of the self-similar flow, and y is the transverse coordinate direction. The nondimensional mean variables U, M, a, K, and N denote mean velocity, Mach number, sound speed, turbulent kinetic energy, and eddy viscosity, respectively. The subscripts 1 and 2 stand for the high- and low-speed side of the freestreams, respectively. The freestream value of the nondimensional turbulent kinetic energy was defined as $K_1 \equiv k_1/U_1^2 = 10^{-6}$ (nearly zero) for the two-equation turbulence models. The freestream value of the nondimensional turbulent viscosity was varied between $10^{-15} \le N \equiv \nu_t/(U_1 x) \le 1$ for freestream analysis or was set equal to $N = 10^{-9}$ (also nearly zero) for analysis with constant freestream conditions. The convective Mach number M_c was varied between the range 0 and 6.5, and the freestream velocity in the low-speed side was set equal to zero, $U_2 = 0$. The initial velocity profile ratio was defined as $U/U_1 = 0.5(1.0 + \tanh(10\eta))$.

1) Velocity profiles

Figure 11.1 shows the comparison between the predictions of the nondimensional mean velocity profile $(U - U_2)/(U_1 - U_2)$ of the mixing layer using the standard turbulence models and the experimental data of Samimy and Elliot against the coordinate $(\eta - \eta_{0.5})/\delta_\omega$. This particular coordinate system is used in order to show all the data in a simpler plot. The nondimensional coordinate $\eta \equiv y/x$, the coordinate $\eta_{0.5}$ represents the point where the nondimensional speed is 0.5, and δ_ω is the vorticity thickness of the mixing layer where $\delta_\omega = (U_1 - U_2)/(\mathrm{d}U/\mathrm{d}\eta)_{max}$. The experimental data are shown with convective Mach numbers of $M_c = 0.51$, 0.64, and 0.86. The experimental data of Liepmann and Laufer (ref. 19) for the incompressible mixing layer, $M_c = 0$, is also shown in this figure as a reference. The numerical predictions with the four different turbulence models were obtained over a wide range of convective Mach numbers, and figure 11.1 shows the predictions with $M_c = 0$, 0.8, and 1.6. The vertical arrows indicate the trend of the predictions with increasing convective Mach number.

All velocity profiles show some degree of agreement with the experimental data due to the particular coordinate system of the plot. These plot coordinates bound the range and collapse all data at the midpoint. The results of the k-ε and k-ω *SST* models show good agreement with the nondimensional shape of the experimental profile. The results of the Spalart-Allmaras model also show good agreement with the experimental data, except for very high freestream eddy viscosity. The mean velocity profiles of the k-ω model show sensitivity to low freestream ω values. The relative good agreement of prediction with data is due to the use of δ_ω in the nondimensional plots. The dimensional profiles and spreading rates show a much stronger dependence on Mach number, as will be seen in subsection d.

2) Spreading rate

In the self-similar region, the thickness of the mixing layer grows linearly with downstream distance and the spreading rate is constant. In Navier-Stokes simulations with Cartesian coordinate systems, (x,y), the spreading rate S is defined as $d\delta/dx$ where $\delta(x)$ is the thickness of the mixing layer. In nondimensional self-similar coordinates, $(x,\eta = y/x)$, the spreading rate S becomes simply the transformed nondimensional thickness of the layer $S = \delta$.

Several formulations have been proposed to measure the thickness of the mixing layer. The most well-known formulation is the energy thickness used by Birch and Eggers (ref. 3) in the 1980–81 AFOSR-HTTM-Stanford Conference on Complex Turbulent Flows. In this definition, the thickness δ is defined as the difference between the values of y/x where $(U - U_2)^2/(U_1 - U_2)^2$ is 9/10 and 1/10.

There are other well-known definitions to measure the thickness of the mixing layers (refs. 19 and 30). One of them is Bogdanoff's vorticity thickness, $\delta_\omega = (U_1 - U_2)/(dU/d\eta)_{max}$, and another is Roshko's pitot thickness, where δ_{pt} is defined as the difference between the values of y/x where the pitot pressure is 0.95 and 0.05. Two other correlation techniques for comparing spreading rates were also assessed by Viegas and Rubesin (ref. 30). One is based on Roshko's pitot thickness and is defined as $G(M_c) = S(U_1 + U_2R)/((U_1 - U_2)(1 + R)$ where $R^2 = \rho_2/\rho_1$, and the other one is based on Bogdanoff's vorticity thickness and is defined as $C_\omega(M_c) = S(U_1 + U_2)(U_1 - U_2)$. These different definitions of spreading rates were tested and showed no significant differences in the comparison between the four model predictions and the experimental Langley data.

Figure 11.2 shows the comparison of spreading rates predicted with the four turbulence models with no compressibility corrections and the experimental Langley data. The predicted results are shown with lines and the experimental data are shown with symbols. The most significant result is that all models fail to predict the experimental data on the decrease of spreading rate with increasing convective Mach number. This is a well-known weakness of present turbulence models.

It is well known that present turbulence models fail to predict the decrease of spreading rate with increasing convective Mach numbers shown by experiment. Recently, model corrections have been proposed by Sarkar et al., Zeman, and Wilcox (see ref. 4). These corrections add an additional term for the dilitation-dissipation of turbulent kinetic energy and improve the predictions of spreading rates in better agreement with experiment (ref. 4). Figures 11.3a, 11.3b, and 11.3c show the comparison between the predicted results of the k-ε, k-ω, and *SST* k-ω turbulence models including the dilitation-dissipation model of Sarkar et al. and the compilation of experimental Langley data. There are several factors that have to be considered in the analysis of these results. Figure 11.3a shows the results of the spreading rate nondimensionalized with the corresponding spreading rate value predicted by each model for the incompressible mixing layer; this is normally done in reporting spreading rate values for the compressible mixing layer. All models show very similar predictions with a decrease of spreading rate and overprediction of the experimental data with increasing M_c. One additional effect that has to be considered is the sensitivity of the predictions of the k-ω model with lower freestream values of ω. Figure 11.3b shows the range of spreading rates predicted with high and low values, and an intermediate value of freestream ω. The agreement with experiment seems to improve with lower values of freestream ω. However, all the models predict very different values of spreading rate for the incompressible mixing layer, and this fact should be considered to obtain an accurate representation of the predictions. Figure 11.3c shows the comparison of the actual predictions of

spreading rates and the compilation of experimental Langley data. The spreading rates predicted with the k-ε and *SST* k-ω models show an intermediate value of the experimental data range and much less sensitivity to M_c than the experimental data. The predictions of the k-ω model show strong freestream sensitivity in the presence of low M_c, and the predictions show better agreement and less freestream sensitivity in the presence of high M_c.

d. Sensitivity analyses

1) Freestream turbulence sensitivity study

The sensitivity of the model predictions to their freestream boundary values is shown below. Figure 11.4 shows the variation of the spreading rates obtained with different freestream values of the eddy viscosity. The simulations are based on the conditions of the experiment of Samimy and Elliot (refs. 4, 29, and 31) with $M_c = 0.86$, freestream Mach numbers of 3.07 and 0.46, freestream density ratio of 0.36, and located at $x = 210$ mm downstream of the initial mixing zone. The simulations use a uniform distribution of 300 grid points within the domain $-1/10 \le \eta \le 1/10$. The freestream values of the nondimensional turbulent viscosity $N = 10^{-n}$ varied with $-13 \le n \le 0$.

The spreading rates predicted with the k-ε and *SST* models are quite insensitive to freestream turbulence. Both models underpredict the experimental data $S = 0.105$, results that are consistent with those reported in figure 11.1. The k-ε model predicts an spreading rate of 0.062, and the *SST* model predicts an spreading rate of 0.063-0.064. The k-ω model predictions show a strong sensitivity to freestream turbulence. Small freestream eddy viscosity values predict a spreading rate of 0.042, large freestream eddy viscosity values predict a spreading rate of 0.154, and intermediate values are predicted in between these two limits. The one-equation model of Spalart-Allmaras predicts a spreading rate of 0.059 with $N \le 10^{-3}$ and increases only with very large values of freestream turbulence, up to a value of 0.136 with a nondimensional eddy viscosity of $N = 1$.

The sensitivity of the turbulence models to freestream turbulence on the spreading rate of the mixing layer of compressible fluids is consistent with the results obtained for free-shear flows of incompressible fluids.

2) Grid sensitivity study

A grid sensitivity study for each model is recommended to provide an estimation of the resolution needed to capture an accurate solution. The computations were performed with 50, 100, 150, 300, 500, and 1000 grid points with a uniform distribution inside the domain $-1/10 \le \eta \le 1/10$. The simulations are based on the conditions given in the previous subsection c.

Figure 11.5 shows the sensitivity of the model solutions to the number of grid points used in the calculations. The predictions obtained with the four turbulence models are reported based on the percent errors with respect to the solution obtained using 1000 grid points. In general, errors can be controlled within less than 2% if 100 grid points or more are used in the calculations of the mixing layer with the k-ε, *SST*, and *S-A* models. The k-ω model shows larger sensitivity to grid resolution, and errors greater than 2% were obtained in the simulations with less than 500 grid points.

3) Initial conditions sensitivity study

The results of mean velocity profiles and spreading rates obtained with each one of the turbulence models and different initial profiles showed no differences with the results shown in figures 11.1, 11.2, and 11.3. The initial velocity profiles were varied using different initial profiles, from a step function shape defined by the freestream states, up to an smooth hyperbolic tangent profile, $U/U_1 = 0.5 + 0.5\tanh(10\eta)$ with different freestream conditions.

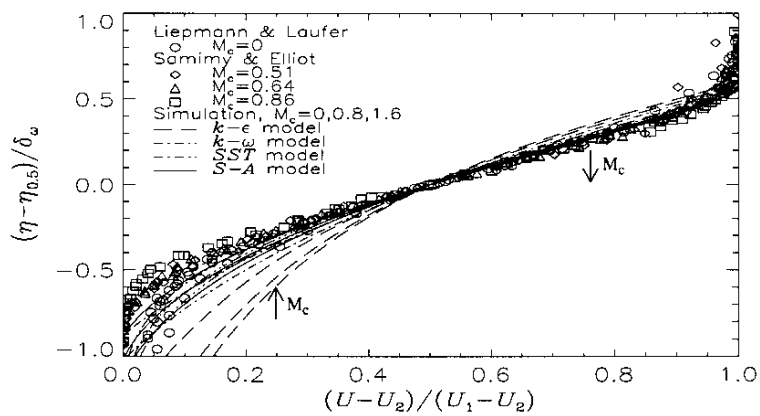

Figure 11.1. Comparison of velocity profiles for compressible mixing layer.

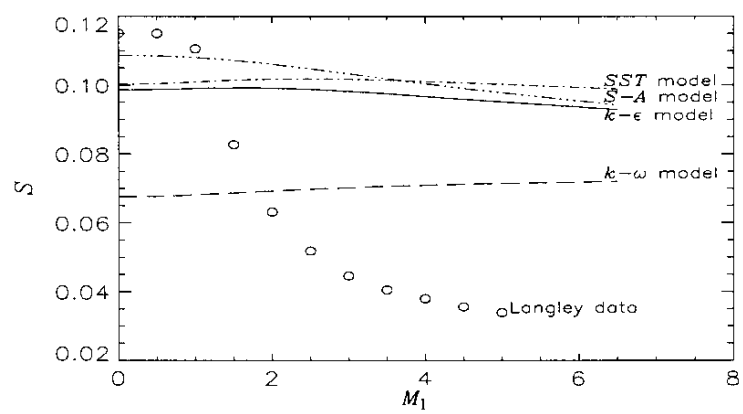

Figure 11.2. Comparison of spreading rate of the mean velocity profile for compressible mixing layer.

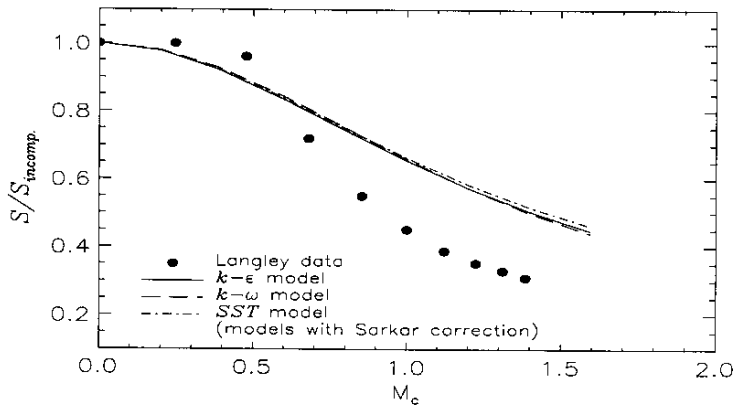

Figure 11.3a. Comparison of spreading rate of the mean velocity profile for compressible mixing layer.

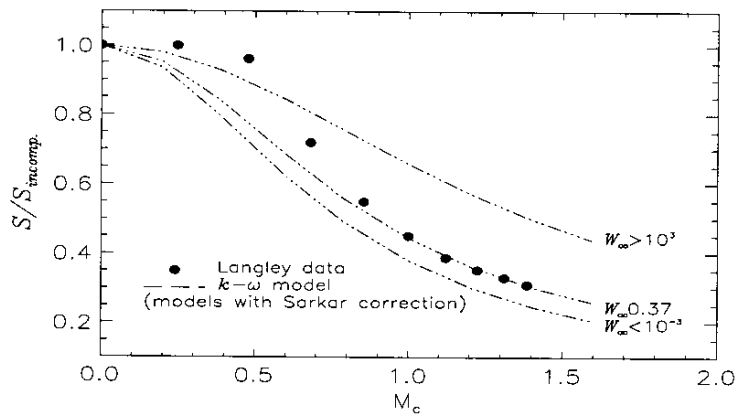

Figure 11.3b. Comparison of spreading rate of the mean velocity profile for compressible mixing layer.

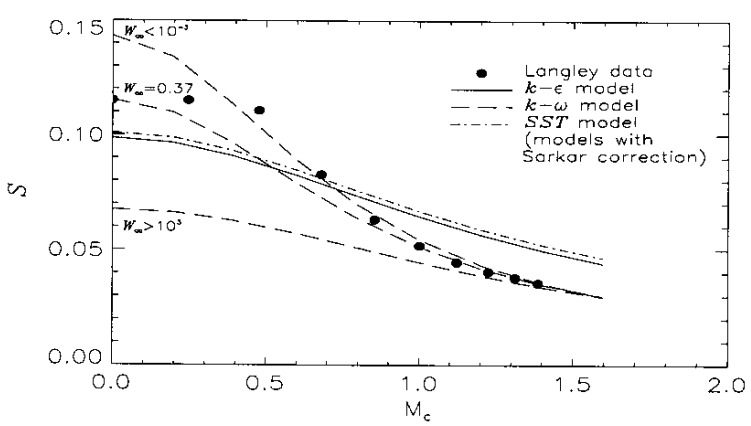

Figure 11.3c. Comparison of spreading rate of the mean velocity profile for compressible mixing layer.

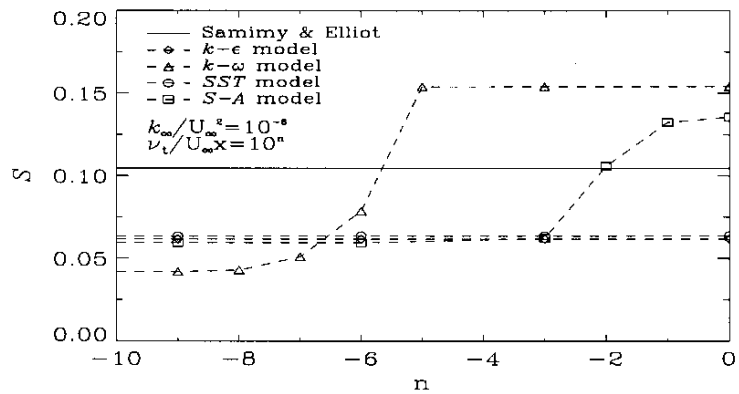

Figure 11.4. Comparison of spreading rate sensitivity to freestream turbulence for compressible mixing layer.

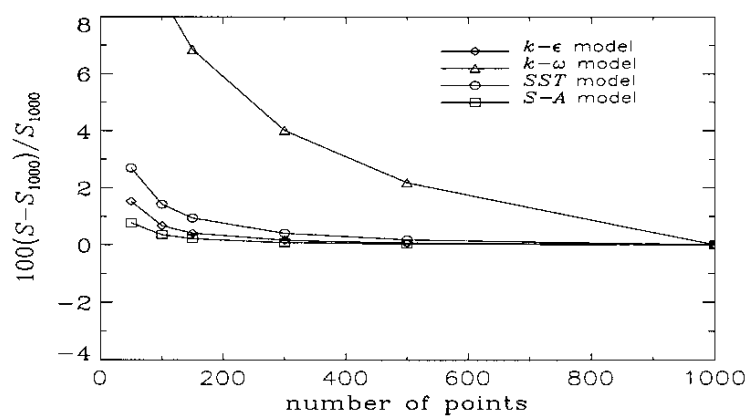

Figure 11.5. Comparison of spreading rate sensitivity to grid resolution for compressible mixing layer.

Part D. Attached and Separated Turbulent Boundary Layer Flows

The turbulent flows included in this study are the flow over an adiabatic flat plate of an incompressible fluid and a compressible fluid at Mach 5, the adverse pressure gradient flow on an axisymmetric cylinder, the shock/boundary layer flow on an axisymmetric bump, and a transonic flow on the RAE 2822 airfoil. The present list of flows is shown below.

Unless it is otherwise stated, the code used in this study is the compressible Navier Stokes code of Huang and Coakley, TURCOM. A detailed discussion of this code is given in reference 32.

Section 12.	Incompressible Boundary Layer
Section 13.	Compressible Flat Plate Flow
Section 14.	Axisymmetric Boundary Layer with Adverse Pressure Gradient
Section 15.	Transonic Separation Flow over an Axisymmetric “Bump”
Section 16.	RAE 2822 airfoil

Section 12. Incompressible Boundary Layer

a. Empirical correlations of data

The incompressible "flat plate" (zero pressure gradient) boundary layer far enough downstream of transition can be defined by any one thickness parameter: the standard is the momentum-thickness Reynolds number $Re_\theta \equiv U_e\theta/\nu$. The model predictions will be compared with the following empirical correlations of mean velocity profile and skin friction.

The similarity laws can be explicitly displayed by Coles' mean velocity profile (refs. 33 and 34) as

$$\frac{U}{u_\tau} = \frac{1}{\kappa}\ln\left(\frac{yu_\tau}{\nu}\right) + C + \frac{2\Pi}{\kappa}\left(\sin\left(\frac{\pi}{2}\frac{y}{\delta}\right)\right)^2 \tag{12.1}$$

where δ is the boundary layer thickness. Coles took the von Kármán constant κ as 0.41 and the additive constant in the logarithmic law as 5.0 and tabulated the "wake parameter" Π, which he chose to asymptote to 0.55 at $Re_\theta > 5000$. Coles' tabulation (ref. 34) only goes up to $Re_\theta = 29000$ but his formulas have been used for higher Reynolds number, assuming Π = constant = 0.55.

The von Kármán-Schoenherr correlation

$$c_f = \frac{1}{17.08\,(\log Re_\theta)^2 + 25.11\log Re_\theta + 6.012} \tag{12.2}$$

is a good approximation for skin friction. The experimental uncertainty for skin friction is at least ±2%, and this correlation agrees with that of Coles to within this uncertainty (see table 12.1) when θ and Re_θ are determined by integrating Coles' law.

Table 12.1. Skin friction coefficients

Re_θ	2000	5000	10000	20000	50000	100000
c_f (K-S)	0.003636	0.003007	0.002633	0.002326	0.001996	0.001790
c_f (Coles)	0.003658	0.002980	0.002630	0.002342	0.002028	0.001829
$H \equiv \delta^*/\theta$ (Coles)	1.404	1.358	1.324	1.297	1.269	1.251

Note, however, that several authors have suggested that Π decreases as Re_θ increases above 15000 or so. Fortunately, the skin friction coefficient is not very sensitive to the exact value of Π at high Reynolds numbers. A 10% decrease in Π will result in only 1.43% and 1.18% increase in skin friction coefficient for $Re_\theta \approx 10000$ and 100000, respectively.

Values of c_f and $H \equiv \delta^*/\theta$ obtained from Coles and Kármán-Schoenherr correlations are listed in table 12.1. In addition, values of u^+ versus y^+ for $Re_\theta = 10000$ and 100000 are provided in tables 12.2 and 12.3, respectively.

Table 12.2. u^+ vs. y^+ at Re_θ = 10,000—Coles' velocity law

y^+	1	2	5	10	20	50	100	200	500	1000	2000	3000
u^+	9.999	1.998	4.871	8.336	11.5	14.46	16.24	17.94	20.29	22.36	25.19	27.08

Table 12.3. u^+ vs. y^+ at Re_θ = 100,000—Coles' velocity law

y^+	100	200	500	1000	2000	5000	10000	20000	30000
u^+	16.23	17.92	20.16	21.85	23.56	25.92	28.03	30.93	32.77

Although the computational experiments have suggested that for $Re_\theta < 5000$ the influences of inlet conditions become unimportant, these results have been obtained using an inlet boundary layer with $Re_\theta = 1000$.

b. Results

The results herein show the comparison of the skin friction at $Re_\theta = 10000$. At this Reynolds number, it is found that the solution is not affected by the inlet conditions used (see fig. 12.4 for effects of inlet conditions). In this section, all calculations were performed for the following conditions unless otherwise stated. The ratio of turbulent viscosity to molecular viscosity in the freestream, μ_t/μ_l, and the ratio of the square root of the freestream turbulent kinetic energy to the freestream velocity, $\sqrt{k}/U_\infty$, were both taken to be 0.1% (see more details in paragraph 3 below). The computational box was defined by $Re_L = 2\cdot10^7$ (Re_θ up to $2.5\cdot10^4$) with a height to length ratio of 0.02. The grid points were expanded exponentially from the wall to the top of the domain with an expansion ratio determined by the choice of the value of y^+ at the first grid point. The value of y^+ at the first point was kept approximately 0.1. Grid sensitivity study has shown that at least 60 points should be used inside the boundary layer to obtain grid-independent results. There is virtually no difference in solutions between a boundary layer code and a Navier-Stokes code as will be seen later. Therefore, it is adequate to use a boundary layer code to assess the model performance. However, for those who are interested in validating the model implementations in their own application (Navier-Stokes) codes, at least 100 grids in the streamwise direction with an expanding grid-spacing ratio of 1.05 are recommended to achieve accurate solutions. For use of compressible codes, the freestream Mach number should be kept on the order of 0.1.

1) Grid sensitivity study

The computations were performed with 50, 100, 250, 500, and 1000 grid points in the y direction. This corresponds to approximately 35, 65, 145, 265, and 465 grid points inside the boundary layer at $Re_\theta = 10000$. The results are reported based on the percent errors with respect to the solution obtained using 1000 grid points. Figure 12.1 shows the sensitivity of the model solutions to the number of grid points used in the calculations. As can be expected, the one-equation model is less sensitive to the grid refinement. In general, errors can be controlled within less than 2% if 100 grid points are used in the calculations (corresponding to 60 grid points inside the boundary layer).

2) Sensitivity to the distance of the first point from the wall, y^+_1

The computations were performed with $y^+_1 \approx 0.014$, 0.14, 0.4, 0.7, 1.1, and 1.4 using 500 points in the y-direction. The results are reported based on the percent errors with respect to the solution obtained using $y^+_1 \approx 0.014$. Figure 12.2 shows the sensitivity of the model solutions to the distance of the first point from the wall used in the calculations. The k-ε model is very sensitive to the value of $y^+$of the first grid point while the zero and the one-equation models are the least sensitive ones. In general, one should limit the value of y^+_1 to be less than 0.3 to have accurate solutions.

3) Freestream sensitivity study

The computations were performed by fixing the freestream value $\sqrt{k_\infty}/U_\infty$ at the upstream boundary at 0.1% while varying the value of freestream turbulent viscosity to molecular viscosity ratio according to $\mu_{t\infty}/\mu_{l\infty} = 10^n$. Values of n chosen were –6, –3, –1, and 0. Figure 12.3 shows the sensitivity of the model solutions to the choice of n. It can be seen that the k-ω model is very sensitive to high freestream turbulence as discussed by Menter (ref. 12). In general, one should choose the value of n to be less than –3. This choice is well within the criteria set by Menter to have freestream-independent results.

4) Effects of inlet conditions and code-independence study

Three codes were used in this study: a boundary layer code (ref. 35), an incompressible Navier-Stokes code (INS2D) (ref. 20), and a compressible Navier-Stokes code (ref. 32). The "standard" solutions for each code were established following the guidelines described above. Figure 12.4 shows the comparison of the results obtained by the three codes using the *SST* model. Differences in the region $Re_\theta < 5000$ were mainly due to the different inlet conditions used in the three runs. Differences in skin friction coefficients are less than 1% after $Re_\theta > 5000$. Comparisons based on other models are also available and they all show similar conclusions.

5) Mach number effects

Figure 12.5 shows the comparison of the results obtained with the k-ε model using freestream Mach numbers of $M_\infty = 0.1$ and $M_\infty = 0.5$. The solution obtained from the incompressible boundary layer code is also shown. In this case the effects of inlet conditions were not investigated. It can be seen that the skin friction coefficients for $M_\infty = 0.5$ are slightly lower than those for $M_\infty = 0.1$. At $Re_\theta = 10000$, the difference between the incompressible boundary layer solution and the Navier-Stokes Mach 0.1 solution is about 0.15% while the difference between the incompressible boundary layer solution and the Navier-Stokes Mach 0.5 solution is about 1.7%.

The comparisons of both skin friction c_f and shape factor H are shown in figures 12.6 and 12.7, respectively. In addition, the results in figures 12.8 and 12.9 are reported based on the percent errors, $(c_f - c_f(\text{K-S}))/c_f(\text{K-S}) \times 100$ and $(H - H(\text{Coles}))/H(\text{Coles}) \times 100$. All models predict Coles' correlation for skin friction within ±2% for $Re_\theta > 10^4$ and tend to overpredict the skin friction within 1% to 3% with respect to the von Kármán correlation at high Reynolds numbers, ($Re_\theta = 10^5$). The differences are larger at low Reynolds numbers; the *SST* k-ω and the Spalart-Allmaras models overpredict 4% while the k-ε and k-ω models underpredict 3.5% and 5%, respectively, the skin

friction of the von Kármán correlation at $Re_\theta = 2000$. The *SST k*-ω and the Spalart-Allmaras models tend to agree better than the other models with the values obtained from Coles' correlation, and they agree almost exactly with Coles' shape factor for $Re_\theta > 5000$.

Plots of u^+ against y^+ for $Re_\theta = 10000$ and 100000 are shown in figures 12.10 and 12.11, respectively. The results are also presented in term of percent errors with respect to Coles' profiles, shown in figures 12.12 and 12.13. All models show agreement with the empirical correlation. In addition, the $Re_\theta = 100000$ run provides information on the predicted values for κ and C in the inner layer. Use y^+ between 50 and 3000 ($y/\delta \approx 0.1$) to extract values of κ and C. Table 12.4 shows values of κ and C evaluated from the benchmark model solutions.

Table 12.4. Predictive values of κ and C

Model	κ	C
k-ε 2-eqn	0.4096	5.525
k-ω 2-eqn	0.3831	4.011
SST k-ω 2-eqn	0.3816	3.939
S-A 1-eqn	0.4073	5.060
B-L 0-eqn	0.4101	5.2034

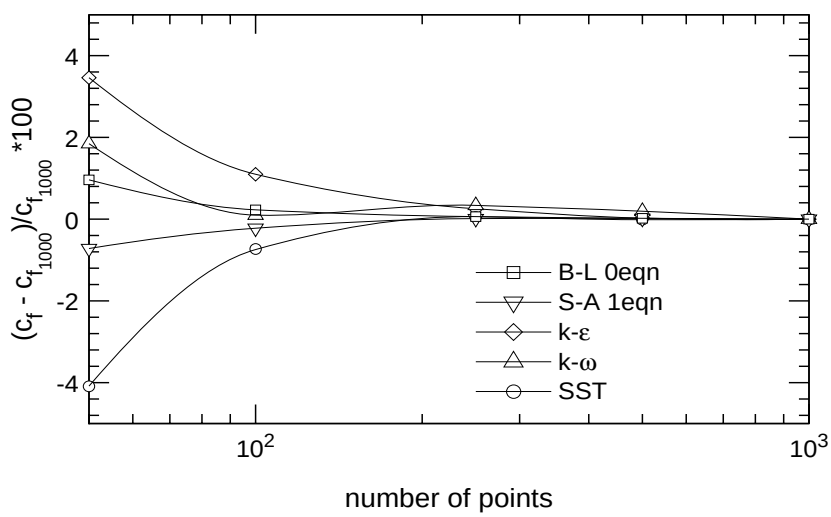

Figure 12.1. Grid sensitivity study—flat plate boundary layer.

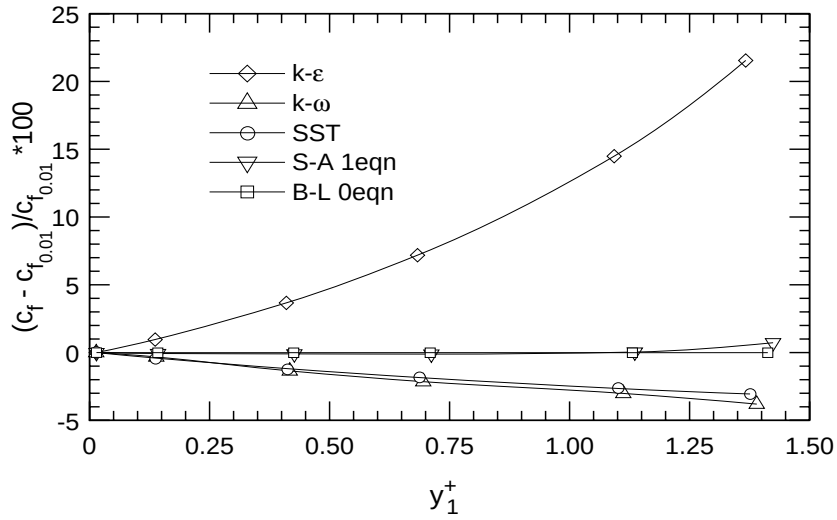

Figure 12.2. Sensitivity to the distance of the first point to the wall.

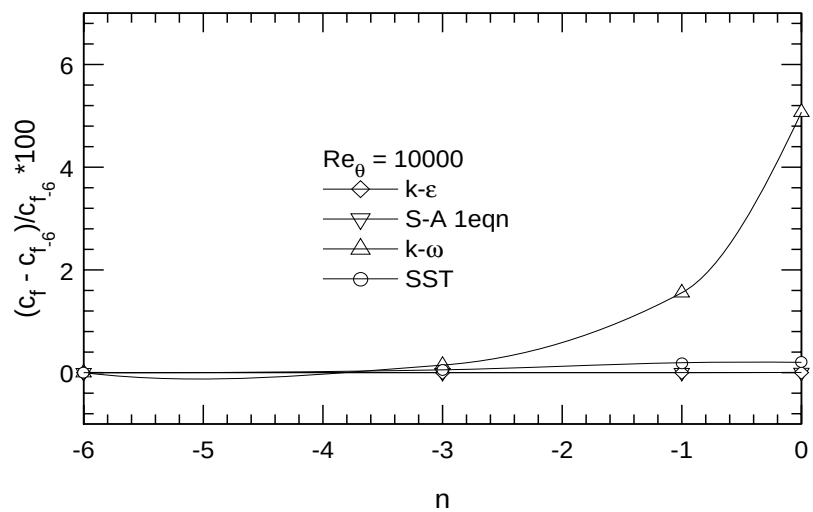

Figure 12.3. Freestream sensitivity study.

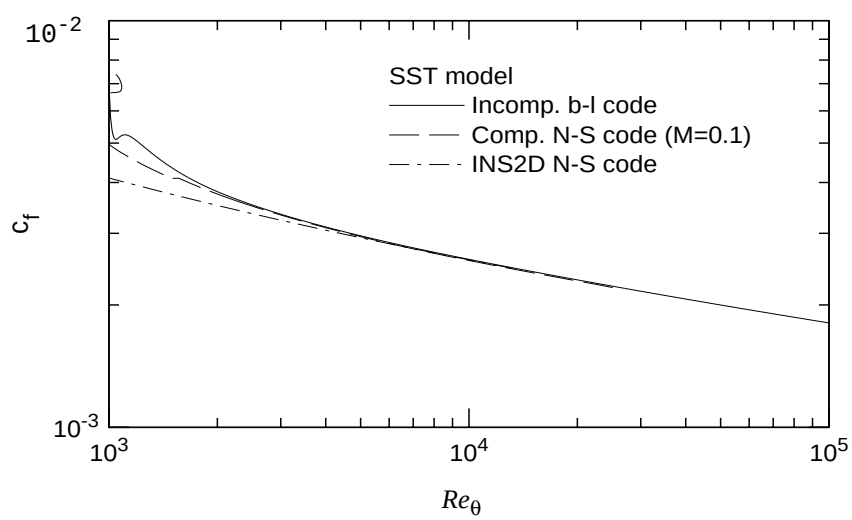

Figure 12.4. Effects of inlet conditions and code-independent study.

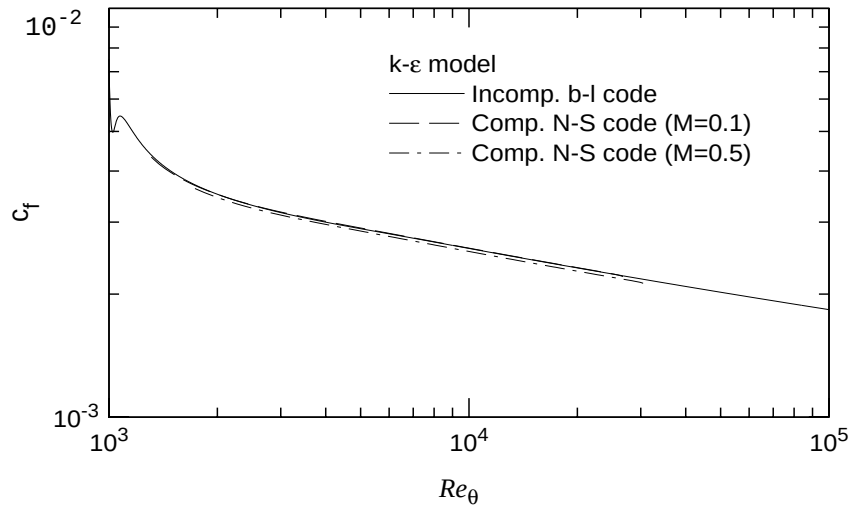

Figure 12.5. Freestream Mach number effects.

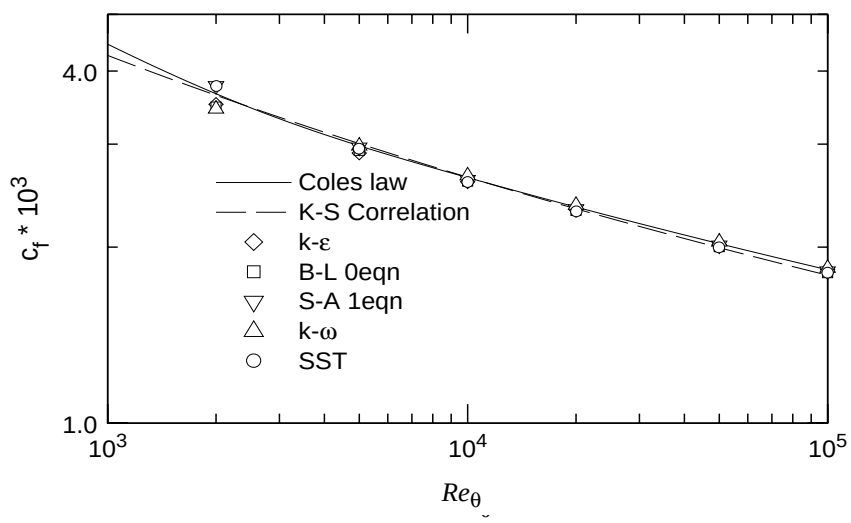

Figure 12.6. Skin friction comparison.

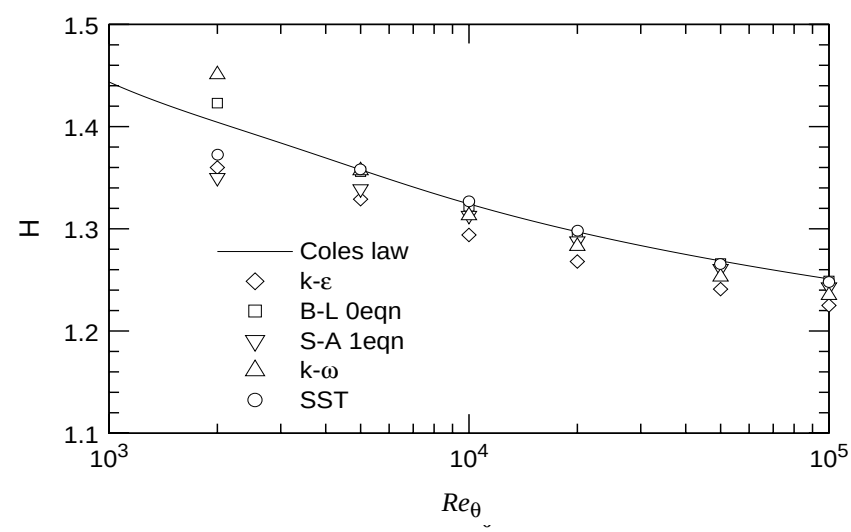

Figure 12.7. Shape factor comparison.

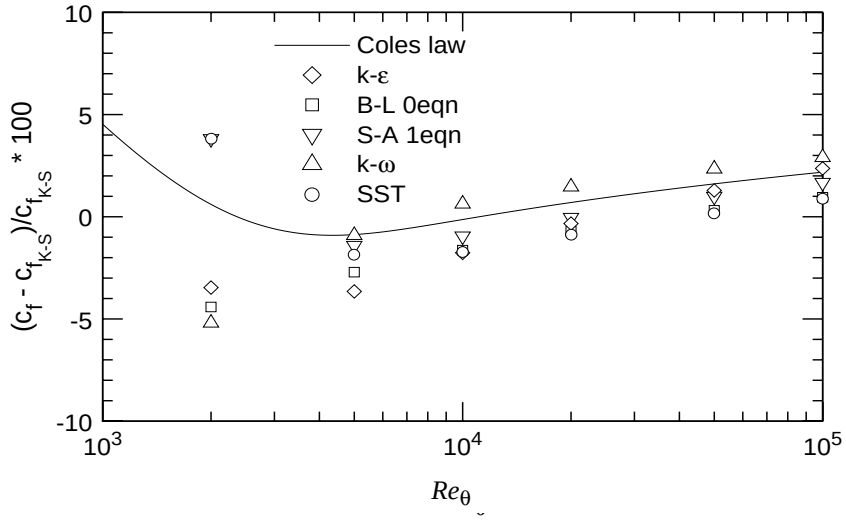

Figure 12.8. Percentage errors of skin friction with respect to the von Kármán-Schoenherr correlation.

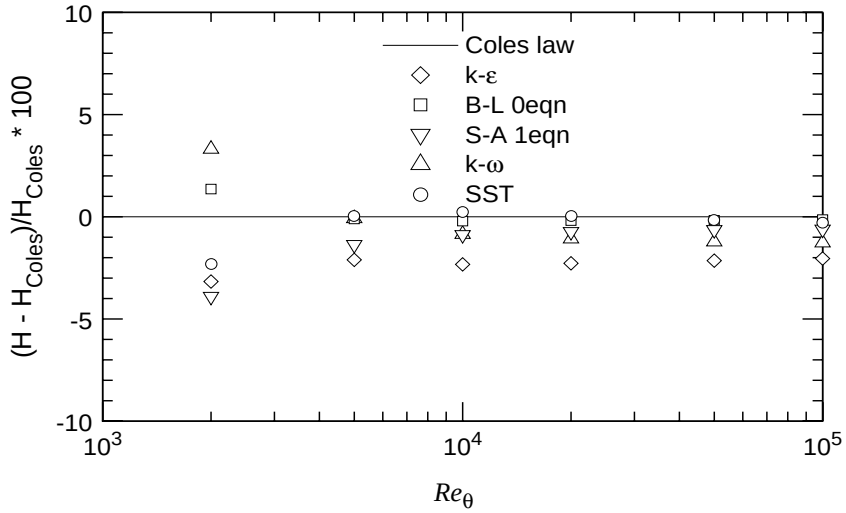

Figure 12.9. Percentage errors of shape factor with respect to Coles' velocity profile.

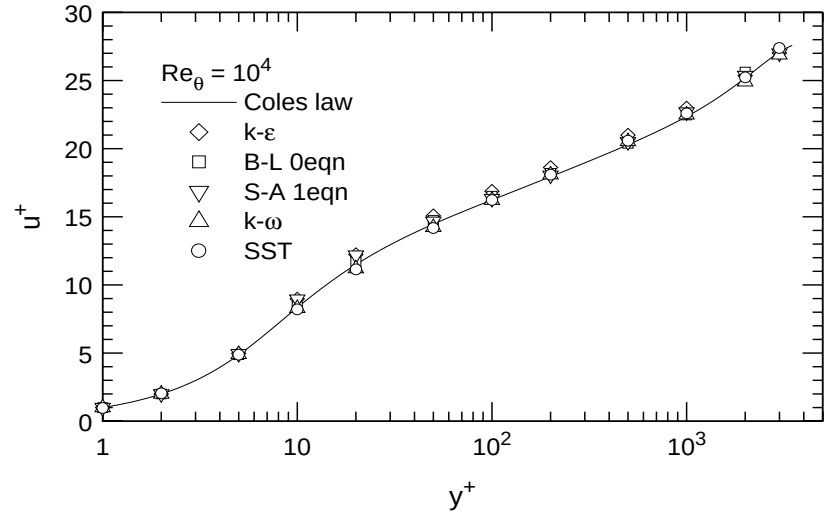

Figure 12.10. Comparison of the velocity profiles—$Re_\theta = 10^4$.

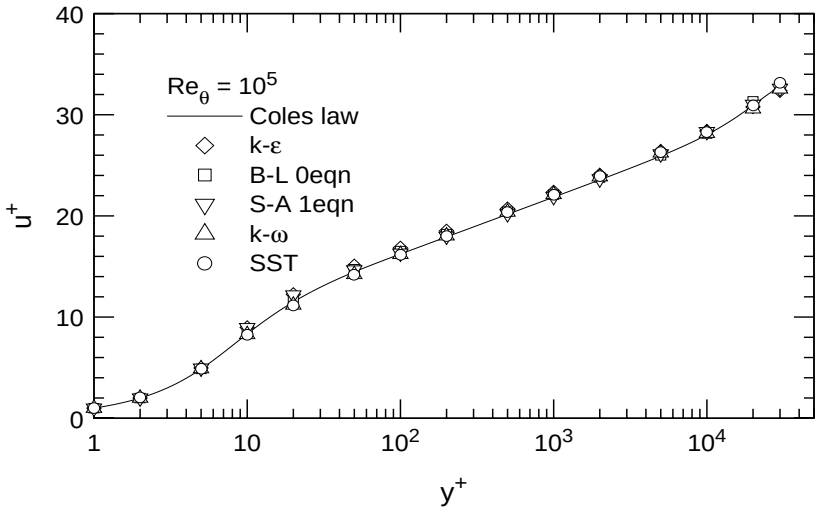

Figure 12.11. Comparison of the velocity profiles—$Re_\theta = 10^5$.

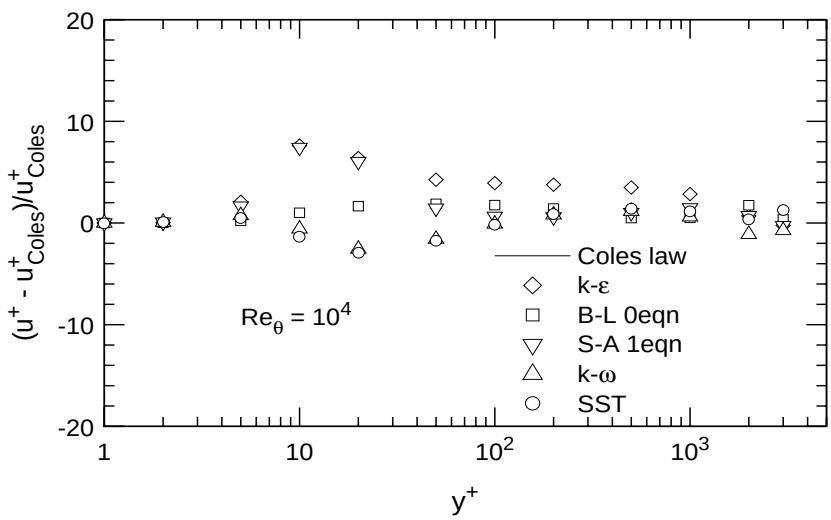

Figure 12.12. Percentage errors with respect to Coles' velocity profile—$Re_\theta = 10^4$.

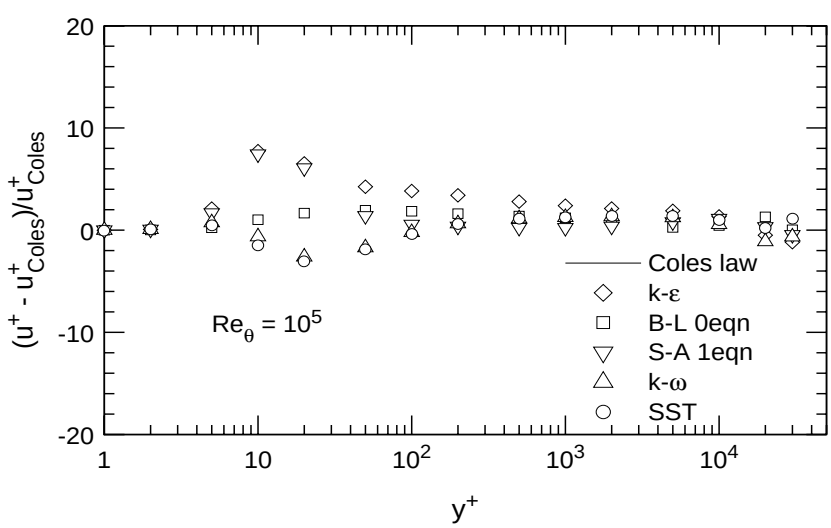

Figure 12.13. Percentage errors with respect to Coles' velocity profile—$Re_\theta = 10^5$.

Section 13. Compressible Flat Plate Flow

a. Empirical correlations of data

The model predictions will be compared with the following empirical correlations of mean velocity profile and skin friction of a Mach 5 boundary layer flow over an adiabatic surface. The general consensus is that the Van Driest I transformation (ref. 36) is a good fit to the experimental data of the velocity profile in the inner layer, and the Van Driest II transformation (ref. 37) offers a good fit to the experimental data of skin friction.

The Van Driest I velocity transformation is

$$U_c^+ = \frac{1}{\kappa} \ln y^+ + C \tag{13.1}$$

where

$$U_c^+ = U_c / U_t \qquad y^+ = \rho_w U_t y / \mu_w \qquad \kappa = 0.41 \qquad C = 5$$

$$U_c = \sqrt{B}\left[\operatorname{asin}\left(\frac{A+U}{D}\right) - \operatorname{asin}\left(\frac{A}{D}\right)\right] \qquad U_t = \sqrt{\tau_w / \rho_w}$$

$$A = q_w / \tau_w \qquad B = (2 c_p T_w) / Pr_t \qquad D = \sqrt{A^2 + B} \tag{13.2}$$

The general formula for Van Driest II skin friction transformation is

$$c_f F_c = f\,(F_{Re_\theta} Re_\theta) \tag{13.3}$$

where

$$F_c = \frac{T_{aw}/T_\infty - 1}{(\operatorname{asin}\alpha + \operatorname{asin}\beta)^2} \qquad \text{and} \qquad F_{Re_\theta} = \frac{\mu_\infty}{\mu_w}$$

$$\alpha = \frac{(T_{aw}/T_\infty) + (T_w/T_\infty) - 2}{\sqrt{[(T_{aw}/T_\infty) - (T_w/T_\infty)]^2 + 4\,(T_w/T_\infty)\,[(T_{aw}/T_\infty) - 1]}} \tag{13.4}$$

$$\beta = \frac{(T_{aw}/T_\infty) - (T_w/T_\infty)}{\sqrt{[(T_{aw}/T_\infty) - (T_w/T_\infty)]^2 + 4\,(T_w/T_\infty)\,[(T_{aw}/T_\infty) - 1]}}$$

$$T_{aw} = T_\infty\left[1 + 0.89\left(\frac{\gamma - 1}{2}\right)M^2\right]$$

For a flow with freestream temperature of 300 K, table 13.1 gives the skin friction values at selected Reynolds numbers:

Table 13.1. Skin friction coefficients

Re_θ	5000	10000	20000	50000	100000
c_f	0.001077	0.0009285	0.0008087	0.0006830	0.0006065

The velocity profile family of Huang, Bradshaw, and Coakley (ref. 38) is an extension of the Van Driest I transformation applied to Coles' profile that includes the sublayer and the wake regions. This profile family is a good fit to boundary layer velocity profiles for a wide range of Mach and Reynolds numbers. It is also displayed in this comparison but should not be treated as an exact solution of the compressible boundary layer flow.

b. Results

Figure 13.1 shows the comparison of the skin friction versus Reynolds number for the Re_θ values listed in table 13.1. The calculations were performed with y^+ at the first grid point at approximately 0.1 and 120 points inside the boundary layer. The freestream temperature was set at T_∞ = 300 K. All models seem to follow the empirical trend well. The k-ε model, however, shows a significant underprediction of skin friction coefficient. This is due to the fact that the model is very sensitive to low Reynolds number effects and tends to overpredict compressible log law as shown in figure13.2, where comparisons of the mean velocity and temperature profiles are shown. As can be seen from the comparison of the dimensionless transformed velocity profiles, the k-ε model tends to predict a large slope in the inner layer while all the other models seem to follow the law of the wall for compressible flow reasonably well. The *S-A* model appears to give the best overall predictions of c_f and u^+.

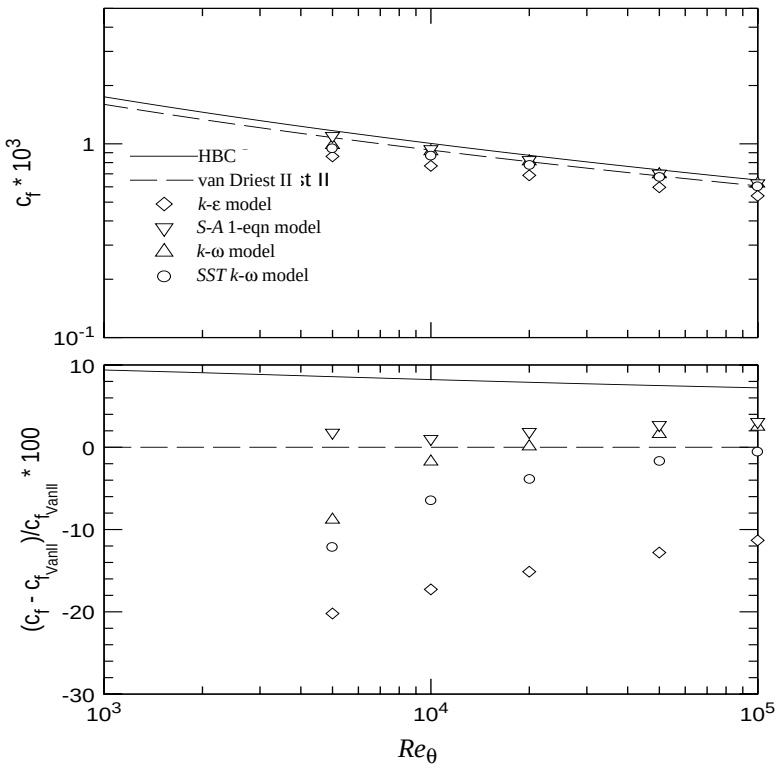

Figure 13.1. Comparison of the skin friction coefficients.

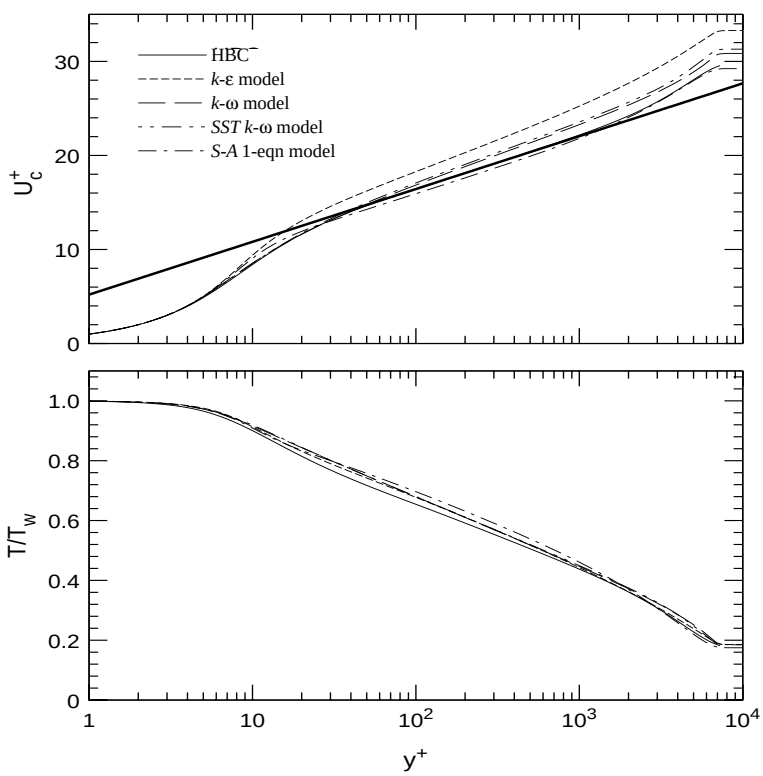

Figure 13.2. Comparison of velocity and temperature profiles.

Section 14. Axisymmetric Boundary Layer with Adverse Pressure Gradient

a. Experimental data and description of numerical procedure

The experiment performed by Driver (ref. 39) consists of an axial flow along a cylinder with superimposed adverse pressure gradient. Boundary layer suction was applied through slots on the wind tunnel walls, and this mass flow removal (about 10% of the incoming mass flow trough the tunnel) allowed the flow to remain attached along the tunnel walls in the presence of the strong pressure gradient. Experimental data, including velocity and Reynolds stress profiles, have been measured in several locations. Since flow separation was observed experimentally, a full Navier-Stokes prediction method was performed and is recommended. The solution procedure requires the specification of an outer boundary such as a streamline. The experimental velocity profiles have been integrated to obtain the stream function and corresponding outer streamline. From a computational point of view, this method allows the flow to be treated as flow in an annular duct with one boundary defined with the surface of the cylinder (no-slip condition) and other boundary defined with an outer streamline (slip condition). The recommended outer streamline distance $h(mm)$ as a function of the coordinate distance $x(mm)$ is

$$x(mm) = [-457.2,\ -330.2,\ -228.6,\ -152.4,\ -76.2,\ -12.70,\ 50.8,\ 101.6,\ 152.4,\ 228.6,\ 304.8,\ 400.0,\ 500.0,\ 600.0,\ 700.0,\ 800.\ 0]$$

$$h(mm) = [\ 37.08,\ 37.10,\ 38.51,\ 42.66,\ 48.53,\ 55.44,\ 61.88,\ 65.08,\ 67.89,\ 70.40,\ 71.20,\ 69.0,\ 63.04,\ 56.04,\ 48.04,\ 42.08]$$

in which the outer streamline profile between $x = -457.2\ mm$ and $x = 304.8\ mm$ is estimated from measured experimental velocity profiles, and for $x \geq 400\ mm$ it is estimated by matching the measured pressure coefficients, c_p, along the cylindrical surface. It should be noted that since the flow reattached around $x \approx 250\ mm$, the exact shape of the streamline after $x = 304.8\ mm$ does not affect the flow field in the region of current interest—a fact that will be demonstrated later.

The inlet profile is a good match to an equilibrium boundary layer with $Re_\theta = 2760$ and can be obtained by matching the momentum thickness from a calculation of a spatially evolving boundary layer (using the same Navier-Stokes code or a boundary layer code).

The following solutions are obtained from a mesh with 201×81 grid points in the x and y directions, respectively. The grid is uniform in the streamwise direction and exponentially expanded in the radial direction with the first y^+ less than 1/10.

b. Results

Figure 14.1 shows comparisons of the pressure and skin friction coefficients based on the same outer boundary. With the exception of the k-ε model, all models predict flow separation. Overall, the *SST* model gives the best performance.

Comparisons of the velocity, turbulent kinetic energy, and shear stresses at some specific measured locations are displayed in figures 14.2, 14.3, and 14.4, respectively. Again, the figures show that

the *SST* model gives the best overall performance, the k-ε model the worst, and the other two models are in between.

There are a few uncertainties associated with this test case—grid resolution, effects of inlet conditions, and effects of outflow boundary conditions. Figure 14.5 shows the comparison of pressure and skin friction coefficients using four different grids—201×81, 101×81, 301×161, and 89×89—all being uniform in the streamwise direction. The results for the last grid system (89×89) were obtained using INS2D code (ref. 20). For purposes of illustration, only results for the *SST* model are presented. As can be seen from the figure, the results obtained using 301×161 and 201×81 were almost identical. Results obtained using 101×81 show a slight undershoot of pressure coefficient for x/R_0 approximately between –1 and 1. This is because in this region there is a rapid expansion of streamlines (see the plot of the outer boundary in the first subset in fig. 14.7), and hence a uniform grid arrangement for such a small grid system may not be sufficient.

As mentioned earlier, the inlet conditions were obtained by matching experimental Re_θ of a Navier-Stokes flat-plate boundary layer calculation. All models show a good match of velocity, turbulent kinetic energy, and shear stress profiles at the first measured location, as shown in the first subset of figures 14.2, 14.3, and 14.4, respectively. There is some uncertainty associated with the measurements in the inlet. In figure 14.6, effects of inlet conditions were studied—in this case, results were compared with those obtained by matching an Re_θ value being 10% less than the experimentally suggested value. As can be seen from the figure, the effects seem smaller than differences between model predictions.

The last location for measuring profiles was at $x/R_0 \approx 4.4$ and $R_0 = 6.927$ *mm*. From the inlet up to this position, the outer streamline was estimated by allowing the mass flow rate (or θ^*) between the outer boundary and the wall to satisfy a prescribed given value. There were no profile measurements after $x/R_0 \approx 4.4$, and therefore the outer boundary was estimated by matching the predicted surface pressure coefficients against the measured ones (fortunately, the differences between model predictions seem small in this region). To ensure that the exact position of the outer boundary after $x/R_0 \approx 4.4$ has little effect in the region of interest, the current results were compared with ones obtained by using an outer boundary of fixed height after $x/R_0 \approx 4.4$. As can be seen from figure 14.7, the results indeed show very little effect.

Finally, a test was conducted to show effects of freestream boundary conditions for the k-ω model. Figure 14.8 shows the comparison of two calculations using the k-ω model—one with $\mu_t/\mu_l = 1$ and the other $\mu_t/\mu_l = 0.001$ at the inlet boundary with $\sqrt{(k/U_\infty)} = 0.1\%$. As can be seen from the results, as expected, effects of freestream conditions do have some important impact on the predictive behavior of the k-ω model for this flow as well. As can be seen from the comparison, the skin friction predicted with $\mu_t/\mu = 1$ is slightly larger than that predicted with $\mu_t/\mu = 0.001$ everywhere, and the pressure coefficient is also overpredicted for the region of x/R_0 between 0 and 5.

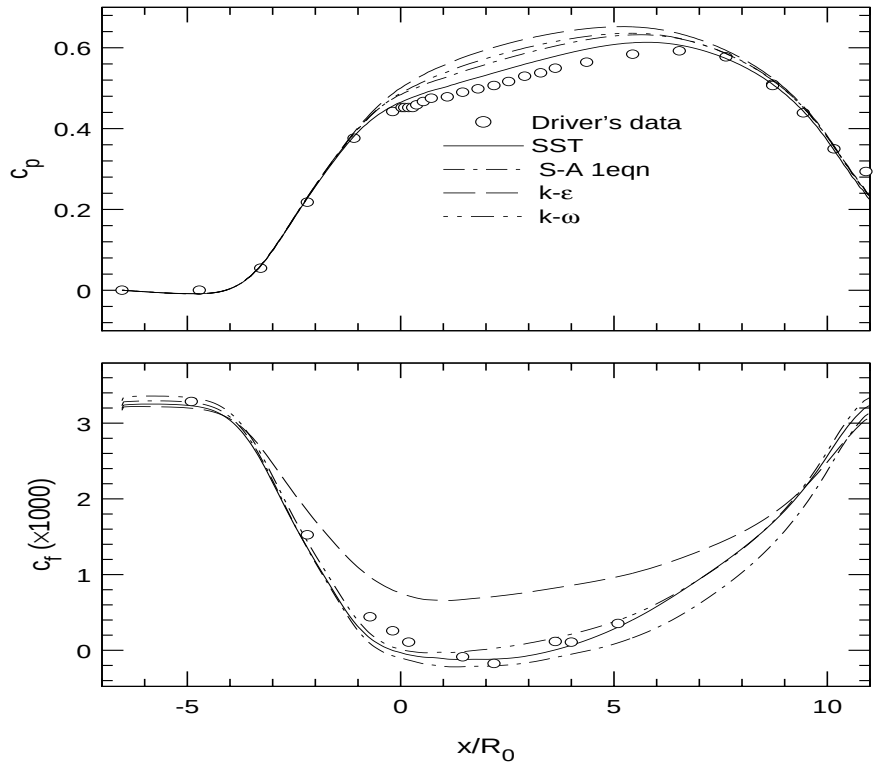

Figure 14.1. Comparison of surface pressure and skin friction coefficients.

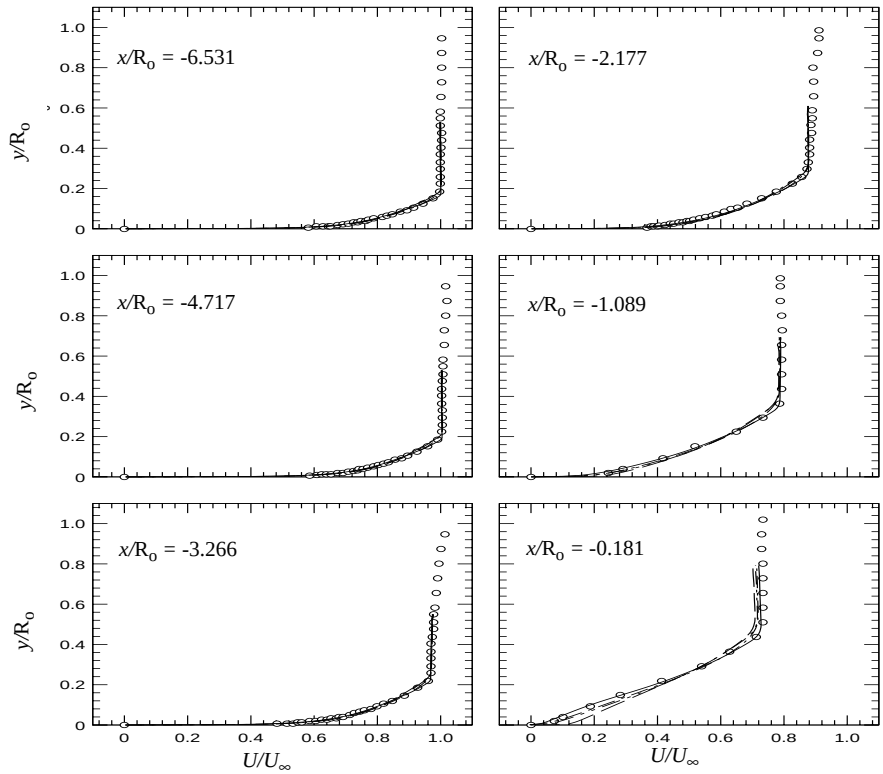

Figure 14.2a. Comparison of velocity profiles. See symbol notations in figure 14.1.

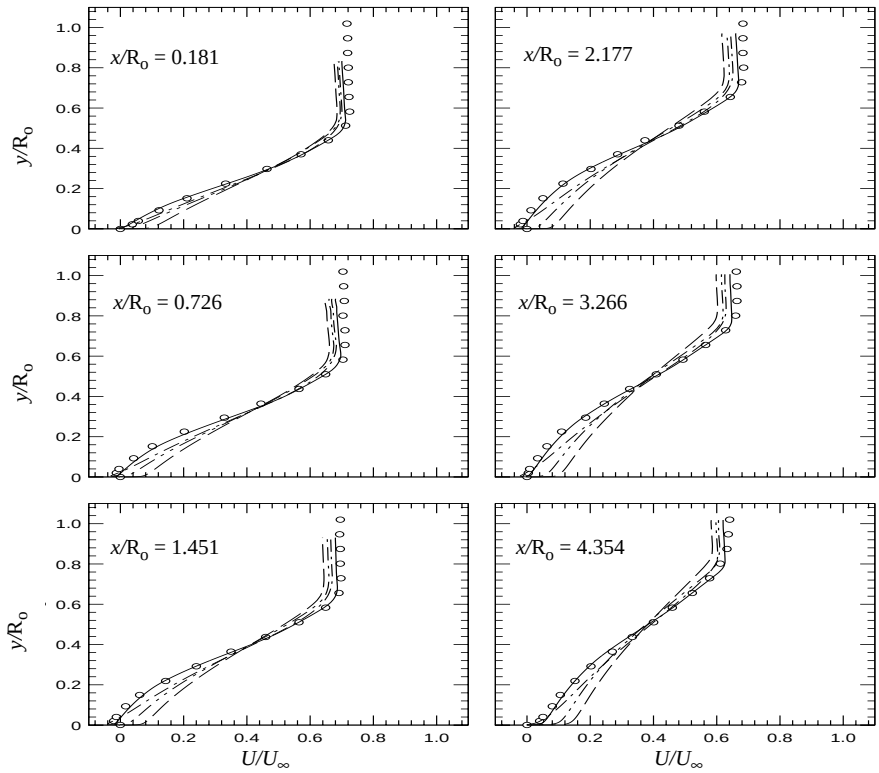

Figure 14.2b. Comparison of velocity profiles. See symbol notations in figure 14.1.

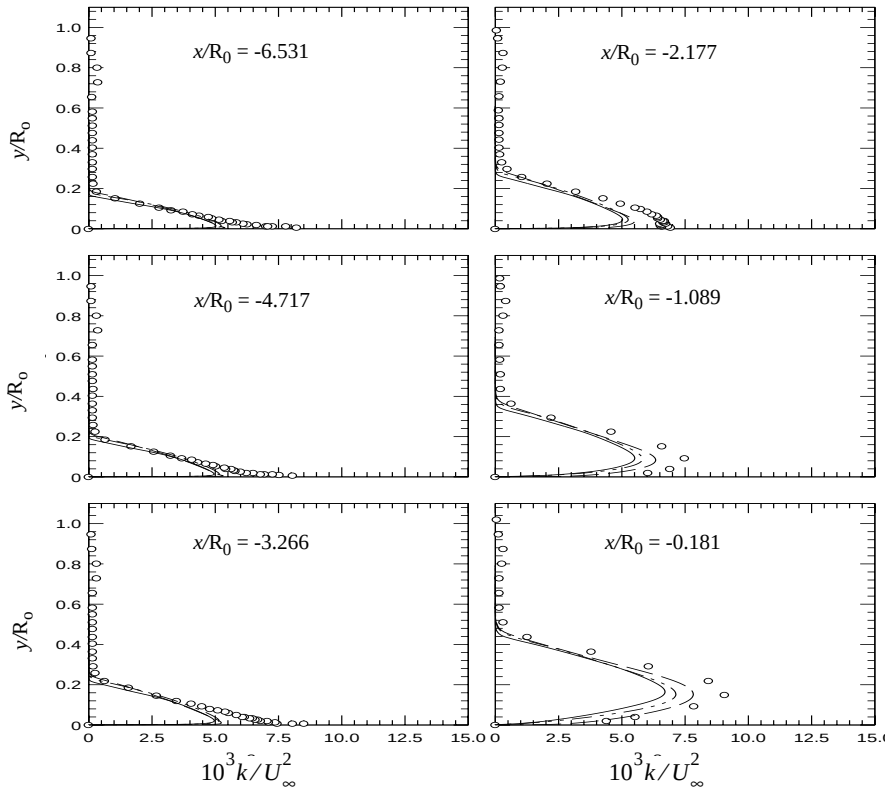

Figure 14.3a. Comparison of the turbulent-kinetic energy profiles. See symbols in figure 14.1.

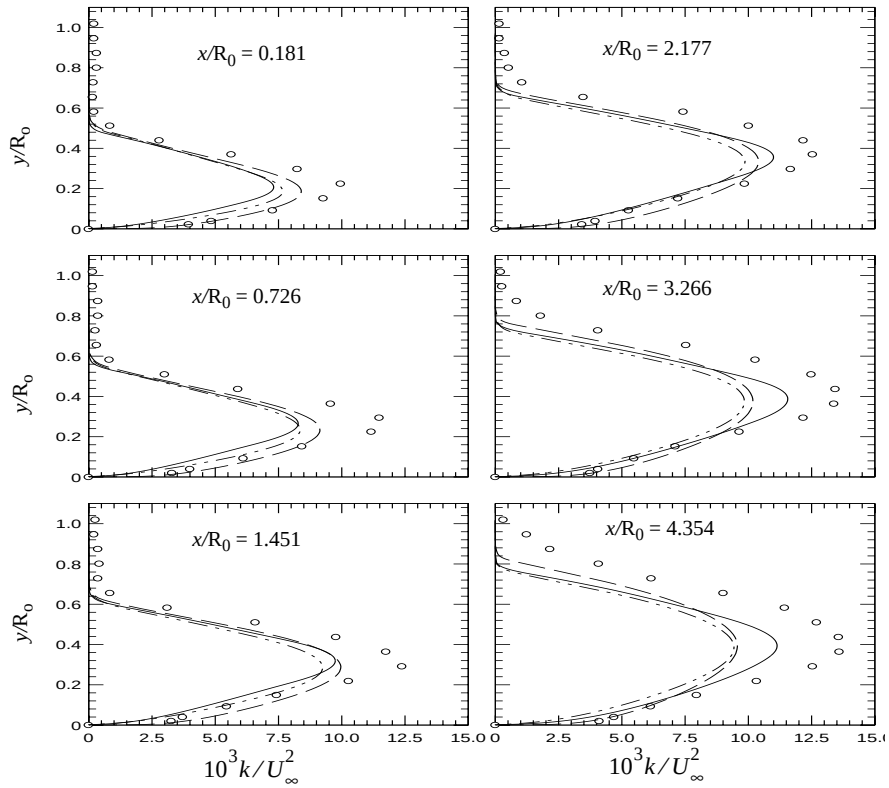

Figure 14.3b. Comparison of the turbulent-kinetic energy profiles.

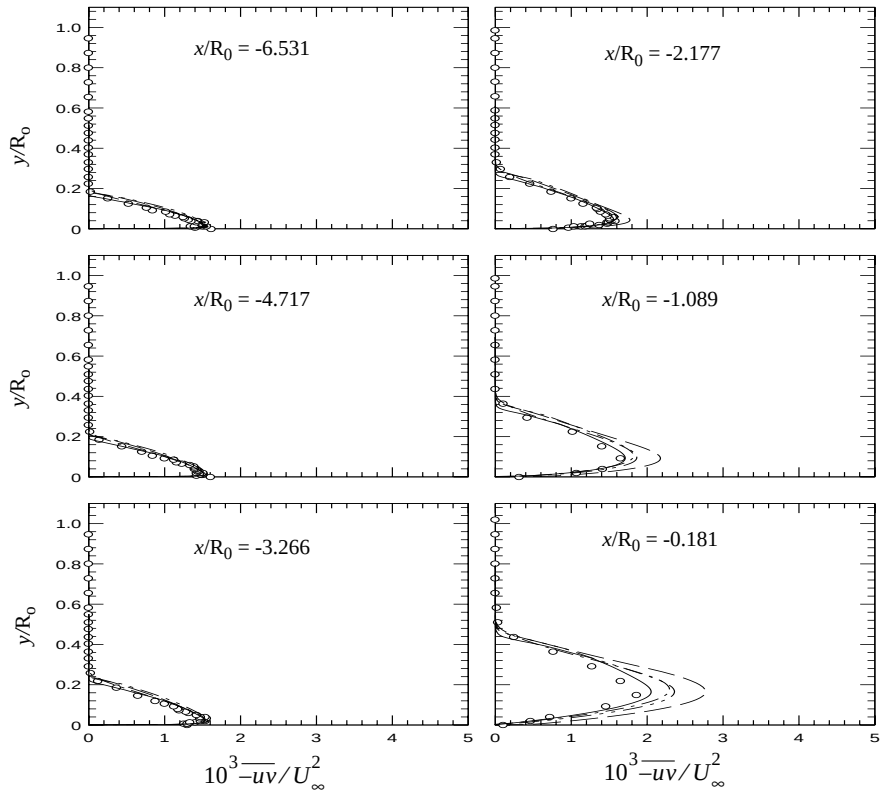

Figure 14.4a. Comparison of the shear-stress profiles. See symbols in figure 14.1.

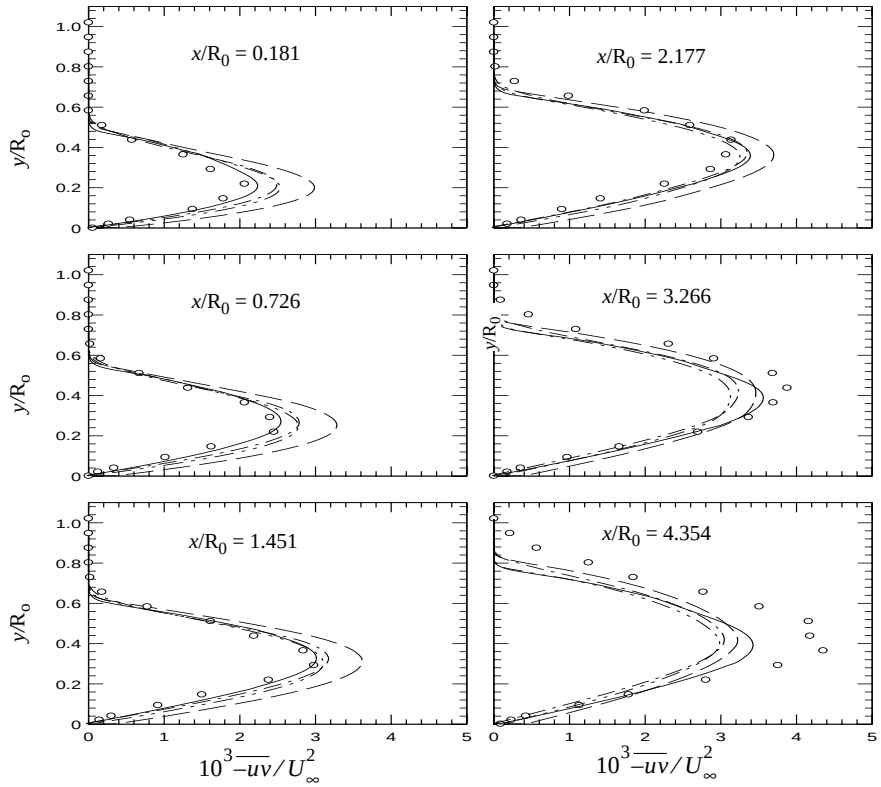

Figure 14.4b. Comparison of the shear-stress profiles.

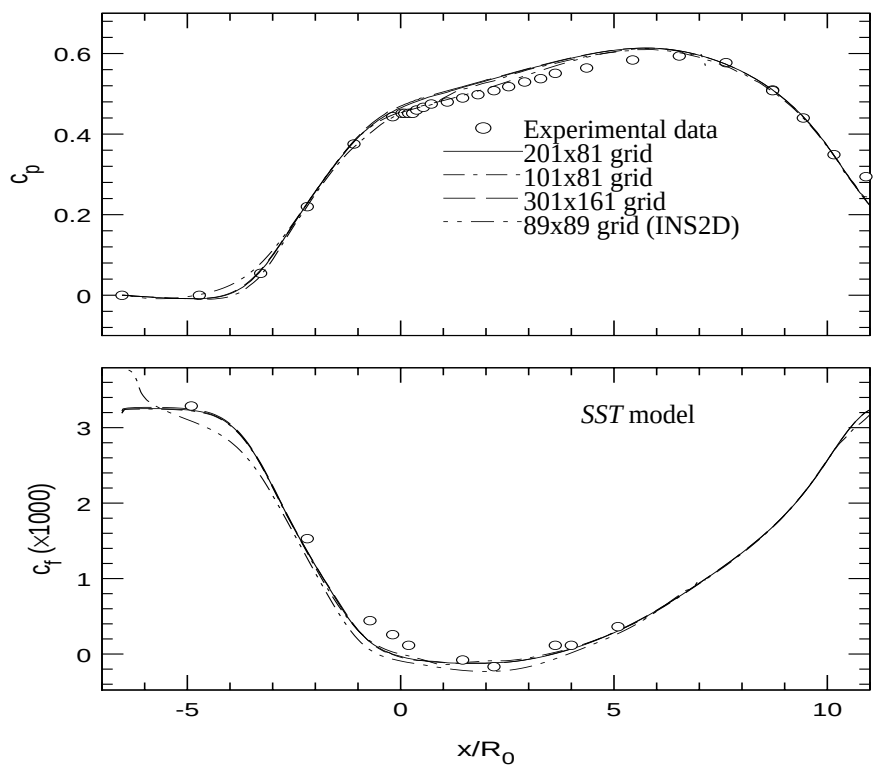

Figure 14.5. Grid sensitivity study.

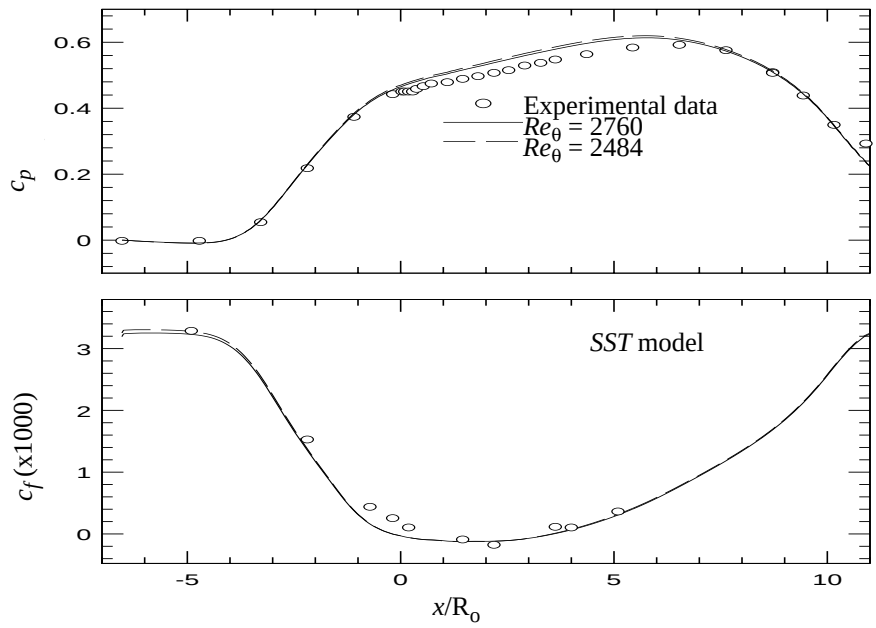

Figure 14.6. Effects of inlet boundary layer profiles.

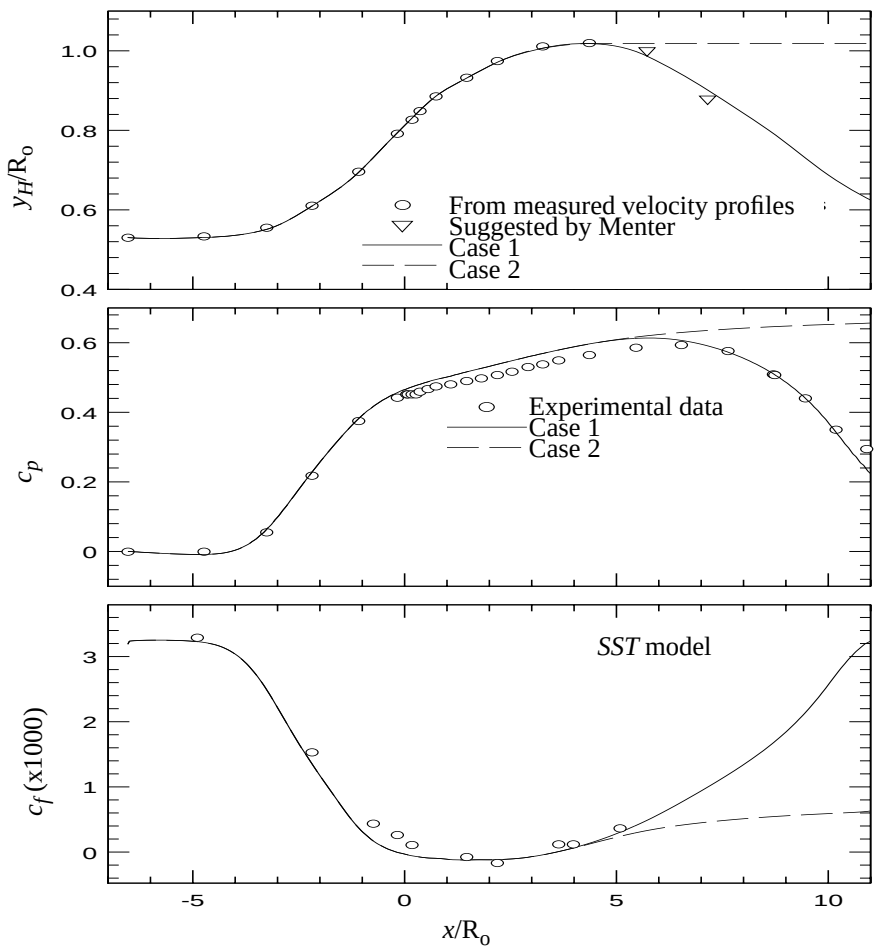

Figure 14.7. Effects of position of the outer streamline in the outflow region.

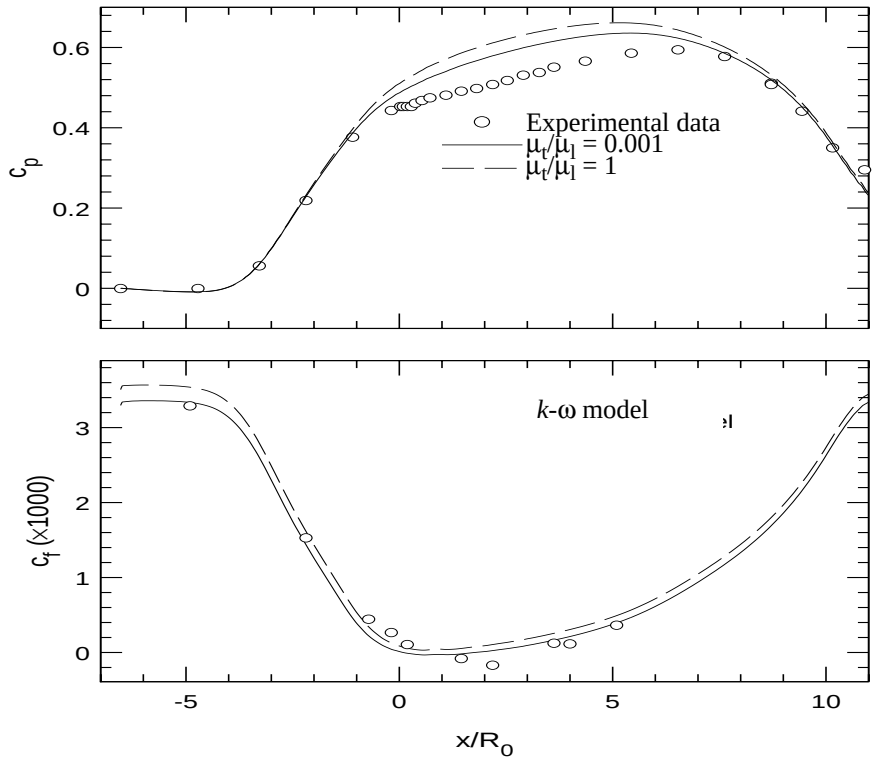

Figure 14.8. Effects of freestream boundary conditions on the *k*-ω model.

Section 15. Transonic Separation Flow over an Axisymmetric "Bump"

a. Experimental data

The experiment (ref. 40) was conducted in the Ames 2- by 2-Foot Transonic Wind Tunnel with total temperature and total pressure of 302 K and $9.5 \cdot 10^4$ N/m^2, respectively. The axisymmetric flow model of this investigation consisted of an annular bump on a circular cylinder aligned with the flow direction. The longitudinal section of the bump was a circular arc. The axisymmetric configuration was chosen to circumvent the problem of sidewall boundary layer contamination of two-dimensionality that can occur in full-span two-dimensional tests. The thin-walled cylinder was 0.0762 m in outside radius and extended 61 cm upstream of the bump leading edge. The straight section of the cylinder permitted natural transition and a turbulent boundary layer just ahead of the bump of sufficient thickness to allow accurate determination of boundary layer information. However, the boundary layer was not so thick, in comparison with the interaction on airfoils, that separation of greater severity would occur than is representative of full scale. The circular-arc bump had a 20.32 cm chord and a thickness of 1.905 cm. Its leading edge was joined to the cylinder by a smooth circular arc that was tangent to the cylinder and the bump at its two end points. Test conditions were a freestream Mach number of 0.875 and unit Reynolds number of $13.1 \cdot 10^6$/m. At this freestream Mach number, a shock wave was generated of sufficient strength to produce a relatively large region of separated flow. The separation and reattachment points were at approximately 0.7 and 1.1 chords, respectively. Boundary layer measurements were obtained by the laser velocimeter technique from upstream of separation through reattachment. These data consist of profiles of mean velocities, turbulence intensities, and shear stresses in the streamwise and normal direction. Separation and reattachment locations were determined from oil-flow visualizations, and local surface static pressures were obtained with conventional pressure instrumentation.

b. Results

Figure 15.1 shows the comparison of the pressure coefficients along the surface of the axisymmetric "bump." Both k-ε and k-ω models predict a delay of the shock position and therefore underpredict the size of the flow separation. The *SST* model provides the best overall performance and the *S-A* one-equation model comes second.

Comparisons of the velocity, shear stress, and turbulent kinetic energy profiles at specific measured positions are shown in figures 15.2, 15.3, and 15.4, respectively. Since experimental data provide only two components of normal stresses, the turbulent kinetic energies shown in figure 15.4 were obtained by setting $w'^2 = (u'^2 + v'^2)/2$. The *SST* k-ω model gives the best agreement of the mean velocity profile with experiment, and closer agreement of mean shear-stress profiles.

Figure 15.5 shows the grid-independent comparison for the *SST* model. The solid line represents results obtained using 181×108 grid points. The grid distribution in the streamwise direction is nonuniform by allowing denser grids near regions of high pressure gradients. The distribution of grid points in the cross-stream direction is expanded exponentially with y^+ values at the points adjacent to the wall being less than 0.1. The dashed line represents results obtained using 382×201 grid points. The grid points in the streamwise direction were increased by placing one additional grid point between two points of the original grid system (181×108). As can be seen from the comparison, the

solution is almost unchanged. It should, however, be noted that Menter, who used CFL3D (ref. 21) and a grid system similar to the current one (181 × 101), obtained a slightly different solution. This is the only case out of all the cases studied so far in which differences between the two codes were found.

Although the calculations were performed from the leading edge of the experimental rig ($x/c \approx -3.2$), it appears that the profiles in the regions just before the flow reaches the bump ($x/c \approx -0.25$) fit the data reasonably well, as can be seen from the first subset of figure 15.2. The calculations were obtained by assuming that the inlet boundary layer profile at the leading edge has a momentum thickness of 200, but it has been found that this profile assumption at the leading edge does not have much impact on the solutions. Figure 15.6 shows the comparison of pressure coefficients for the results obtained by using two different inlet boundary layer profiles, one with $Re_\theta = 200$ and the other $Re_\theta = 1000$. It can be seen that although there is slight change of the velocity profile before the bump the comparison of the pressure coefficients is almost unchanged.

Finally, effects of the freestream conditions of the k-ω model are presented in figure 15.7. As can be seen in the figure, by decreasing the value of the freestream ω 1000-fold, the results are almost unaffected; both predict a delay of the shock position and underpredict the size of the flow separation.

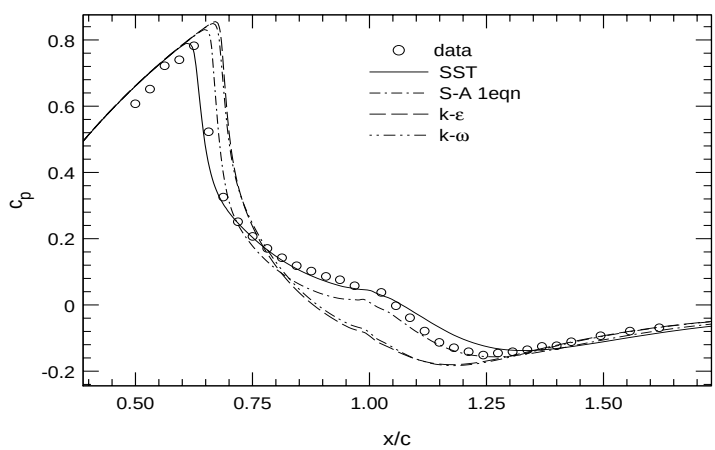

Figure 15.1. Comparison of surface pressure coefficient—transonic bump flow.

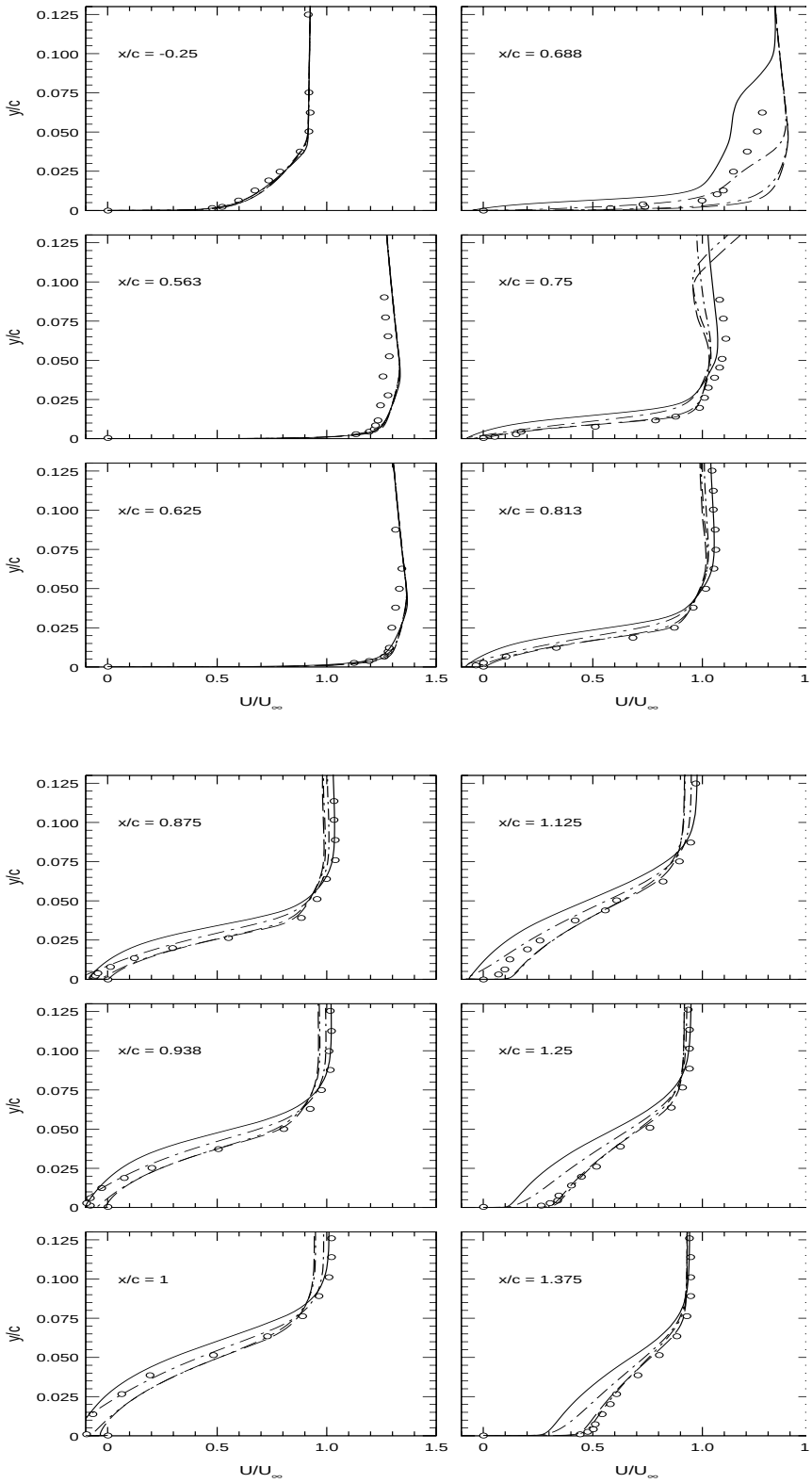

Figure 15.2. Comparison of mean velocity profiles. See symbols in figure 15.1.

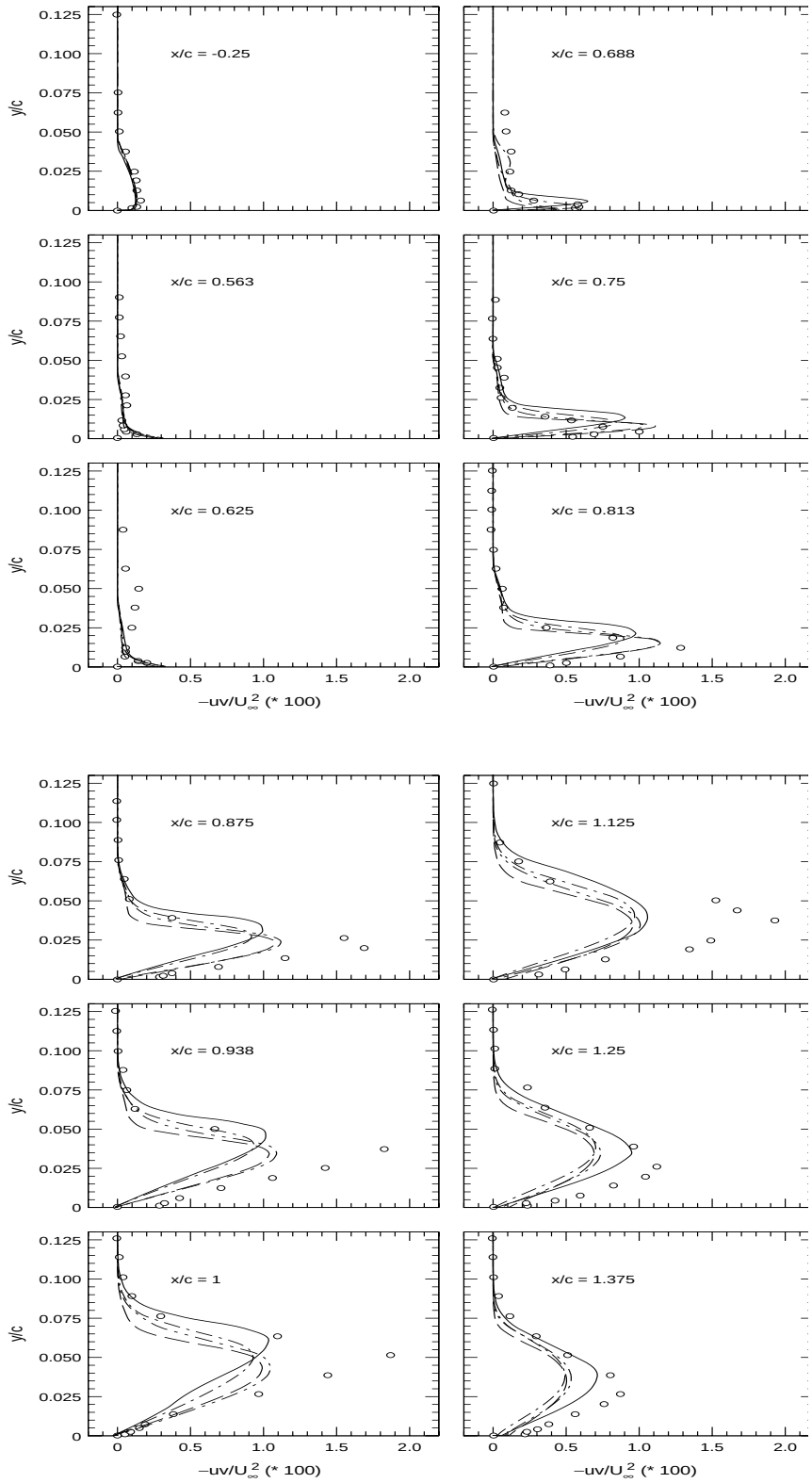

Figure 15.3. Comparison of mean shear-stress profiles. See symbols in figure 15.1.

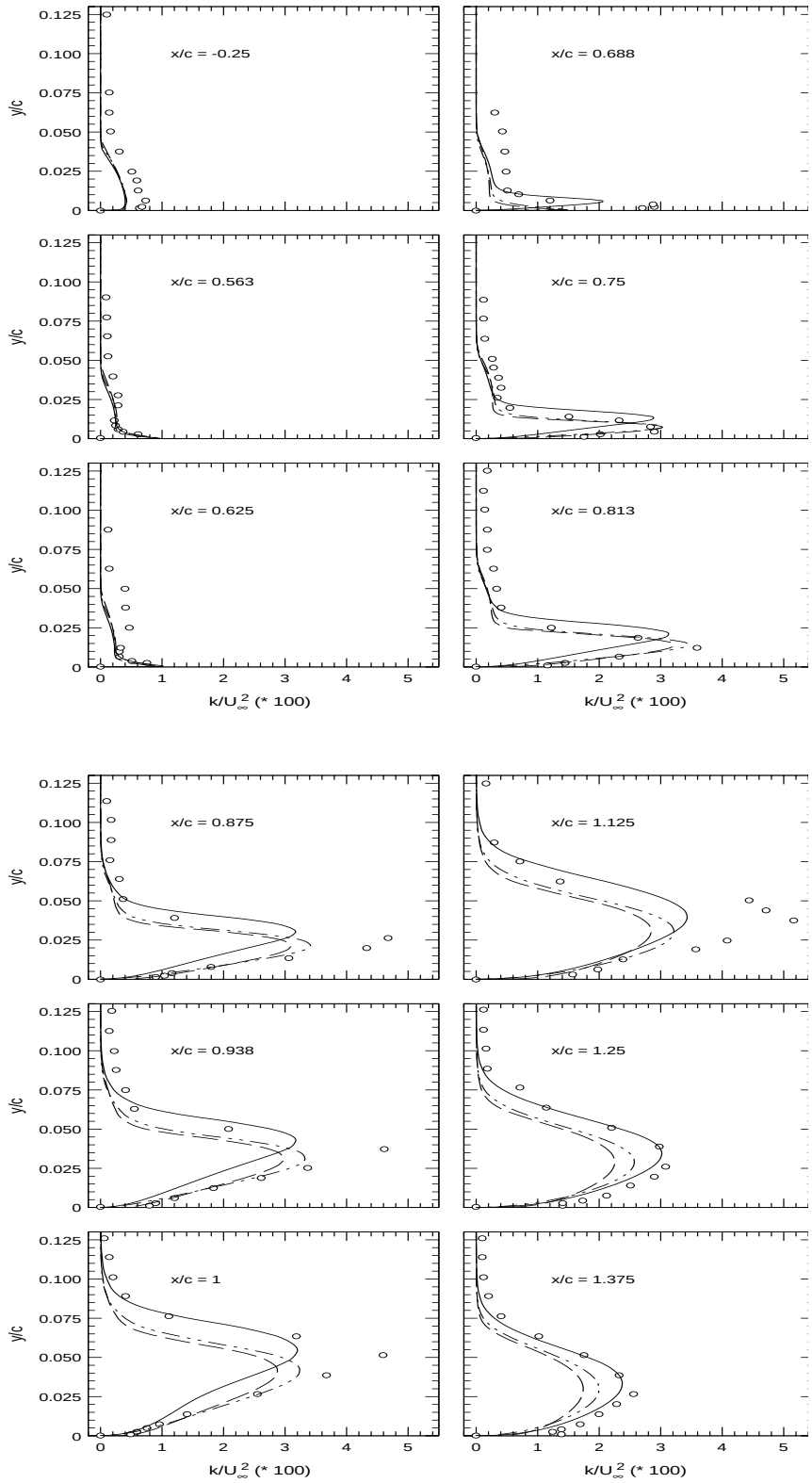

Figure 15.4. Comparison of the turbulent kinetic-energy profiles. See symbols in figure 15.1.

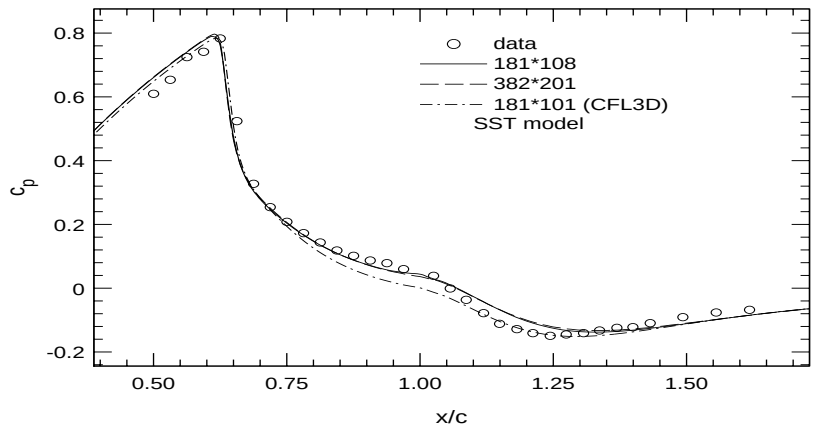

Figure 15.5. Grid refinement study.

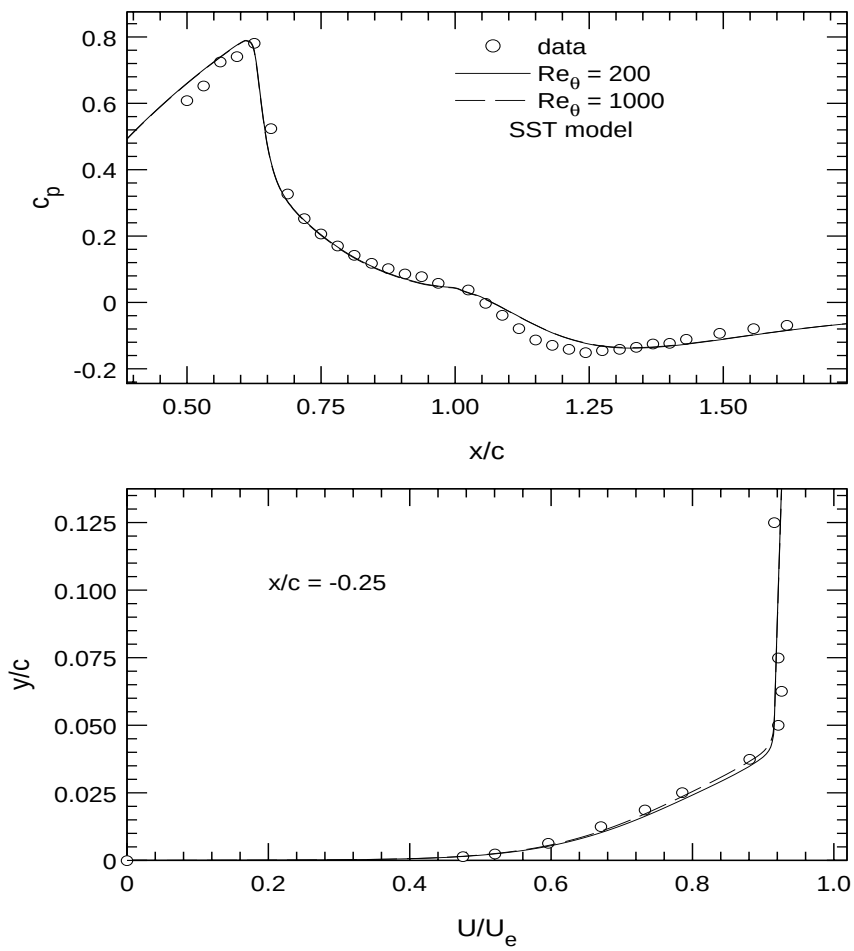

Figure 15.6. Effects of inlet boundary layer profiles.

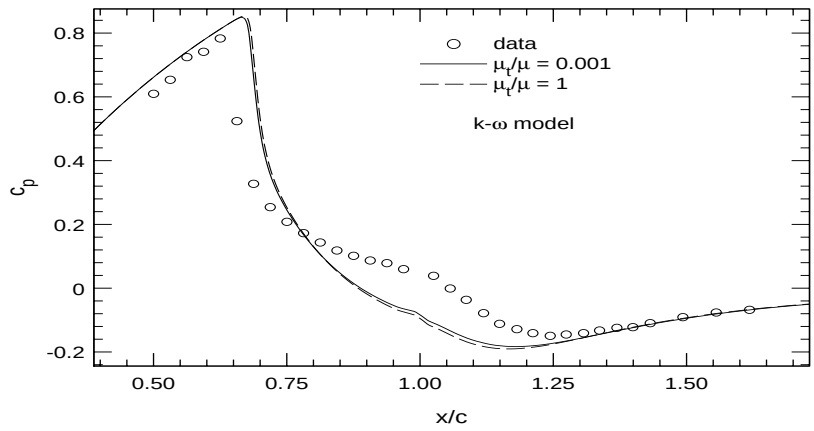

Figure 15.7. Effects of freestream conditions for the *k*-ω model.

Section 16. Transonic airfoil: RAE 2822

a. Experimental data

This data set contains selected results for the RAE 2822 airfoil from the boundary layer, wake, and flow field measurements made in the RAE 2.438 × 1.829 m tunnel at Farnborough, United Kingdom (ref. 41). The detailed description of this test problem can be obtained from FILE 1120 of the 1980–81 AFOSR-HTTM-Stanford Conference on Complex Turbulent Flows (ref. 17). Flow conditions for Case 10 are $M = 0.75$ and $Re = 6.2 \cdot 10^6$. The recommended angle of attack was 2.79° (the sensitivity of the solution to the assumed angle of attack will be presented in a later discussion). The data measured included surface pressure coefficients on both upper and lower surfaces, skin friction coefficients, boundary layer profiles on the upper surface at selected locations ($x/c = 0.152$, 0.179, 0.319, 0.404, 0.498, 0.574, 0.650, 0.75, and 0.9), and three velocity profiles in the wake region ($x/c = 1$, 1.025, and 2). It should be noted that the skin friction coefficient is defined by the local boundary layer freestream conditions, not by the incoming flow conditions.

b. Results

The calculations were performed using a 386 × 82 grid provided by L. Wigton of the Boeing Company. Far field boundary conditions on the velocity field took into account the effect of airfoil circulation due to lift. The grid is shown in figure 16.1. The comparison of the pressure and skin friction coefficients is given in figure 16.2. As can be seen from figure 16.2, the *SST* model shows very good agreement with the experimental data; both the k-ε and k-ω models exhibit a shift of shock position in the downstream direction, and the *S-A* model result is in between. It should be noted that the k-ε model fails to predict flow separation. The comparison of the velocity profiles at the above-mentioned locations is presented in figure 16.3.

The comparison of results obtained using the Boeing grid and grids used by others is presented in figure 16.4 for the *SST* model. As can been seen from figure 16.1, Boeing's grid condenses many points near the stagnation and the shock regions. Thus it results in a better pressure peak near the front of the airfoil and a better shock resolution.

Effects of freestream conditions on the k-ω model are shown in figure 16.5. The freestream turbulent kinetic energy is fixed according to $k/U_\infty^2 = 10^{-6}$ while the value of μ/μ_t varies from 10^{-3} to 1. The results show that the k-ω model does not seem to be affected by the freestream conditions in this particular test case.

Finally, by slightly adjusting the angle of attack by ±10%, it can be seen from figure 16.6 that the change of the solution is smaller than the differences found in the models.

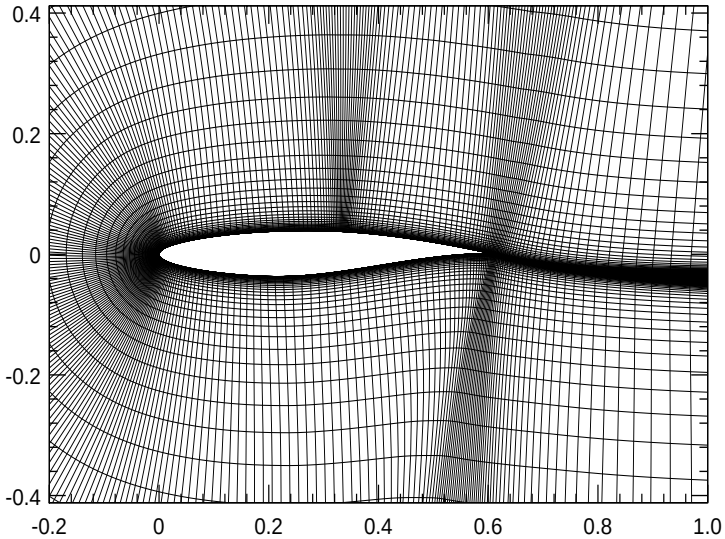

Figure 16.1. Computational grid with 386×82 points.

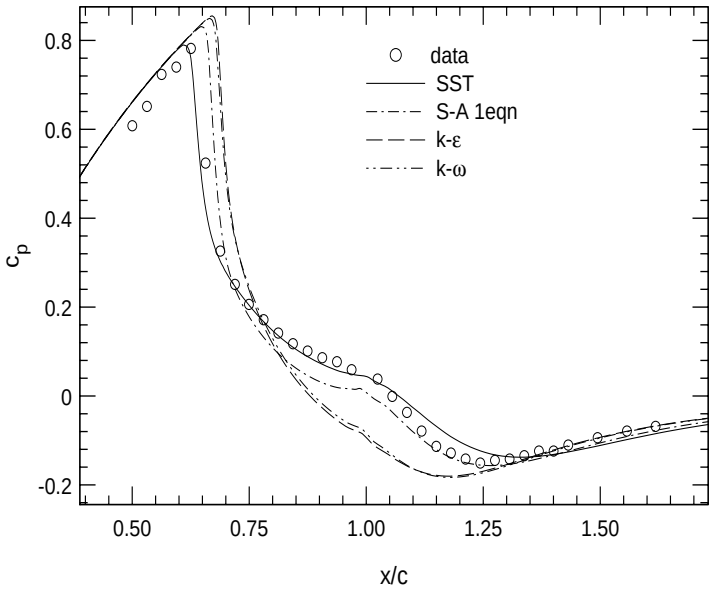

Figure 16.2. Comparison of surface pressure and skin friction coefficients.

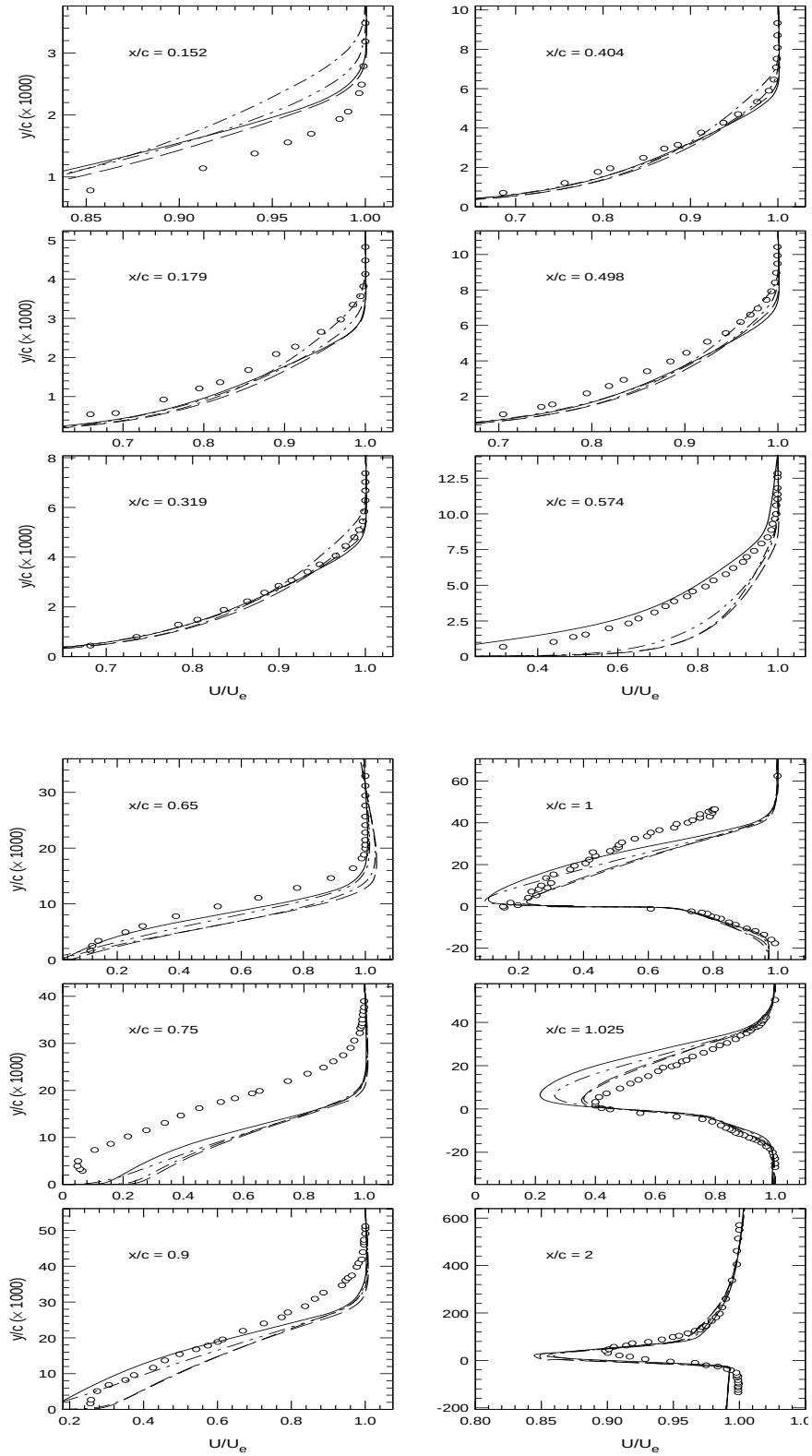

Figure 16.3. Comparison of velocity profiles. See symbol notations in figure 16.2.

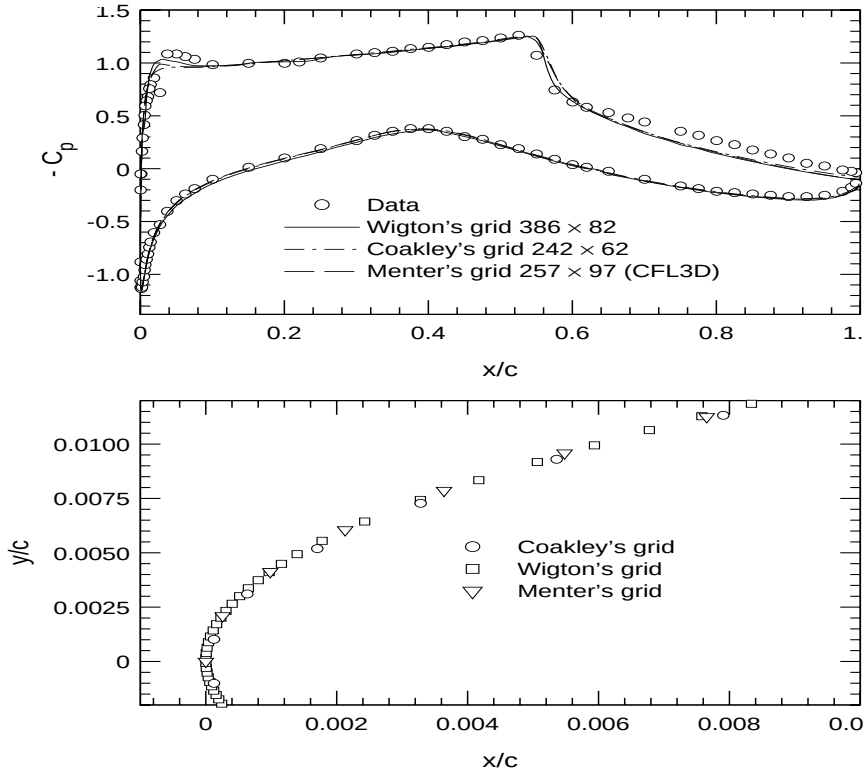

Figure 16.4. Grid sensitivity study.

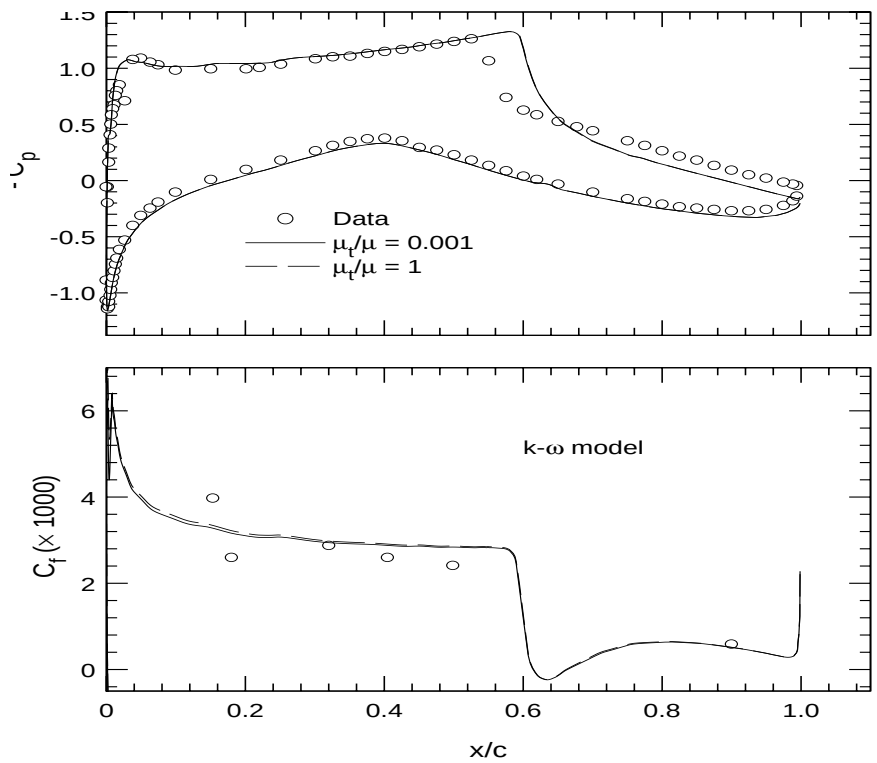

Figure 16.5. Effects of freestream boundary conditions on the *k*-ω model.

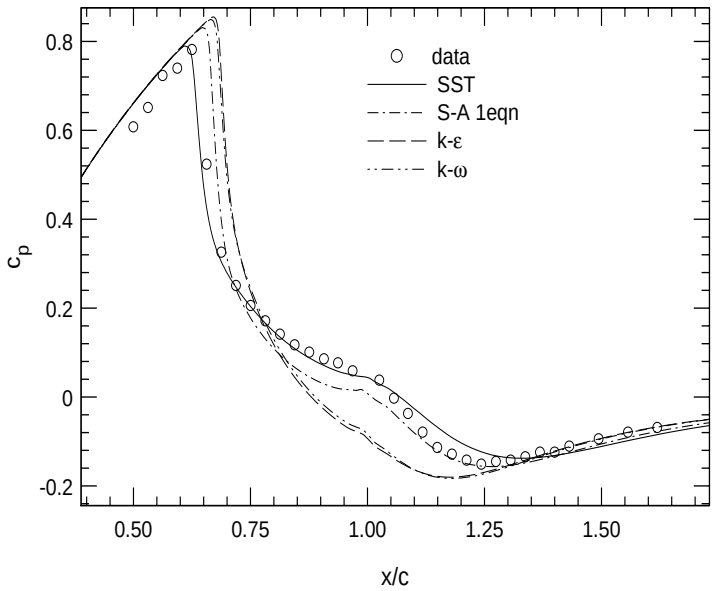

Figure 16.6. Effects of slight variation in the angle of attack of the mean flow.

Part E. General Conclusions

Section 17. Conclusions and Recommendations

In this section, we will give our summary of the work performed and our conclusions regarding the relative performance of the various models tested. Four turbulence models were tested on a series of ten flows. The models included the one-equation model of Spalart and Allmaras and the two-equation models of Wilcox, Launder-Sharma, and Menter. The Wilcox model and the Menter *SST* models are k-ω models while the Launder-Sharma model is a k-ε model. Of the ten flows tested, seven were relatively simple free-shear and zero-pressure-gradient boundary layer flows and three were relatively complex flows involving separation. In addition to testing the relative performance of the models by comparing predictions with experimental data, tests to determine the numerical performance of the models were also conducted. These tests included studies of grid refinement and sensitivity to initial and boundary conditions.

Our conclusions regarding the relative performance of the various models studied is as follows. The best overall model is judged to be the k-ω *SST* model, followed by the Spalart-Allmaras model, then the Launder-Sharma k-ε model, and finally the k-ω model of Wilcox. The *SST* model is considered the best model because it does the best overall job in predicting the complex flows involving separation while giving results comparable with the best of the other models for the simple flows. For the simple free-shear flows, all of the models except the Wilcox model are about equal in their performance, with the Spalart-Allmaras model giving best predictions of the mixing layer and plane wake flows and the Launder-Sharma and *SST* models giving the best predictions of the jet flows. The performance of the Wilcox model is judged to be poor for these flows because of its sensitivity to freestream conditions with the resulting unreliability of solutions. None of the unmodified models do well in predicting the compressible mixing layer, although with compressibility modifications they do give improved predictions.

For the complex flows, as stated above, the best overall model was the *SST* model because of its ability in predicting separation. The worst model in this regard was the Launder-Sharma k-ε model with the Spalart and Wilcox models falling in between. The Wilcox model did not appear to be as sensitive to freestream conditions for the complex flows (where a Navier-Stokes solver was used) as it was for the free-shear flows, although there was sensitivity. While there appear to be several possible explanations for this, we are not prepared to offer a definitive explanation at this time.

With regard to the numerical performance of the models, the Spalart-Allmaras model was found to be the best, followed by the *SST* model, and then the Launder-Sharma and Wilcox models. This evaluation was based on grid spacing required for accurate solutions and the maximum y^+ allowable at the first grid point off the wall.

Although the Menter *SST* and Spalart-Allmaras models are found to give superior performance compared with the other models, there is considerable room for improvement of these models. As stated above, the *SST* model needs improvement on the wake flow, and the S-A model needs improvement on the jet flows. All of the models need better compressibility corrections for free-shear flows. Although not discussed in this report, none of the models appear to do well on recovering flows downstream of reattachment. Corrections for rotation and curvature are still another area requiring attention. Finally, the *SST* and *S-A* models are not coordinate-invariant in that they use functions

dependent on distance from nearest walls, whereas the models of Launder and Sharma and Wilcox are invariant. Coordinate invariance is a desirable feature in models since it removes ambiguities and uncertainties in the definition of a distance function and is more in tune with the original intent of higher order turbulence modeling. It would be desirable if the two newer models could be made coordinate-invariant as well. These topics, as well as additional testing of the currently popular models on a variety of flows, will be the subject of future studies.

Appendix. Self-Similar Equations for Free-Shear Flows

There is a large variety of self-similar flows that are of great importance from an engineering and a turbulence modeling point of view. These flows include a large variety of physical phenomena of practical flows (ref. 3), compressible and incompressible flows, attached boundary layers, and free-shear flows. Mixing layers, jets, and far wakes belong to this class of turbulent flows. The principle of self-similarity of free-shear flows at high Reynolds numbers asserts that far enough downstream the flow is geometrically similar at all sections and the similarity is independent of initial conditions (refs. 3 and 4). These flows can be solved numerically using Navier-Stokes codes in complex engineering applications, and using simpler methods with transformed self-similar equations in turbulence modeling validations.

a. Compressible boundary layer equations

The two-dimensional equations of motion for the self-similar turbulent mixing layer of a compressible perfect gas are given by the conservation of mass, momentum, and energy equations and the equation of state. The static pressure is assumed constant and equal to the freestream pressure. The conservative form of the equations neglecting lower order terms is written as follows:

$$
\begin{aligned}
\frac{\partial}{\partial x}(\rho u) + \frac{\partial}{\partial y}(\rho v) &= 0 \\
\frac{\partial}{\partial x}\left(\rho u^2\right) + \frac{\partial}{\partial y}(\rho u v) &= \frac{\partial}{\partial y}\left(\mu_t \frac{\partial u}{\partial y}\right) \\
\frac{\partial}{\partial x}(\rho u H) + \frac{\partial}{\partial y}(\rho v H) &= \frac{\partial}{\partial y}\left(c_p \frac{\mu_t}{Pr_t}\frac{\partial T}{\partial y} + u\mu_t \frac{\partial u}{\partial y} + \sigma_k \mu_t \frac{\partial k}{\partial y}\right) \\
p &= R\rho T \\
H &= c_p T + \frac{u^2}{2} + k
\end{aligned}
\tag{1}
$$

where x and y are the coordinate directions, u and v are the velocity components, ρ is the density, T is the temperature, p is the static pressure, and H is the total enthalpy of the fluid. The turbulent kinetic energy is k, the absolute eddy viscosity is μ_t, the specific heat of the gas at constant pressure is c_p, the perfect gas constant is R, and the turbulent Prandtl number is Pr_t.

Equations 1 for total enthalpy and energy conservation include the turbulent kinetic energy, k. This quantity is not available and is omitted in zero-equation turbulence models; it can be included or excluded in two-equation turbulence models. The rigorous approach indicates that all quantities should be included, although little difference is found when these terms are included in the present simulations of free-shear flows.

In most computational fluid dynamics (CFD) codes, the equations of motions are written in nondimensional form. Equations 1 may be written in nondimensional form using a reference length scale, pressure, and density leading to a similar set of equations where the factor c_p is replaced by the factor $\gamma/(\gamma - 1)$. The factor γ is the ratio of specific heats, which is equal to $\gamma = 1.4$ for a diatomic perfect gas

according to classical statistical mechanics. The reference values are usually selected to be freestream values in the high-speed side of the mixing layer.

b. Incompressible two-dimensional and axisymmetric equations

The equations of motion for two-dimensional and axisymmetric free-shear flows of an incompressible fluid are given by the conservation of mass and momentum. The static pressure is assumed constant and equal to the freestream pressure. The conservative form of the equations neglecting lower order terms is written as follows:

$$\begin{gathered} \frac{\partial u}{\partial x} + \frac{\partial v}{\partial y} = 0 \\ \frac{\partial}{\partial x}\left(u^2\right) + \frac{\partial}{\partial y}(uv) = \frac{1}{y^j}\frac{\partial}{\partial y}\left(y^j \nu_t \frac{\partial u}{\partial y}\right) \end{gathered} \tag{2}$$

In equations 2, the subscript $j = 0$ stands for two-dimensional flow and $j = 1$ stands for axisymmetric flow. The kinematic eddy viscosity is defined as $\nu_t = \mu_t/\rho$.

c. Separation of variables and coordinate transformation

The self-similar equations can be written in compact form with the following transformations from (x,y) coordinates to (η,x) self-similar coordinates, and separation of variables for the velocity components and turbulence variables, for mixing layer and jet flows (refs. 3 and 4) as

$$\begin{gathered} \eta = \frac{y}{x} \qquad \text{and} \qquad x = x \\ u = aU \qquad v = aV \qquad \rho = r\rho \qquad T = T/u_1^2 \qquad J = 2\pi^j \int U^2 y^j dy \\ k = a^2 K \qquad \varepsilon = \frac{a^3}{x}E \qquad \omega = \frac{a}{x}W \qquad \nu_\tau = axN \end{gathered} \tag{3}$$

and with the following transformation (ref. 2) for far wake flows as

$$\begin{gathered} \eta = yu_\infty/\sqrt{Dx} \qquad \text{and} \qquad x = x \\ u = u_\infty - aU \qquad k = a^2 K \qquad D = 2\int \rho u\,(u_\infty - u)\,dy \\ \omega = \frac{u_\infty}{x}W \qquad \varepsilon = \frac{u_\infty a^2}{x}E \qquad \nu_\tau = \frac{a^2 x}{u_\infty}N \end{gathered} \tag{4}$$

where the self-similar variables U, V, K, W, N, E, T, and ρ are functions only of η (for simplicity the symbols T and ρ are repeated in the definition of the separation of variables); the variables a, u_1, and r are functions only of the transformed coordinate x; and u_∞ is the constant velocity of the freestream wake flow. D is the total drag per unit mass on the body upstream of the wake flow, and J is the momentum flux per unit mass of the jet. The variables k, ε, and ω are the turbulent kinetic energy, dissipation rate, and specific dissipation rate variables defined in the turbulence models.

The transformation coefficient, $a(x)$, is chosen without loss of generality for each one of the turbulent free-shear flows as follows:

Flow	$a(x)$
Mixing layer	u_1
Plane jet	$(J/x)^{1/2}$
Round jet	$J^{1/2}/x^{3/2}$
Far wake	$(D/\rho x)^{1/2}$

d. Self-similar equations

The transformed boundary layer equations of motion for two-dimensional and axisymmetric flows are shown below.

- Mean momentum and mass conservation equations for compressible mixing layer

The self-similar mean momentum, energy, and mass conservation equations for free-shear flows of a compressible fluid are shown below.

$$\rho V^* \frac{dU}{d\eta} - \frac{d}{d\eta}\left(\rho N \frac{dU}{d\eta}\right) = 0$$

$$\rho V^* \frac{dH}{d\eta} - \frac{d}{d\eta}\left(\frac{\gamma}{\gamma - 1}\frac{\rho N}{Pr_t}\frac{dT}{d\eta} + \rho N U \frac{dU}{d\eta} + \sigma_k \rho N \frac{dK}{d\eta}\right) = 0$$

$$\rho V^* \equiv \rho V - \eta \rho U = -\int_0^\eta \rho U d\sigma \tag{5}$$

$$H = \frac{\gamma}{\gamma - 1} T + \frac{U^2}{2} + K$$

where the transformed equations have no source terms, and the transformed transverse velocity component is defined as $V^* = V - \eta U$.

The mean energy equation can be reduced to the following equation for the mean temperature profile:

$$\rho V^* \frac{dT}{d\eta} - \frac{d}{d\eta}\left(\frac{\rho N}{Pr_t}\frac{dT}{d\eta}\right) = (\gamma - 1) M_1^2 \rho E \tag{6}$$

where E is the transformed dissipation rate of turbulent kinetic energy, and M_1 is the Mach number of the high-speed side of the layer. In equation 6, the source term has been transformed in order to set the

range of mean velocity, temperature, and density between 0 and 1. If the turbulent kinetic energy is neglected in the definition of total enthalpy in equations 5, then equation 7 for the mean temperature is obtained.

$$\rho V^* \frac{dT}{d\eta} - \frac{d}{d\eta}\left(\frac{\rho N}{Pr_t}\frac{dT}{d\eta}\right) = (\gamma - 1)\, M_1{}^2 \rho N \left(\frac{dU}{d\eta}\right)^2 \tag{7}$$

where the source term is a direct function of the production of turbulent kinetic energy.

- Mean momentum and mass conservation equations for incompressible flows

For incompressible fluids, the self-similar equations for the mean momentum and continuity are shown below.

$$\begin{gathered} V^* \frac{dU}{d\eta} - \frac{1}{\eta^j}\frac{d}{d\eta}\left(\eta^j N \frac{dU}{d\eta}\right) = S_u U \\ V^* \equiv V - \eta U \end{gathered} \tag{8}$$

The transverse velocity component V^* is defined for each free-shear flow in the table on the following page.

- Two-equation turbulence models (refs. 2–4)

The self-similar equations for the two-equation turbulence models can be written in compact form as

$$\begin{gathered} \rho V^* \frac{dK}{d\eta} - \frac{1}{\eta^j}\frac{d}{d\eta}\left(\eta^j \rho \sigma_k N \frac{dK}{d\eta}\right) = \rho N \left(\frac{dU}{d\eta}\right)^2 - \rho E + S_k \rho K \\ \rho V^* \frac{dF}{d\eta} - \frac{1}{\eta^j}\frac{d}{d\eta}\left(\eta^j \rho \sigma_f N \frac{dF}{d\eta}\right) = c_{f1} \rho \frac{F}{K} N \left(\frac{dU}{d\eta}\right)^2 - c_{f2} \rho \frac{F}{K} E + S_f \rho F + 2\sigma_c \frac{\rho}{W}\frac{dK}{d\eta}\frac{dF}{d\eta} \\ N = \frac{K}{W} = c_\mu \frac{K^2}{E} \qquad E = \beta^* W K \qquad c_\mu = \beta^* = 0.09 \end{gathered} \tag{9}$$

and the model constants for free shear flows are shown below as

Model	K-F	E	c_{f1}	c_{f2}	σ_f	σ_k	σ_c
k-ε (ref. 6)	K-E	E	$c_{\varepsilon 1}$=1.44	$c_{\varepsilon 2}$=1.92	σ_ε=1.3	1.0	0
k-ω (ref. 4)	K-W	$\beta^* WK$	γ=5/9	β/β^*=5/6	σ=0.5	σ^*=0.5	0
SST (ref. 14)	K-W	$\beta^* WK$	γ=0.44	β/β^*=0.92	σ_ω=0.856	1.0	σ_ω

where the generalized nomenclature of model K-F stands for K-E or K-W models.

• One-equation turbulence model

The self-similar equations for the one-equation model of Spalart-Allmaras (ref. 7) can be written in compact form as

$$\rho V^* \frac{dN}{d\eta} - \frac{1}{\eta^j}\frac{1}{\sigma}\frac{d}{d\eta}\left(\eta^j \rho N \frac{dN}{d\eta}\right) = c_{b1}\rho N \frac{dU}{d\eta} + c_{b2}\frac{\rho}{\sigma}\left(\frac{dN}{d\eta}\right)^2 + S_s \rho N$$
$$c_{b1} = 0.1355 \qquad c_{b2} = 0.622 \qquad \sigma = 2/3 \tag{10}$$

• Flow Parameters

For each free-shear flow, the parameters of the model equations are defined as

Flow	j	S_u	S_k	S_ε	S_ω	S_s	V^*
Mixing layer	0	0	0	U	U	$-U$	$-\int_0^\eta U(\sigma)\, d\sigma$
Round jet	1	U	$2U$	$2U$	$4U$	0	$-(1/\eta)\int_0^\eta U(\sigma)\, d\sigma$
Plane jet	0	$0.5U$	U	$2.5U$	$1.5U$	U	$-0.5\int_0^\eta U(\sigma)\, d\sigma$
Far wake	0	0.5	1	2	1	0	-0.5η

e. Boundary conditions

The boundary conditions on the velocity and turbulence variables are Dirichlet conditions (specified function value) in freestream boundaries, and Neumann conditions (specified zero normal gradient) in symmetry boundaries.

The conservation of the total momentum leads to an additional integral constraint in free-shear flows (conservation of total drag D in far wake flows and total momentum J in jet flows as shown in the table on page 83). These necessary conditions must be satisfied by the numerical method in order to achieve convergence from initial profiles to self-similar profiles. There are different numerical methods to impose integral constraints into the numerical method. One successful procedure is obtained by explicitly scaling the mean velocity profile after each numerical iteration of the numerical relaxation until convergence is achieved; the system of ordinary differential equations may be relaxed until the error reaches machine accuracy. However, this method decreases the rate of convergence and increases the total computational time. For plane jet and far wake flows, the “inverse method of relaxation” provides a much faster convergence to the self-similar solution. In this method, instead of specifying a symmetry or Neumann boundary condition at the center of the flow, the velocity magnitude in the symmetry plane is specified after each iteration subject to the conservation of total momentum in the streamwise direction. The use of such an adaptive Dirichlet condition instead of Neumann condition at the center of these flows leads to a very fast relaxation procedure and the same final solution.

References

1. Marvin, J. G.; and Holst, T. L.: CFD Validation for Aerodynamic Flows—Challenge for the 90's. AIAA Paper 90-2995, AIAA 8th Applied Aerodynamics Conference, 1990.
2. Marvin, J. G.: Accuracy Requirements and Benchmark Experiments for CFD Validation. Paper No. 2, AGARD-CP 437, vol. 1, Validation of Computational Fluid Dynamics, May 1988.
3. Schlichting, H.: Boundary Layer Theory. McGraw-Hill Book Company, Inc., New York, Toronto, London, Verlag G. Braun, Karlsruhe, 1960.
4. Wilcox, D. C.: Turbulence Modeling for CFD. DCW Industries, Inc., 5354 Palm Drive, La Cañada, Calif., 1993.
5. Jones, W. P.; and Launder, B. E.: The Prediction of Laminarization with a Two-Equation Model of Turbulence. International Journal of Heat and Mass Transfer, vol. 15, 1972, pp. 301–314.
6. Launder, B. E.; and Sharma, B. I.: Application of the Energy Dissipation Model of Turbulence to the Calculation of Flow Near a Spinning Disc. Letters in Heat and Mass Transfer, vol. 1, no. 2, 1974, pp. 131–138.
7. Menter, F. R.: Two-Equation Eddy Viscosity Turbulence Models for Engineering Applications. AIAA J., vol. 32, Nov. 1994, pp. 1299–1310.
8. Spalart, P. R.; and Allmaras, S. R.: A One-Equation Turbulence Model for Aerodynamic Flows. AIAA Paper 92-0439, 1992.
9. Spalart, P. R.; and Allmaras, S. R.: A One-Equation Turbulence Model for Aerodynamic Flows. La Recherche Aerospatiale, no. 1, 1994, pp. 5–21.
10. Rodi, W.: Experience with Two-Layer Models Combining the k-ε Model with a One-Equation Model Near the Wall. AIAA Paper 91-0216, Jan. 1991.
11. Wilcox, D. C.: Reassessment of the Scale-Determining Equation for Advance Turbulence Models. AIAA J., vol. 26, no. 11, Nov. 1988, pp. 1299–1310.
12. Menter, F. R.: Influence of Freestream Values on k-ω Turbulence Model Predictions. AIAA J., vol. 30, no. 6, June 1992, pp. 1657–1659.
13. Menter, F. R.: Zonal Two Equation k-ω Turbulence Models for Aerodynamic Flows. AIAA Paper 93-2906, Orlando, Fla., 1993.
14. Menter, F. R.; and Rumsey, L. C.: Assessment of Two-Equation Turbulence Models for Transonic Flows. AIAA Paper 94-2343, 25th AIAA Fluid Dynamics Conference, Colorado Springs, Colo., June 20–23, 1994.
15. Johnson, D. A.; and King, L. S.: A Mathematically Simple Turbulence Closure Model for Attached and Separated Turbulent Boundary Layers. AIAA J., vol. 23, Nov. 1985, pp. 1684–1692.
16. Baldwin, B. S.; and Barth, T. J.: A One-Equation Turbulence Transport Model for High Reynolds Number Wall-Bounded Flows. NASA TM-102847, 1990.
17. Kline, S. J.; Cantwell, B. J.; and Lilley, G. M.: 1980-81 AFOSR-HTTM-Stanford Conference on Complex Turbulent Flows. Stanford University, Stanford, Calif., 1981.
18. Birch, S.: Planar Mixing Layer. In 1980-81 AFOSR-HTTM-Stanford Conference on Complex Turbulent Flows, S. J. Kline, B. J. Cantwell, and G. M. Lilley, eds., Stanford University, Stanford, Calif., vol. 1, 1981, pp. 170–177.

19. Liepmann, H. W.; and Laufer, J.: Investigations of Free Turbulent Mixing. NACA TN-1257, 1947.

20. Roger, S. E.; and Kwak, D.: An Upwind Differencing Scheme for the Steady-State Incompressible Navier-Stokes Equation. NASA TM-103911, Mar. 1992.

21. Rumsey, C. L.; and Vatsa, V. N.: A Comparison of the Predictive Capabilities of Several Turbulence Models using Upwind and Central-Difference Computer Code. AIAA Paper 93-0192, 1993.

22. Foss, J. F.: The Effect of the Laminar/Turbulent Boundary Layer States on the Development of a Plane Mixing Layer. Proc. Symposium on Turbulent Shear Flows, April 18–20, 1977, pp. 11.33–11.42.

23. Bradbury, L. J. S.: The Structure of a Self-Preserving Turbulent Plane Jet. J. Fluid Mech., vol. 23, pt. 1, Sept. 1965, pp. 31–64.

24. Wygnanski, I.; and Fiedler, H. E.: Some Measurements in the Self-Preserving Jet. J. Fluid Mech., vol. 38, pt. 3, Sept. 18, 1969, pp. 577–612. (Also in Boeing Scientific Research Labs, Flight Science Laboratory, Document D1-82-0712.)

25. Fage, A.; and Falkner, V. M.: Note on Experiments on the Temperature and Velocity in the Wake of a Heated Cylindrical Obstacle. Proc. Roy. Soc., London, vol. A135, 1932, pp. 702–705.

26. Chevray, R.; and Kovasznay, L. S. G.: Turbulence Measurements in the Wake of a Thin Flat Plate. AIAA J, vol. 7, no. 8, Aug. 1969.

27. Bradshaw, P.: Compressibility Effects on Free-Shear Layers. In 1980-81 AFOSR-HTTM-Stanford Conference on Complex Turbulent Flows, S. J. Kline, B. J. Cantwell, and G. M. Lilley, eds., Stanford University, Stanford, Calif., vol. 1, 1981, pp. 364–368.

28. Birch, S. F.; and Eggers, J. M.: A Critical Review of the Experimental Data for Developed Free Turbulent Shear Layers. Free Turbulent Shear Flows, Volume I—Conference Proceedings, Langley Research Center, NASA, Hampton, Va., July 20–21, 1972, pp. 11–40.

29. Settles, G. S.; and Dodson, L. J.: Hypersonic Turbulent Boundary-Layer and Free Shear Database. NASA CR-177610, Ames Research Center, Apr. 1993.

30. Viegas, J. R.; and Rubesin, M. W.: Assessment of Compressibility Corrections to the k-ε Model in High-Speed Shear Layers. AIAA J., vol. 30, no. 10, Oct. 1992, pp. 2369–2370.

31. Samimy, M.; and Elliot, G. S.: Effects of Compressibility on the Characteristics of Free Shear Layers. AIAA J., vol. 28, no. 3, Mar. 1990, pp. 439–445.

32. Huang, P. G.; and Coakley, T. J.: An Implicit Navier-Stokes Code for Turbulence Flow Modeling. AIAA Paper 92-0547, 30th Annual Meeting, Reno, Nev., Jan. 6–9, 1992.

33. Coles, D.: The Law of the Wakes in the Turbulent Boundary Layer. J. Fluid Mech., vol. 1, 1956, pp. 191–226.

34. Coles, D.: The Turbulent Boundary Layer in a Compressible Fluid. RAND Corp Rept. R-403-PR, 1962.

35. Huang, P. G.; Schwarz, W. R.; and Bradshaw, P.: L-BL-SW— A General Reynolds-Stress Boundary Layer Code. Internal Report, Dept. of Mech. Engrg., Stanford University, Stanford, Calif., June 1990.

36. Van Driest, E. R.: Turbulent Boundary Layer in Compressible Fluids. J. Aeronaut. Sci., vol. 18, no. 3, 1951, pp. 145–160.

37. Hopkins, E. J.; and Inouye, M.: An Evaluation of Theories for Predicting Turbulent Skin Friction and Heat Transfer on Flat Plates at Supersonic and Hypersonic Mach Number. AIAA J., vol. 9, no. 6, 1971, pp. 993–1003.

38. Huang, P. G.; Bradshaw, P.; and Coakley, T. J.: Skin Friction and Velocity Profile Family for Compressible Turbulent Boundary Layers. AIAA J., vol. 31, no. 9, 1993, pp. 1600–1604.

39. Driver, D. M.: Reynolds Shear Stress Measurements in a Separated Boundary Layer Flow. AIAA Paper 91-1787, 1991.

40. Bachalo, W. D.; and Johnson, D. A.: Transonic Turbulent Boundary-Layer Separation Generated on an Axisymmetric Flow Model. AIAA J., vol. 24, 1986, pp. 437–443.

41. Cooke, P.; McDonald, M.; and Firmin, M.: Airfoil RAE2822—Pressure Distributions and Boundary Layer Wake Measurements. AGARD AR-138, 1979.

REPORT DOCUMENTATION PAGE

Form Approved
OMB No. 0704-0188

Public reporting burden for this collection of information is estimated to average 1 hour per response, including the time for reviewing instructions, searching existing data sources, gathering and maintaining the data needed, and completing and reviewing the collection of information. Send comments regarding this burden estimate or any other aspect of this collection of information, including suggestions for reducing this burden, to Washington Headquarters Services, Directorate for information Operations and Reports, 1215 Jefferson Davis Highway, Suite 1204, Arlington, VA 22202-4302, and to the Office of Management and Budget, Paperwork Reduction Project (0704-0188), Washington, DC 20503.

1. AGENCY USE ONLY *(Leave blank)*

2. REPORT DATE
April 1997

3. REPORT TYPE AND DATES COVERED
Technical Memorandum

4. TITLE AND SUBTITLE
Turbulence Modeling Validation, Testing, and Development

5. FUNDING NUMBERS
505-59-50
505-59-53

6. AUTHOR(S)
J. E. Bardina,* P. G. Huang,† and T. J. Coakley

7. PERFORMING ORGANIZATION NAME(S) AND ADDRESS(ES)
Ames Research Center
Moffett Field, CA 94035-1000

8. PERFORMING ORGANIZATION REPORT NUMBER
A-976276

9. SPONSORING/MONITORING AGENCY NAME(S) AND ADDRESS(ES)
National Aeronautics and Space Administration
Washington, DC 20546-0001

10. SPONSORING/MONITORING AGENCY REPORT NUMBER
NASA TM-110446

11. SUPPLEMENTARY NOTES
Point of Contact: T. J. Coakley, Ames Research Center, MS 229-1, Moffett Field, CA 94035-1000
(415) 604-6451
*Caelum Research Corp., Moffett Field, California †University of Kentucky, Lexington, Kentucky

12a. DISTRIBUTION/AVAILABILITY STATEMENT
Unclassified — Unlimited
Subject Category 34

12b. DISTRIBUTION CODE

13. ABSTRACT *(Maximum 200 words)*

The primary objective of this work is to provide accurate numerical solutions for selected flow fields and to compare and evaluate the performance of selected turbulence models with experimental results. Four popular turbulence models have been tested and validated against experimental data of ten turbulent flows. The models are: 1) the two-equation k-ω model of Wilcox, 2) the two-equation k-ε model of Launder and Sharma, 3) the two-equation k-ω/k-ε SST model of Menter, and 4) the one-equation model of Spalart and Allmaras. The flows investigated are five free shear flows consisting of a mixing layer, a round jet, a plane jet, a plane wake, and a compressible mixing layer; and five boundary layer flows consisting of an incompressible flat plate, a Mach 5 adiabatic flat plate, a separated boundary layer, an axisymmetric shock-wave/boundary layer interaction, and an RAE 2822 transonic airfoil. The experimental data for these flows are well established and have been extensively used in model developments. The results are shown in the following four sections: Part A describes the equations of motion and boundary conditions; Part B describes the model equations, constants, parameters, boundary conditions, and numerical implementation; and Parts C and D describe the experimental data and the performance of the models in the free-shear flows and the boundary layer flows, respectively.

14. SUBJECT TERMS
Turbulence modeling, Computational fluid dynamics, CFD, Code validation

15. NUMBER OF PAGES
98

16. PRICE CODE
A05

17. SECURITY CLASSIFICATION OF REPORT
Unclassified

18. SECURITY CLASSIFICATION OF THIS PAGE
Unclassified

19. SECURITY CLASSIFICATION OF ABSTRACT

20. LIMITATION OF ABSTRACT